TABLE OF CONTENTS

XIV

LIST OF TABLES

Page

LIST OF FIGURES

Page

XX

LIST OF ABBREVIATIONS

UAV   Unmanned Aerial Vehicle

LARCASE   Laboratoire de Recherche en Commande Active, Avionique et Aéroservoélasticité/ Research Laboratory in Active Controls, Avionics and AeroServoElasticity

ÉTS   École de Technologie Superieure

MFC   MicroFiber Composite

PBP   Post-Buckled Pre-compressed

ESAC   Elastically Shaped Aircraft Concept

SMA   Shape Memory Alloy

IAR-NRC   Institute of Aerospace Research-National Research Council Canada

LVDT   Linear Variable Differential Transformer

ANFIS   Adaptive Neuro-Fuzzy Inference System

BLDC   Brushless Direct Current

DC   Direct Current

AC   Alternating Current

PMSM   Permanent Magnet Synchronous Motor

NI   National Instruments

PID   Proportional-Integral-Derivative

PC   Personal Computer

GUI   Graphical User Interface

STD   Standard Deviation

FFT   Fast Fourier Transform

EPOS	Easy to use Positioning System
CAN	Controller Area Network
TCP/IP	Transmission Control Protocol/Internet Protocol
DAQ	Data Acquisition
FPGA	Field-Programmable Gate Array
FIFO	First In-First Out
I/O	In/Out
DSP	Digital Signal Processing
MF/mf	Membership Function
LSE	Least Squares Estimation
GD	Gradient Descent
DI/DIs	Digital Indicator/ Digital Indicators
CFD	Computational Fluid Dynamics
BEMF	Back ElectroMotive Force
RPM	Revolutions Per Minute

LIST OF SYMBOLS

V_{XN}	Voltage of the phase X to Neutral	Volt
V_{YN}	Voltage of the phase Y to Neutral	Volt
V_{ZN}	Voltage of the phase Z to Neutral	Volt
V_{dc}	Voltage of the phase Z to Neutral	Volt
A_j	j^{th} linguistic variable	Nondimensional
x	Crisp input variable	Nondimensional
p	Number of the linguistic variables/number of the rules	Nondimensional
A	Fuzzy membership set of the input variable x	Nondimensional
y_j	Consequent linear polynomial function associated with the crisp input x and the jth linguistic variable A_j, or Output membership function associated with the jth linguistic variable	Nondimensional
$L_{i,k}$	The output of the ith fuzzy input node of the layer k	Nondimensional
$\alpha_{A_j}(x)$	Input membership function with input x	Nondimensional
W_j	Weights of the associated rule j^{th} *Note* : number of rules = number of linguistic variables	Nondimensional
$\overline{W_j}$	Ratio of the jth rule's weight W_j to the sum of all the rules' weight $\sum_j^p W_j$	Nondimensional
a_j	Consequent parameter associated with j^{th} linguistic variable	Nondimensional
b_j	Consequent parameter associated with j^{th} linguistic variable	Nondimensional
y	Crisp output variable	Nondimensional

T_{AB}	Triangular norm of two variables A and B	Nondimensional
NBB	Linguistic variable - Negative Extra Big	Nondimensional
NB	Linguistic variable - Negative Big	Nondimensional
NLL	Linguistic variable - Negative Extra Large	Nondimensional
NL	Linguistic variable - Negative Large	Nondimensional
NM	Linguistic variable - Negative Medium	Nondimensional
NS	Linguistic variable - Negative Small	Nondimensional
ZZ	Linguistic variable - Zero	Nondimensional
PS	Linguistic variable - Positve Small	Nondimensional
PM	Linguistic variable - Positive Medium	Nondimensional
PL	Linguistic variable - Positive Large	Nondimensional
PLL	Linguistic variable - Positive Extra Large	Nondimensional
PB	Linguistic variable - Positive Big	Nondimensional
PBB	Linguistic variable - Positive Extra Big	Nondimensional
l_j	Premise parameter associated with j^{th} linguistic variable	Nondimensional
m_j	Premise parameter associated with j^{th} linguistic variable	Nondimensional
n_j	Premise parameter associated with j^{th} linguistic variable	Nondimensional
o_j	Premise parameter associated with j^{th} linguistic variable	Nondimensional
t_j	Premise parameter associated with j^{th} linguistic variable	Nondimensional

t_j	Premise parameter associated with j^{th} linguistic variable	Nondimensional
u_j	Premise parameter associated with j^{th} linguistic variable	Nondimensional
v_j	Premise parameter associated with j^{th} linguistic variable	Nondimensional
ΔP	The mean value of the pressures of all the recorded data points of a Kulite sensor	psi
ΔP_{std}	The standard deviation of the pressure on a Kulite sensor	psi
ΔP_i	The pressure of the ith data point	psi
M	Mach number	Nondimensional
α	Angle of attack	degree
δ_{ail}	Aileron deflection angle	degree
c	Chord of the wing	meter
x/c	Ratio of a point on the horizontal axis x to the chord of the wing	Nondimensional
y/c	Ratio of a point on the vertical axis y to the chord of the wing	Nondimensional

INTRODUCTION

The perspectives of energy shortages have made it imperative to find ways to produce and use renewable energy sources such as solar, wind, bio-fuel and hydropower and others. Worldwide concerns about the climate have also stimulated the development of green technologies, and have supported efforts to decrease fuel consumption. Reducing fuel consumption also serves to decrease (or slow down the increase of) the amount of greenhouse gas emissions. Along these lines, aerospace companies are trying to incorporate morphing wings on aircrafts manufactured from light modern materials. These new technologies would allow airlines to reduce fuel costs and the air pollution caused by aircraft. According to (Barbarino, Bilgen, Ajaj, Friswell, & Inman, 2011), a morphing wing can change its shape (thus, its geometry) according to aerodynamical structures and control interactions,. The morphing concept arose from mimicking the movement of birds in flight. The "morphing wing" concept was already applied by Wright brothers in the "Wright Flyer" (Anderson, 1987). In their design, the twist of the wings with cables was monitored directly by the pilot and further adjusted for roll control.

The morphing technologies depend on the design of suitable flexible skins. Meanwhile, the skin should be tender and elastic so that the shape of the airfoil can change easily. It should also be able to maintain the wing's ability to sustain the aerodynamic loads, and its structural shape requirements. In general, a morphing system design needs to be simple, easy to implement, and able to overcome the weight penalty caused by its actuation system. The airfoil design must also take into account the expected loading settings and the desired changes of shapes. These changes are different for each specific flight case for which the aerodynamic performances are improved. There are three phases of the airflow along an airfoil, which are: the "laminar flow zone", where the flow is stable; the "turbulence zone", where the flow is turbulent; and the "transition zone" which defines the laminar to turbulent flow conversion (see APPENDIX I, Figure-A I-1).

In this research, the wing upper surface is manufactured using composite materials, and changes its shape using electrical actuators, while Kulite sensors measure the pressures on the wing. The "transition" zone is then determined by using the Root Mean Square (RMS) pressure values. Subsequently, a controller relates the actuator displacements to the Kulite sensor's pressure measurement. The simulation results obtained with the controller are experimentally validated in the Wind Tunnel at the Institute of Aerospace Research-National Research Council of Canada (IAR-NRC).

The remainder of the thesis is organized as follows. A bibliographical review of morphing wings, as well as actuators' controlling methods, is provided in Chapter 1. Chapter 2 discusses the outlines and objectives of the research project. The originality, contributions and methodologies of the work are presented in Chapter 3. Chapter 4 describes the wind tunnel laboratories and the wind tunnel tests. The thesis ends with some conclusions and recommendations for future work presented in the Conclusion section.

CHAPTER 1

LITERATURE REVIEW

1.1   Morphing Skins

Among the many applications of smart and adaptive materials on morphing technologies, the flexible skin's design is complicated and challenging, yet inspirational. A number of researchers carried out studies on different skin designs. Generally speaking, morphing wings can be classified into three categories, depending on their characteristics and purposes as shown in (2011) by Barbarino et al. These categories are the following: planform, out-of-plane and airfoil. These categories then can be divided into several divisions (Barbarino et al., 2011):

- Planform : Chord, Sweep, Span;
- Out-of-plane : Spanwise Bending, Twist, Diherall/Gull;
- Airfoil : Thickness, Camber.

In (Thill, Etches, Bond, Potter, & Weaver, 2008), an overview of morphing skins was given, while in another research work (Thill, Etches, Bond, Potter, & Weaver, 2010), the authors gave a summary of corrugated structures used for morphing skins. By using a composite corrugated structure, morphing skin panels were designed in its trailing edge section. On the second part of the publication, they introduced the corrugated sandwich structures and its application on the morphing wing technology. The wind tunnel tests showed that the chord length could be changed up to 4% chord, control surface deflections was able to reach up to 12 degrees while keeping the aerodynamic surface continuous.

Meanwhile, in (Olympio & Gandhi, 2010), the authors have used cellular honeycombs for the adaptation of skins for morphing aircraft applications. These researchers pointed out that due to its higher stiffness, the cellular cores can bear the global strains 10 times greater than the normal material, which they used to build these cores.

In two research publications (Joo, Reich, & Westfall, 2009) and (Reich, Sanders, & Joo, 2007), these researchers developed flexible skin concepts via topology optimization, while in (2010) Murray, Gandhi, & Bakis developed flexible matrix composite skins. These three research works all focused on increasing the stiffness of the out-of-plane skin part, while maintaining the low stiffness of the in-plane part.

The application of adaptive materials, such as composite, was also presented in (Heryawan, Park, Goo, Yoon, & Byun, 2005). In the research work, a small size morphing wing was designed and manufactured. The design was a combination of composite carbon strips, as well as of balsa and carbon fiber composite. The Wind Tunnel test was carried out with Raynolds numbers of 30,000. The test results indicated that the design helped to increase the total lift force 3 times greater and the drag force was reduced 10% lower through the wing expansion.

Besides the adaptive materials, optimization tools was also used to cope with challenges in the morphing wing technology. Prock, Weisshaar, & Crossley introduced in (2002) a procedure connecting optimization tools and analytical models in order to create various lightweight wing/actuator/structure combinations, which need a minimum amount of energy for the design and manufacture of a morphing wing. In this research, the authors used the energy that the actuator consumes as the functional objective; the internal structure of the wing was featured as variable; via the computation, the most effective actuators and their locations to minimize energy were identified for the morphing wing system.

In (Raither, Heymanns, Bergamini, & Ermanni, 2012), a semi-passive airfoil concept by means of smart materials was proposed. The experimental and simulation results showed that this new conception allowed the morphing airfoil to obtain effectively twist control and offered high lightweight and energy efficiency.

The use of different adaptive structure also give us interesting results. In (2009), Kota et al. described the steps involved in the design, manufacturing and testing of a variable camber

trailing edge in high altitude aircrafts. The elasticity of the structure was the key to the design of a lightweight and low-power adaptive trailing edge. In-flight tests at full-scale Mach number and full-scale dynamic pressure proved the effectiveness of the designed wing. The laminar flow region was retained at over 60% of the airfoil chord.

In (Hetrick, Osborn, Kota, Flick, & Paul, 2007), the researchers at U.S. Air Force Research Laboratory considered a system equipped with an adaptive structure trailing edge flap, which was a section of a laminar airfoil. Wind tunnel tests showed that this technology offered a drag reduction of 25% and the lift/drag ratio was increased by 75%.

Along with the flaps, the elasticity technology in morphing wing design was applied in (N. T. Nguyen, Ting, Nguyen, Dao, & Trinh, 2013) and (N. Nguyen & Urnes, 2012), where the drag reduction goal was achieved through an elastic wing shaping control methodology. The wing structures with high flexibility were realised by utilising the Elastically Shaped Aircraft Concept (ESAC). With the reduction of drag force of 50% using a new flap, "Variable Camber Continuous Trailing Edge" flap (N. Nguyen & Urnes, 2012), the design and ESAC was proved to be a potential approach in reducing the drag force using flaps.

In (2009), Gamboa , Vale, P. Lau, & Suleman presented a new morphing wing design to enhance the performance of an UAV. They optimized its aerodynamic shape, using a structural morphing template to build a series of optimal wing shapes that gave a lowest drag force in various flight scenarios. Generally speaking, these researchers tried to use telescopic ribs and spar in order to bring changes in the wing shape ("morphing concept").

Another method to alter or change the shape of the wing was developed by researchers at Embraer Aerospace S.A. and University of São Paulo-Brazil (Catalano, Greco Jr, & Martins, 2002). In this approach, the camber line was bended with the aim to make the desired changes in the trailing edges and in the leading edges of the wing. The experimental results showed that the Embraer team was able to reduce the drag force by up to around 24%.

1.2   Actuators and theirs Controllers

Actuators attached to the inside of morphing wings have been used to control the motions of the upper parts of morphing wings. These actuators can be operated by different energy sources such as electrical currents, hydraulic fluid pressures, or pneumatic pressures. Actuator systems have been incorporated on the aircraft, and were used to control the rudder, slats, flaps, brakes and landing gears for a long time. Table 1.1 presents a list of actuators types along with some typical examples (Zupan, Ashby, & Fleck, 2002).

Table 1.1 Classification of actuator types
Taken from Zupan et al. (2002)

Actuator Type	Example
Electromagnetic	Solenoid, Magnetostriction
Electromechanical	Linear Drive, MEMS Comb Drives
Fluidic	Hydraulic, Pneumatic
Piezoelectric	Ceramic, Polymer
Smart Materials	Shape Memory Alloy, Bimetallic
Hybrid	Piezoelectric and Electromechanical

Besides the list, two basic types of actuators can also be distinguished by their motions with respect to the controller command: "linear" and "nonlinear". "Linear actuators" are the actuators whose motions are directly proportional to the controller's command, while for the "nonlinear actuators", this motion relationship is indirect to the controller's command.

The linear actuators are further divided into two groups: "directly linear" and "indirectly linear" actuators.

"Directly linear" actuators can use the power from an engine without the need for any power reductions generated by a gearbox, pinion, belts or wheels. In this case, the electrical energy is used directly to achieve "linear motion".

"Indirectly linear" actuators convert electrical energy into mechanical energy with the aim to generate torque or the required moving force. These are mostly "rotary actuators".

To use indirectly linear actuators for a morphing wing, an adaptive system is required, which translates the rotary motion of the output shaft of a motor into a translational motion capable of ensuring the deformation (shape change) of the wing.

The applications of actuators in morphing wing technologies are indeed various. A Macro-Fiber Composite (MFC) actuator system was used to generate surface induced deformation in (Bilgen, Friswell, Kochersberger, & Inman, 2011). Two cascading active surfaces (upper and lower) were used to compose an airfoil. The authors aimed to obtain the highest possible lift coefficient, as well as the highest lift-to-drag ratio. Under the following wind tunnel conditions: Reynolds number of 127,000, a turbulence rate of 0.85% and air velocity of 15 m/s, the research showed that the lift-to-drag ratio was increased by using these composite actuators.

In (2011), Ohanian et al. used piezoelectric MFC actuators for a bimorphed configuration. This configuration was designed to change the aft part of a control surface cross section.

From its aerodynamic performance point of view, the approach achieved a larger change in the lift coefficient than the one using a hinged servo-drive flapped airfoil.

In (Usher, Ulibarri, & Camargo, 2013), Usher et al. introduced two approaches for designing and manufacturing the control surfaces. One approach involved the formation of flap-like structures by affixing the MFC actuators to the sides of a metal substrate, then attached it to the trailing edge. Another approach showed that MFC actuators were bonded to the wing in a direct way. The direct approach gave a better flexibility than the first approach. However, when they increased wing pressure, there are problems with tension loading, which still has to be solved.

In (1999), Pern & Jacob used the piezoelectric effect to control the airflow on the upper surface of an airfoil. THUNDER actuator, a kind of actuator that is built by binding a skinny sheet of piezoelectric ceramic under hydrostatic pressure between an aluminum electrode and a metal substrate, was created for the adaptive airfoil. The experiments showed that a maximum change of 1 cm of the wing's leading edge was achieved when voltage was put on the actuators; and the amplitude of flutter vibration was also lower.

The piezoelectric effect was also used in (Munday & Jacob, 2002) and (Munday, Jacob, Hauser, & Huang, 2002). In both studies, piezoelectric actuators were used for a NACA 4415 wing. In the research works, the flow separation over the wing's upper surface was investigated. The experimental results obtained in their laboratory revealed that with the help of the actuators, a reduction of 30-60% was found in the separated flow size with respect to the flow size on a shaped static wing. The researchers have also developed an approach using a wing airfoil that adapted to flow conditions, and its aerodynamic performance was improved over its upper surface for low Reynolds numbers with low speeds. Experimental tests with the wing was also carried out at different angles of attack, speeds and Reynolds numbers. Pressure signals were used to provide feedback signals to a real-time controller to extend the laminar flow over the upper surface of the wing, thereby delaying the transition zone.

In (LeBeau, Karam, Pern, & Jacob, 2010), the researchers investigated the low speed flow influence on an adaptive airfoil. In their research, the shape of the upper wing surface was changed by using piezoelectric actuators. At the Reynolds number of 25.000, the experimental results on this morphing airfoil revealed significant changes in its aerodynamic performance.

Other results obtained by Debiasi, Bouremel, Lu, & Ravichandran (2013) indicated that the changing of the shape of the airfoil's upper surface was not the only way to enhance wing or aircraft's aerodynamic performance. They have proposed in their research an airfoil whose upper and lower surfaces were adaptive. In their approach, piezoelectric actuators were built as integral parts of the skin. Wind tunnel tests showed that the hysteresis characteristics of the MFC actuators prevented the desired airfoil shape from being obtained. The researchers proposed using a closed loop control instead of open loop control to avoid and thus to cancel out the hysteresis motions of the actuators. Debiase and his co-workers also observed that the changes on the upper and lower surfaces of the wings equipped with the MFC actuators contributed in achieving better aerodynamic performance.

In (Vos, Barrett, de Breuker, & Tiso, 2007), the actuator's performance was enhanced by using "compressed elements". Post-Buckled Pre-compressed (PBP) piezoelectric bender actuators were used to replace conventional piezoelectric actuators on a reduced scale Unmanned Aerial Vehicle (UAV). These new PBP actuators aimed to control the UAV camber distribution, and therefore induced roll control. In comparison to conventional piezoelectric actuators, the new approach using PBP actuators gave around a factor of 2 to 15.25 degree peak-to-peak higher deflection, an increase of 38% of the roll control authority. The energy consumption was decreased from 24 W to 100mW, and the actuator weight was reduced from 59g to 3g.

Adaptive wing technologies for low-speed UAVs were summarized by Santhanakrishnan and his colleagues (2005). In these UAVs, actuators were integral parts of the wings. Their

summary presented the experimental results obtained from wind tunnel and flight testing for each method.

In (2010), Cosin, Angelo, Catalano, & Bonemer De Salvi have designed and manufactured a novel adaptive wing with enhancement of its aerodynamics properties. Span-wise and chord-wise wing deformations of the wing were allowed and their values were validated with wind tunnel hardware. An optimization algorithm was conceived to link the acquisition hardware to the desired positions given by the actuators.

In (Mashud, Rahman, Kaiser Ahmed, & Mujahidul Islam, 2010), an osccillating camber to control the flow separation was used. Piezoelectric actuators were attached on the upper surface of the wing to carry out the camber's changes. Their tests indicated that the flow separation has occured at an angle of attack of 10 degrees when the actuators were located at 65%-75% of the chord length, and that this separation appeared at 15 degrees from the leading edge for an actuator placed at 55% to 75% of the chord length.

Shape Memory Alloy (SMA) is a kind of smart material and adaptive structures used as actuation systems in morphing wing systems. A flap morphing structure was investigated in (Kang, Kim, Jeong, Lee, & Ahn, 2012). These researchers used an SMA wire actuator to minimize the energy losses due to the geometrical discontinuities.

To further reduce aircraft fuel consumption, Brailovski, Terriault, Georges, & Coutu (2010) created an experimental laminar morphing wing that enhances the laminar flow region on the wing upper surface. The morphing mechanism of the wing moved its upper surface using an SMA actuator system.

Galantai(2012) investigated a scheme to improve an innovative wing equipped with SMAs for UAVs. They designed a lightweight wing that has a high degree of flight adaptability and thus an enhanced performance.

Two Neuro-Fuzzy control methods for open-loop morphing wing systems were studied as part of the CRIAQ 7.1 project (T. L. Grigorie & Botez, 2009; T. L. Grigorie, Botez, & Popov, 2009). These methods considered the pressure differences in relation to airfoil displacements. The two controllers were validated for 33 different flight cases. Another Neuro-Fuzzy controller method was proposed in (T. L. Grigorie & Botez, 2010). Using SMA hysteresis modeling of a morphing wing, these researchers created a new controller by taking advantage of different Neuro-Fuzzy controllers to correlate the sets of forces and electrical current values.

The wind tunnel results in real time of a morphing wing in (Andrei V Popov, Grigorie, Botez, Mamou, & Mébarki, 2010) showed the delay of the transition toward the trailing edge. The transition zone was already detected by means of an algorithm, explained and discussed in their previous work (Andrei Vladimir Popov, Botez, & Labib, 2008). Tests were performed for different angles of attack, Mach and Reynolds numbers, and showed that their method changed the shape of the morphing wing to an optimal formation under various wind tunnel airflow circumstances.

In (T. Grigorie, Botez, & Popov, 2013; T. Grigorie, Popov, & Botez, 2012), these researchers proposed another method for controlling the morphing wing's shape in an open-loop design. In this method, the actuation mechanism consisted of two parallel actuation lines. A Fuzzy logic Proportional Derivative approach was used for the controller. The simulation and the experimental results showed that the controlled system worked well, with a position control error of less than 0.05 mm.

Another way to model and test the morphing wing system in its open-loop architecture was given in (Andrei Vladimir Popov, Grigorie, Botez, Mébarki, & Mamou, 2010). The researchers showed how this architecture could be used, and controlled in order to measure the pressure data on the upper surface of a flexible wing skin using Kulite pressure sensors, and to validate it through wind tunnel tests. They described the controller design and the actuation mechanism that they used to control the laminar flow region on the wing (T.

Grigorie, Popov, Botez, Mamou, & Mébarki, 2012a; Andrei Vladimir Popov, Labib, Fays, & Botez, 2008). Figure 1.1 shows this mechanism, that had two actuations lines, each line had three lines of SMA wires, along with a cam that was sliding span wise on a supporting plate. The rollers were used to translate the span-wise motion. A gas spring was used to restore the SMA after contraction. When the SMA was heated, the cam moved to the right and the actuator contracted. The reverse behavior of the SMA was observed by cooling the SMA. An On-Off Proportional Integral Controller was used to manipulate the vertical displacements of the actuators.

In order to validate the numerical controllers, two programmable power supplies were used to regulate actuation lines, as well as for a Quanser data acquisition card. To obtain the position feedback from the actuator, they implemented Linear Variable Differential Transformer potentiometers (LVDT) coupled to the inputs of a Quanser acquisition card. This system with the integrated controller was first tested on a bench test at their laboratory and then in a wind tunnel. The experiments were carried out under the conditions of a 2 degree angle of attack and a Mach number of 0.25. The results indicated that the transition point was moved successfully towards the trailing edge. However, the nonlinearity behaviour of the SMA actuators used for the morphing wing system in (T. Grigorie, Popov, Botez, Mamou, & Mébarki, 2012b) leads to the design of a new nonlinear controller.
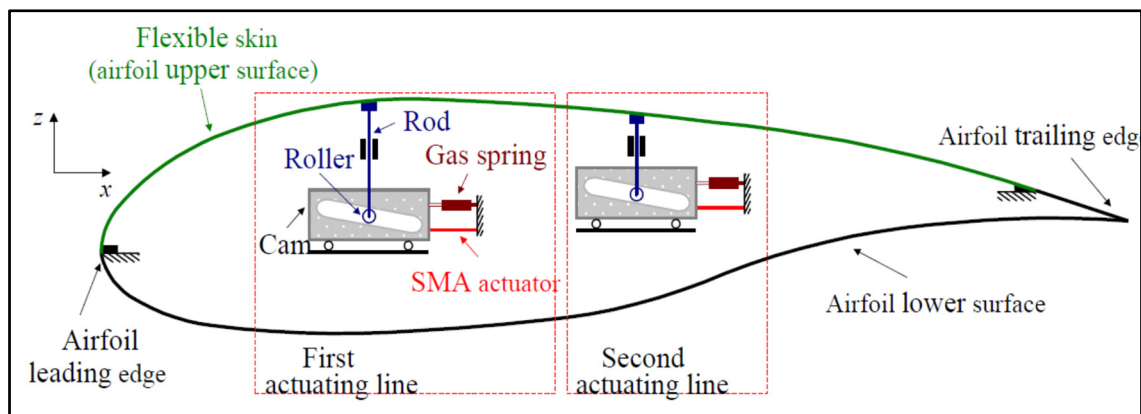
Figure 1.1 Mechanical schematics of a morphing wing model using a SMA actuator
Taken from T. Grigorie et al. (2012a)

Thus, a nonlinear Fuzzy logic-Proportional-Integral-Derivative controller that is also a typical on-off controller (a hybrid controller) was subsequently designed and evaluated (T. L. Grigorie, Botez, Popov, Mamou, & Mébarki, 2012a). This hybrid controller technique was used to control the SMA actuators by regulating the electric current supplied; the aim of this technique is to cancel the deviation ε between the desired values of the vertical displacement that match up with the optimized airfoil displacements and the actual values thatachieved from the LVDT position transducers; in addition, this technique was used to solve the nonlinearities of the SMA actuators' characteristics. Figure 1.2 shows the block diagram of the control system using the hybrid controller (T. L. Grigorie et al., 2012a). The experimental results of the nonlinear controllers were presented in (T. L. Grigorie, Botez, Popov, Mamou, & Mébarki, 2012b).
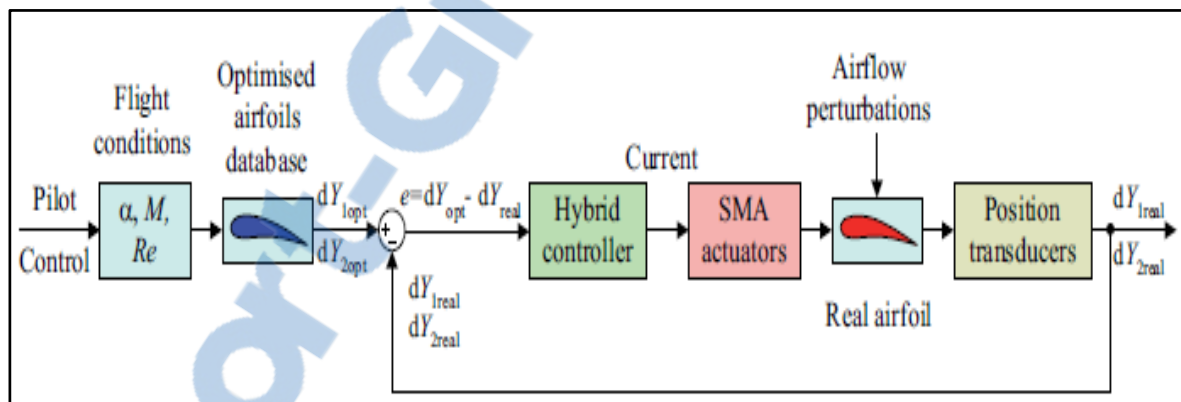
Figure 1.2 Block diagram of the controlled morphing wing system
Taken from T. L. Grigorie et al. (2012a)

In the listed references above, the LARCASE team worked on the CRIAQ 7.1 project called "Controller design and validation for laminar flow improvement on a morphing research wing- validation of numerical studies with wind tunnel tests". In this thesis, we work on the MDO 505 project named "Morphing architecture and related technologies for wing efficiency improvement". The objective is to move the transition point toward the trailing edge by using another type of actuation system and a unique combination of control methods such as Fuzzy and Neuro-Fuzzy logic methods. The previous working experiences in dealing

with problems of morphing wing and actuation system would be a very useful source to consider, and to take it as a reference.

CHAPTER 2

PROBLEMS AND OBJECTIVES

2.1 Problems

In the previous CRIAQ 7.1 project, the wing was idealized as a rectangular box, that had no structural constraints. For that wing, the SMA actuators were consuming a high amount of energy. In the present CRIAQ project, a wing-tip of a real aircraft is considered, that has already structural constraints imposed by its designer and manufacturer (Bombardier). On this wing, electrical in-house actuators were implemented.

In this project, the challenge for the realization of the morphing wing system is that its airfoil needs to improve its aerodynamic performance under different flight conditions. In other words, the system needs to reduce its drag while maintaining constant lift to improve its aerodynamic performance. The most promising approach is to move the flow transition region closer to the trailing edge, which would increase the lift-to-drag ratio. In the implementation of control methods for morphing wing, some of the difficulties that can be anticipated are the nonlinearities of the whole system, and the integration and synchronization of the wing tip control system. Original control methods to solve these problems will be developed and investigated.

2.2 Objectives and Project Description

The CRIAQ MDO 505 project involves two teams of partners from two countries: Canada and Italy. The Canadian team is comprised of partners from the Ecole de Technologie Superieure (Montreal), Ecole Polytechnique de Montreal, Thales, Bombardier, and the Institute of Aerospace Research of National Research Council of Canada (IAR-NRC). The Italian partners are partners from CIRA and the University of Naples Federico II. The main goal of the project was to build a wing-tip controller system of a Bombardier aircraft, and to validate it via wind tunnel and flight tests. The wing tip prototype system, including a

morphing wing and a morphing aileron were designed, manufactured and tested. Various types of actuators and sensors were used to control the morphing wing tip mechanisms of the system, with the following objectives:

- Improving the wing tip-aileron aerodynamic performance at low subsonic speeds;
- Extending a laminar flow region while avoiding massive boundary layer separation.

Wind tunnel test data were collected at the IAR-NRC aerodynamics laboratory to validate the morphing wing-tip system. Numerical investigation of the aero-elastic capability of the prototype was performed by the aerodynamics team to verify the flutter stability boundaries and to eliminate any eventual system buffeting phenomenon occurring at transonic speeds.

The wing tip has been equipped with electrical actuators, and with Kulite sensors that were used to measure the pressures. The main objective of the thesis was to design a robust and reliable control system for the morphing wing tip system. New methodologies presented in this thesis were developed to morph the active structure (skin composite) shape for predefined flight conditions, and to integrate and implement the aerodynamic and structural morphing wing-tip technologies in the control system.

CHAPTER 3

ORIGINALITY AND METHODOLOGY

3.1   Originality

Several researchers have been working on improving the airfoil flow to enhance the dynamic performance of morphing aircraft systems. However, most of the studies have used intelligent materials for the actuation of the morphing systems. The CRIAQ MDO 505 research team decided to use Brushless Direct Current (BLDC) motors for the actuation mechanism. BLDC motors are miniature permanent magnet synchronous motors that offer many advantages such as high flexibility, good controllability, high power density, high efficiency, large torque to inertia ratio, as well as light weight. Compared to Permanent Magnet Synchronous Motors (PMSMs), BLDC motors are less expensive as they have concentrated windings and use Hall-effect sensors, which are cheaper than the position sensors required by PMSMs, such as optical encoders.

This thesis considers, for the first time, using two types of ANFIS controllers to control the actuators in a Bombardier aircraft morphing wing-tip system for both cases; those in which the aileron moves and when it stays still. Both controllers were experimentally tested in a wind tunnel with a morphing aileron installed on a wing. These two controllers, based on a Neuro-Fuzzy methodology, offer promising approaches for actuator control. The first controller is built with trapezoidal-shape input membership function and constant output membership function. The second controller is built with bell-shape input membership functions and linear output membership functions. Maxon industrial drives are used to implement these algorithms into the real-time morphing wing-tip system. The control architecture using National Instruments systems in real time is also proposed and implemented for the first time in the morphing wing-tip system. Problems encountered during the Wind Tunnel Test validation are also mentioned and solved.

3.2 Morphing wing and aileron system

3.2.1 Morphing wing-tip model

The wing-tip model in this project has a chord of 1.5 meters and a span of 1.5 meters, which is equivalent to a full-scaled part of the wing and aileron of a regional aircraft. The wing model is equipped with an aileron, and a morphing skin made of composite materials on the wing's upper surface.

Figure 3.1 indicates the position of the wing-tip model on an aircraft wing, in which the wing-tip part is located between the fuel tank part and its winglet part. Figure 3.2 shows a cross section (airfoil) of this wing-tip model. The ailerons are used to control the aircraft in roll motion (or motion around the aircraft's longitudinal axis). The lower surface of the wing is made of aluminum, and is large enough to accommodate a strain gauge transducer, an actuation system, sensors, as well as a cabling system for these sensors.
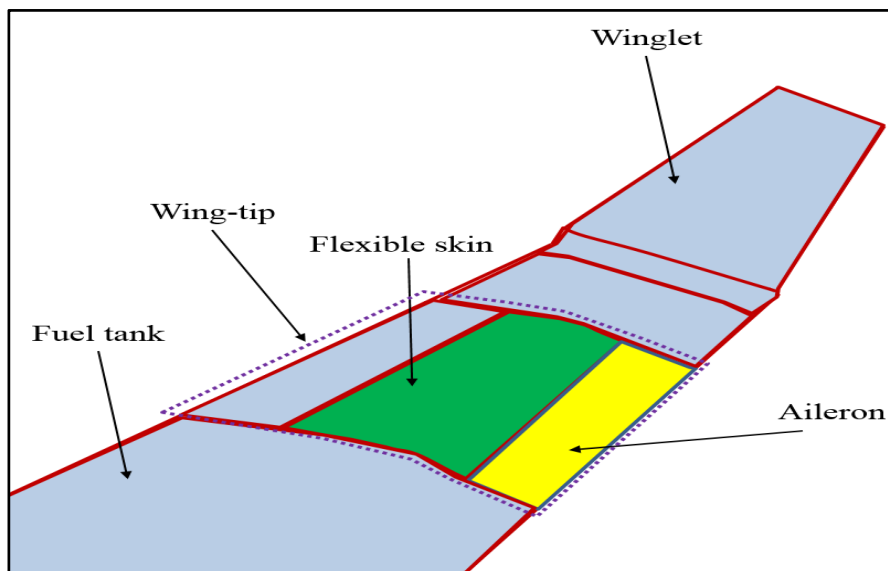
Figure 3.1 Position of the morphing wing-tip on the aircraft wing

The lower surface was produced by the mechanical team of the CRIAQ MDO 505 under the leadership of Dr. Simon Joncas from ÉTS, and in collaboration with Bombardier team. The

morphing wing-tip was designed and manufactured by Bombardier Aerospace as it represented a real Bombardier wing.
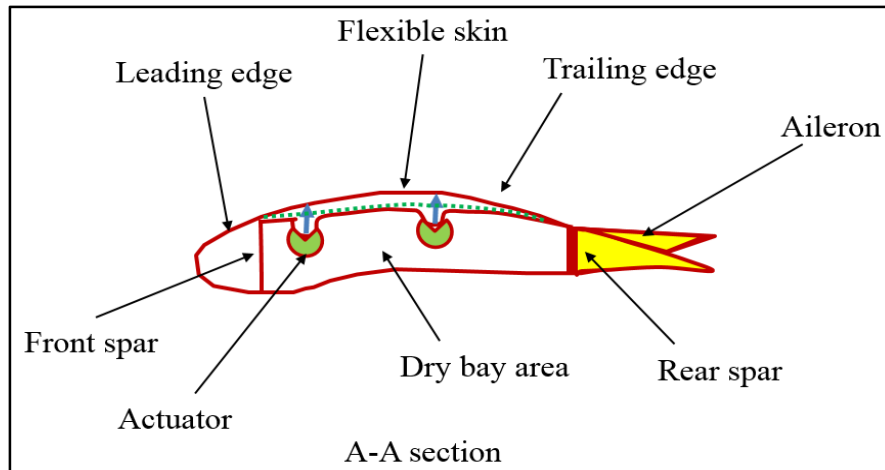
Figure 3.2 Wing-tip structure

3.2.2   Actuators

The morphing wing's actuation system is composed of four actuators fixed inside the wing. Four BLDC motors serve as electrical motion sources, one for each actuator. These Maxon-type motors have the characteristics indicated in Table 3.1. To convert the motors' rotary motion to the vertical motion of the wing's upper surface, each actuator has a gearing system equipped with a nut, which is joined to the shaft of its BLDC motor.

As known, a brushless DC motor is a synchronous electric machine driven by DC electricity. BLDC motors can be used in single phase, 2-phase or 3-phase power stage. The BLDC motors used in the project are constituted as 3-phase power bridges corresponding to, three windings of the stator. Figure 3.3 shows the BLDC motor in its cross section.

Table 3.1 BLDC motor's characteristics

Nominal voltage	12 volts
No load speed	4610 RPM
No load current	75.7milliamperes
Nominal Speed	2810 RPM
Nominal torque (maximum continuous torque)	25.1 millinewton-meter
Nominal current (maximum continuous torque)	1 ampere
Stall torque	84.1 millinewton-meter
Starting current	3.49 amperes
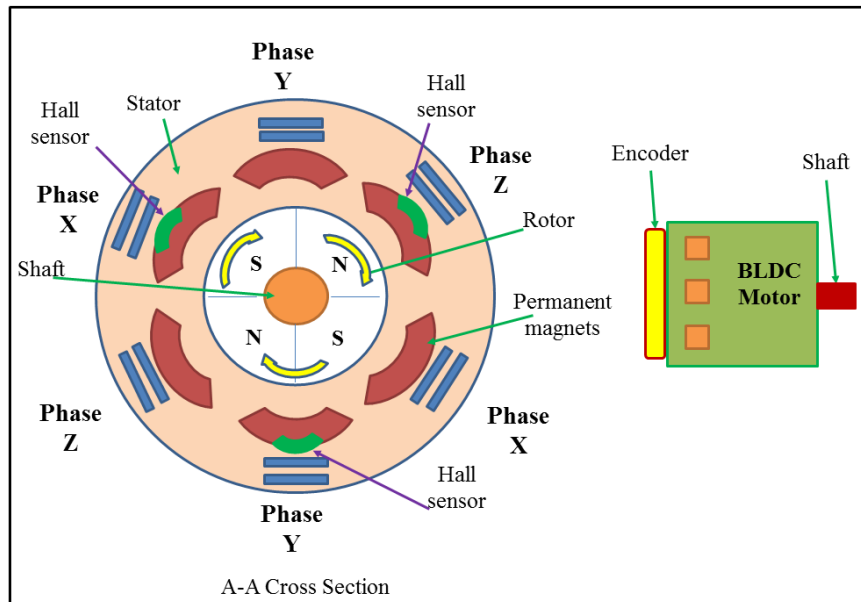
Figure 3.3 BLDC motor

The BLDC motors use the interaction between the stator flux with the rotor flux, generated by permanent magnets, to create the torque. Because of the fact that the rotor flux is induced by the stator poles flux, the stator pole position of a BLDC motor needs to be checked to

control its 3 motor phases. Thus, a 6-step commutation configuration is built by a motor controller. These commutation steps, or commutation phases, help to create a rotational electromagnetic field, which provoke the rotation of the rotor permanent magnets and move the motor shaft. In order to create these commutation phases, six power transistors corresponding to six commutation steps are used for 3 phase's power stages (X, Y and Z). Among these 3 phases, only two phases are active at the same time, the remaining phase stays unpowered (or off). One of these two active phases has positive or negative voltage, while the remaining active phase has negative or positive voltage, respectively, and create 6 commutation steps as shown in Table 3.2. The Hall-effect sensors determine the positions of the rotor. The stator flux vector was based on the positions of rotor to change so that the angle between the stator flux and the rotor flux remains as close as possible to 90 degrees. In that way, the rotor of the BLDC motor keeps moving. Table 3.2 and Table 3.3 shows the 6 commutation phases for two cases: clockwise rotation and counterclockwise rotation. The values of Hall-effect sensors are also presented: 0 means the Hall sensor is inactive, while 1 denotes that Hall sensor is active.

Table 3.2 Commutation Phases for clockwise rotation

Commutation Phases	Hall Sensor X	Hall Sensor Y	Hall Sensor Z	Phase X	Phase Y	Phase Z
1	1	0	0	+	-	Off
2	1	1	0	+	Off	-
3	0	1	0	Off	+	-
4	0	1	1	-	+	Off
5	0	0	1	-	Off	+
6	1	0	1	Off	-	+

Table 3.3 Commutation Phases for counter-clockwise rotation

Commutation Phases	Hall Sensor X	Hall Sensor Y	Hall Sensor Z	Phase X	Phase Y	Phase Z
1	1	0	0	-	+	Off
2	1	0	1	Off	+	-
3	0	0	1	+	Off	-
4	0	1	1	+	-	Off
5	0	1	0	Off	-	+
6	1	1	0	-	Off	+

Figure 3.4 shows the stator flux vectors in the 6-step commutation phases. "XYZ" denotes the Hall-effect sensor output. The green arrows denote the stator flux vectors. Figure 3.5 demonstrates the behaviors of the BEMF motor phases corresponding to the changes of commutation phases. BEMF denotes the Back ElectroMotive Force or the counter Electromotive force of the three motor phases, which is the "voltage or electromotive force created by the relative motion between the armature of the motor and the magnetic field generated from the motor's windings" (Wikipedia, 2017a). S1 to S6 are the six transistors used in the inverter to control the commutation phases. V_{XN}, V_{YN} and V_{ZN} are the voltages of the phases X, Y, Z to Neutral, respectively. V_{dc} is the DC link voltage. Each commutation phase is reassigned every 60 electrical degrees.

The commutation process can be explained as follows : Consider the clockwise rotation for the commutation phase number 1 as shown in Table 3.2, the Hall sensor state is XYZ [100] as seen in Figure 3.4; in other words, the phase X is connected to the positive voltage V_{dc} source by opening the transistor S1 or $V_{XN} = V_{dc}$ (see Figure 3.5); the phase Y is connected to the negative voltage $-V_{dc}$ by opening the transistor S5 or $V_{YN} = -V_{dc}$, the phase Z is off and unpowered (see Figure 3.5);. When the rotor moves to a particular position, the Hall sensor's state changes its values from the previous state XYZ [100] to the next state XYZ

[110] as seen in Figure 3.4, and the corresponding voltage is applied to each phase as shown in Table 3.2.
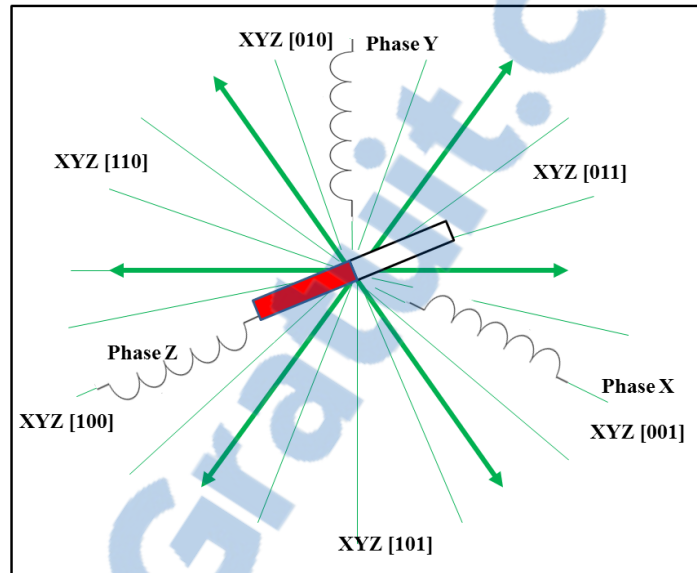
Figure 3.4 Stator flux vectors
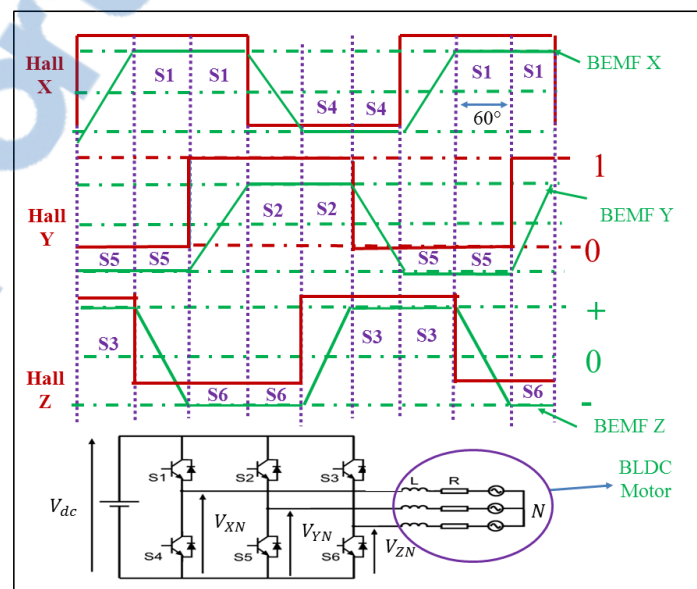
Figure 3.5 Six step Hall sensor outputs
and motor phases

In order to control the speed and direction of the motor, Hall-effect sensors plays a very important role. However, the Hall-effect sensors do not offer the real time angular position feedback when it can only provide information for each 60° movement in the rotor's position and within each electrical cycle. Thus, here encoders are used to compensate the drawback of Hall-effect sensors. The Hall sensors are used for the commutation of the BLDC motor, while the encoders track the position, speed and rotation of the motor, and convert the angular position to an analog/digital code or a pulse, and send it to the BLDC drives (in this project the BLDC drives are the Maxon drives). A BLDC controller is then used to control the active state of the transistors (open or closed) based on the signals received from the encoders and Hall sensors.

Figure 3.6 shows the way in which actuators are attached inside the wing. This figure also shows the positions of the four actuators, and the cabling system inside the wing.
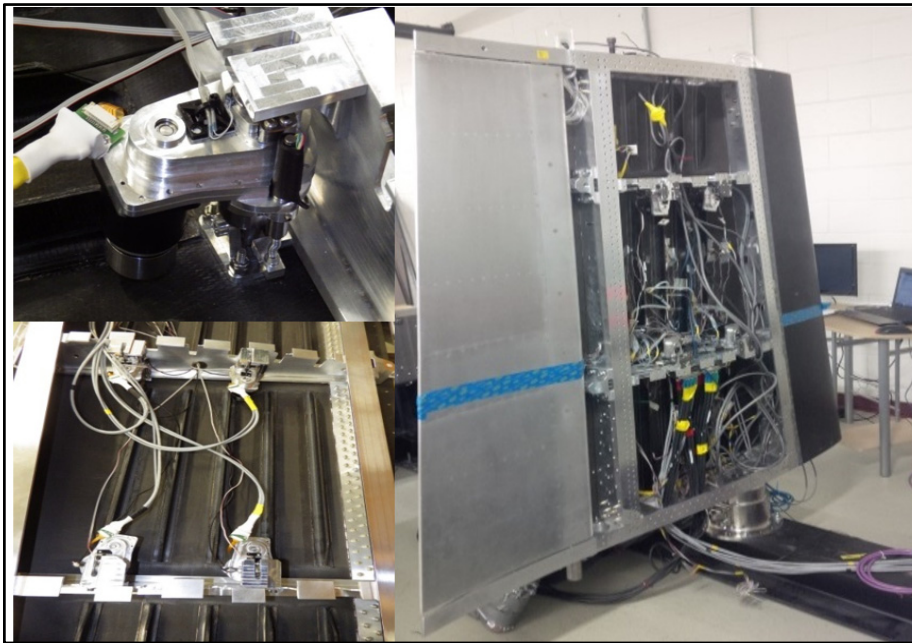
Figure 3.6 The wing-tip model with actuators and cabling system

3.2.3   Sensors

Control methods are implemented in the actuation system with the aim to change the surface of the wing until it reaches its desired optimal shapes. The desired wing surface displacements were calculated by our aerodynamic team to achieve the optimum airfoil wing shapes. The displacements differ as a function of Mach numbers (M), angles of attack (α) and aileron deflection angles (δ_{ail}). In the control loop, as shown in Figure 3.7, the morphing wing-tip system is controlled by the position feedback signals received from the LVDT sensors. The LVDTs (Wikipedia, 2017b) are a kind of electrical transformers, which are used to measure linear positions, thus wing surface displacements. The sensors are attached along with the piston of the actuators so that any movements of the actuators are recorded and observed. Figure 3.8 shows an actuator with this LVDT mechanism. In our research, the LD340-6 series are used with a range of mechanical travel of ± 6mm (wing skin displacements). These values of ± 6mm were chosen as function of the aero-structural interactions and were calculated by the aerodynamic and structural teams. The specifications of an LD340 can be found in (Omega, 2014).
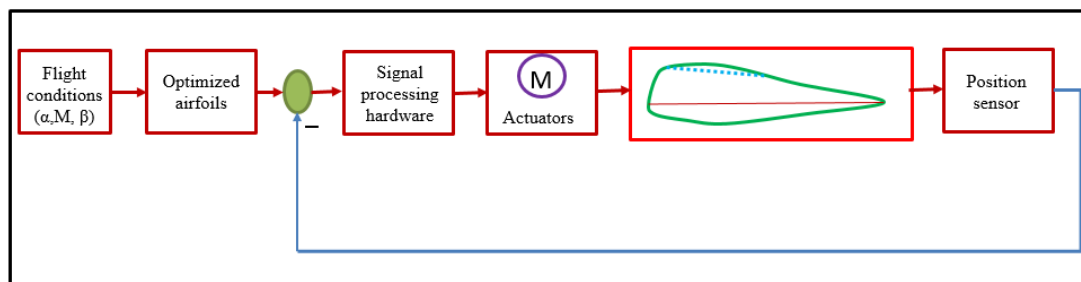
Figure 3.7 General principle of the closed control loop
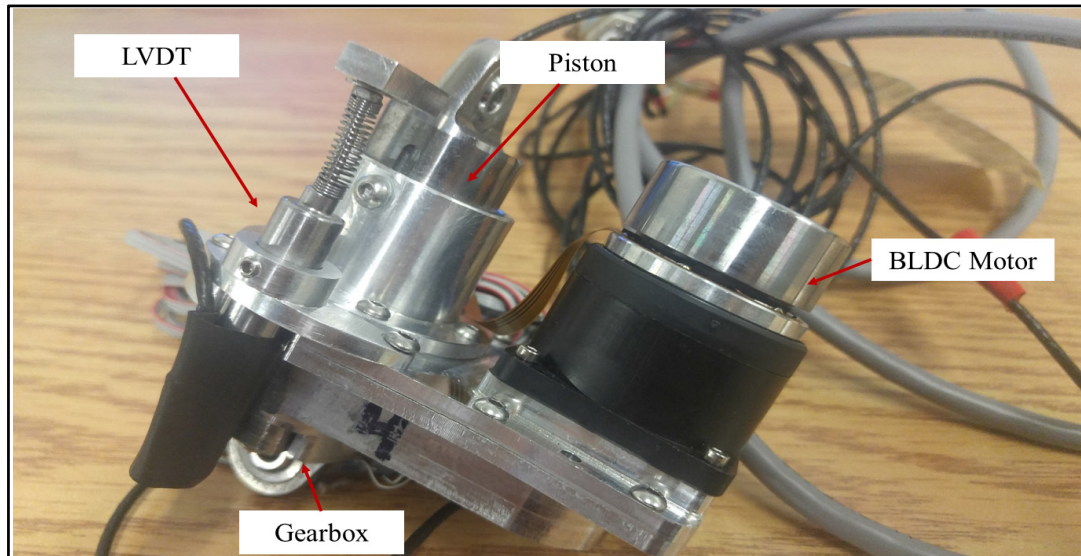
Figure 3.8 An actuator with LVDT sensors

To observe the behavior of the morphing wing's skin and to evaluate the improvement of the system's aerodynamic performance, Kulite sensors are used to record the pressure changes on the skin surface. The Kulite sensor is a kind of pressure transducer that generates an electrical output proportional to the measured pressure. The sensor systems were tested earlier in the *Price Païdoussis* Subsonic Wind Tunnel at the LARCASE, along with a demonstration model of the morphing wing's upper surface. In our research, we used 32 Kulite XCQ-0162 series sensors to measure pressures of a 0.35 to 5 psi range. The Kulite piezoelectric sensors are also used to detect the flow transition from the laminar to turbulent regimes. The specifications of such a Kulite sensor is shown in (Kulite, 2015).

3.2.4   Ailerons Control

The motions of the aileron actuation system are less complicated and easier to control than those of the wing. The deflection range of the aileron is between -6 to +6 degrees. This range of the aileron was determined by aerodynamic constraints and security limitations in the wind tunnel. Two types of ailerons were considered: a rigid aileron, which was built by a Canadian team, and a morphing aileron, which was designed, manufactured and controlled by an Italian team. The type of aileron did not affect the movement of the morphing wing

skin because ailerons were controlled separately by their controller systems, which were different from the wing's actuation system. The aileron actuation system is presented in details in the next section 3.3. The system controlling the shape of the morphing aileron was designed and manufactured by the Italian team. The system controlling the interaction between the morphing wing and the aileron (rigid or morphing) is described in Section 3.4.

3.3 Operating System Hardware and Software

This section presents the hardware and software that we used to carry out the wind tunnel tests. All equipment used to control the morphing wing-tip system is shown in Figure 3.9, as it is configured in our LARCASE laboratory. Two kinds of industrial communication networks are used in the system: Ethernet and CAN.

Ethernet is a link layer protocol that is used to connect the real-time operating system in the embedded controller, NI PXIexpress-8135, with a Host PC and the Kollmorgen Drive, which is used to control the movement of the aileron.

The other connection network, CAN network, is used to connect the Maxon drives (EPOS 24/5) with the embedded controller. The communication issues among these different types of equipment are discussed and presented in detail in (Guezguez, 2016). In this thesis, we describe the general concept and purposes of the equipment in the system in a limited extent. Thus, the system includes:

1. NI SCXI-1000 & SCXI-1540 Add-on LVDT Conditioning Modules, which filter and process LVDT signals.

2. NI PXIexpress-8135 is an embedded controller for the PXI express system, which is used for system computation. To monitor the embedded controller to control program deployment, system state and data logging, a Host PC is connected via an Ethernet network using a TCP/IP communication protocol.

3. Maxon drive EPOS2 24/5 (Easy to use Positioning System, second generation, 24V-5A) is a "small-sized, full digital smart motion control unit" (MaxonMotor, 2016). This drive is used for positioning of BLDC motors with digital Hall-effect sensors and encoders. The drive is designed as a "slave node" in a CANopen network, and can be monitored via any USB or RS232 connection. In this research, we use a Maxon drive as a supported controller because of its functionality in reducing torque ripple, its low noise and its integrated current and speed control. Ten modes are implemented in the drive, including "homing mode", "profile position mode", "profile velocity mode" and "position mode". We used the position mode for our work. In this mode, we can set a new value for the position control loop without setting up a new profile, which makes easy the control of the motion of the actuators (MaxonMotor, 2014).

4. The CPX400 power supply provides a fixed 24V for each BLDC motor.

5. The computer screen of the Host PC is used to observe the connection between devices and to visualize the real-time system/hostPC deployment process.

6. Kulite add-on Conditioning Modules, which filter and process Kulite signals.
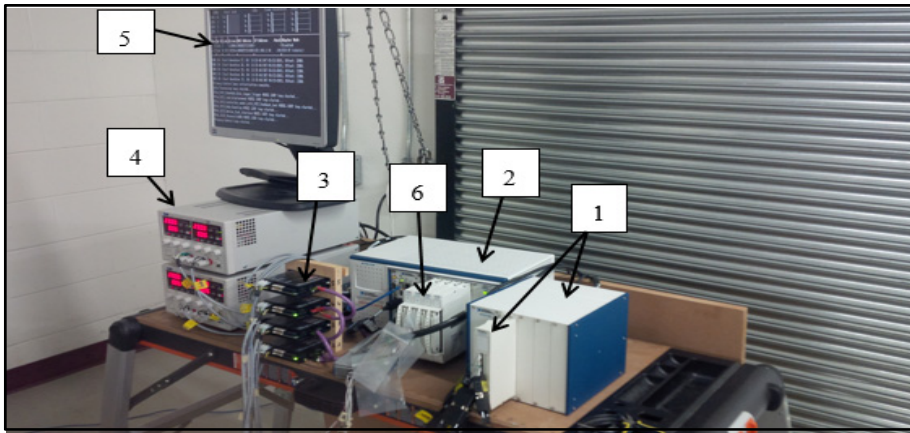
Figure 3.9 Equipment used in the morphing wing-tip system

Because we have two kinds of ailerons, the equipment used to control these ailerons is also different. For a rigid aileron, its motions are controlled by a BLDC servo motor supported by a Kollmorgen® drive. In the same way as the other BLDC motors, these motors use Hall-effect sensor feedback to detect the rotor's position and initiate power stage phases. Encoder sensors provide the position and speed feedback in real time and give the drive the precise angular position and speed of the motor.

The motor is then controlled by a Proportional Integral Derivative (PID) algorithm implemented in the Kollmorgen® drive to reach desired deflection aileron angles. Because of the fact that we only need to deflect the aileron for a certain number of predefined aerodynamic shapes, we decided to create sets of fixed aileron positions. The "motion task" feature in the Kollmorgen® drive allow us to create the sets of desired displacements, speed that assist the aileron actuation system to reach the desired deflection angles. The user then only needs to input the motion task number on an Ethernet interface, and the actuation system moves the aileron to its required position.

When using a morphing aileron, a DSPACE DSP controller was used to move the aileron. The DSPACE system has its own graphical interface. The real-time control strategy was developed using MATLAB/Simulink software, and then is converted into C code using the C/C++ compiler. The code was implemented into the DSP board, and allows the user to control the system in real time.

The whole wing-tip system and the ailerons are shown in Figure-A I-1 and Figure-A I-2 in ANNEX I. The software used to carry out the experiments is listed in Table 3.4.

Table 3.4 Software List

Software Name	Description
Matlab® Simulink	Used for control modeling; these control models will be further integrated with NI-VeriStand® to control the system in real time.
LabVIEW®	Used for developing custom devices in order to acquire the required signals. LabView® is also used for developing models integrated with NI-VeriStand®
NI-VeriStand®	Used for real-time testing applications. The main objective is to configure the real-time engines to implement tasks such as data acquisition, conditioned measurement, etc. NI-Veristand® also allows users to deploy/import control models, and to create run-time interfaces with the real-time equipment of National Instruments.

Each software package and its function in our experiments is presented in detail in the following paragraphs. The main software used to control the real time testing is NI-Veristand, from National Instruments. It provides us "a framework for real-time testing applications" (NationalInstruments, 2015b). Figure 3.10 gives an overview of the NI Veristand architecture, inspired by the introduction of NI Veristand (NationalInstruments, 2015a, 2016). This architecture includes three windows on the Host Computer/PC: the Workspace, the System Explorer and the Stimulus Profile Editor. The Target, which here is NI-PXIexpress-8135, has the mission of hosting the definition files and running the NI Veristand Engine.
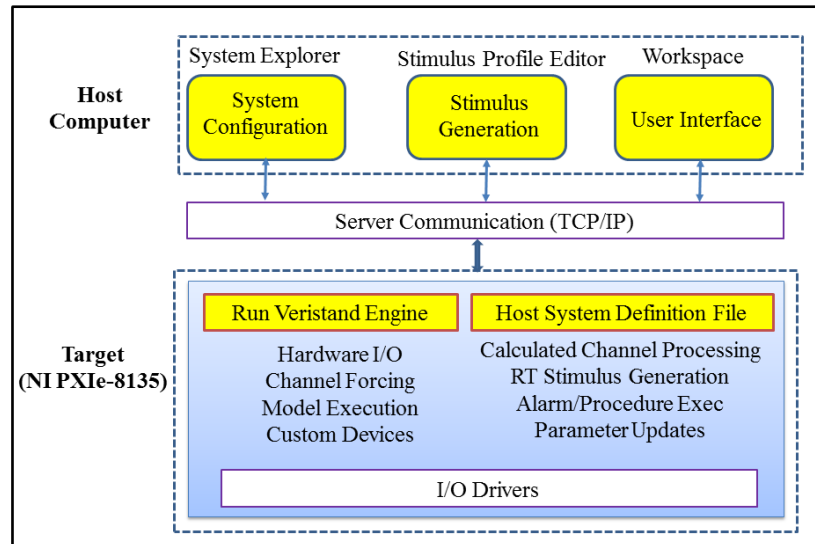
Figure 3.10 The NI Veristand architecture
Adapted from National Instruments (2015a, 2016)

Several important definitions of this architecture are listed below:

1. System Explorer

The purpose of the window is to create a system definition. All of the settings such as hardware I/O (Input/Output), the functional models imported from LabVIEW and Matlab/Simulink, etc.… are created and edited in the System Explorer. The system definition file, therefore, includes the running rate of the system, data acquisition devices, channel configurations, simulation models, active alarms and procedures, as well as system mappings. We present here several key sections in the system definition file:

- Targets: Contains the targets in which we want to deploy our program. Additional Hardware (I/O) can be added here, including DAQ and FPGA. In our experiments, the Target is NI-PXIexpress-8135 with the additional modules NI SCXI-1000, SCXI-1540 Add-on LVDT Conditioning Modules and Kulite Modules;

- Simulation Models: "Mathematical representation of a real-world system" (NationalInstruments, 2015a). These models are created separately in Matlab/Simulink. Inputs/Outputs of the models are assigned to the Inports/Outports on a Target via System Mapping, and to operate the real-time control of the targets;

- System Mapping: Links the source with destination channels or custom devices;

- Custom Devices: Channels/modules that are created to serve a specific purpose. LabVIEW is used here to create Custom Devices for the sensor data acquisition;

- Calculated Channels: These channels are used to modify the values of other system channels according to the calculated requirements of the user such as calibrated values of LVDTs;

- Active Alarms/Procedures: Utilized to inform the user about current events and to show the list of actions that can be executed on the Target.

In order to implement the system definition file on the Target, the Veristand Gateway is used, which creates a TCP/IP communication channel to communicate with the VeriStand Engine and synchronizes with the definition file that is currently running on the Target.

2. Stimulus Profile Editor

The Editor is a tool to create stimulus profiles, which allow users to execute desired tasks and tests deployed in the Veristand Engine in an automated way. Users can create lists of steps, loop structures, variables and conditional statements that they want the NI Veristand Engine to perform. Users also can assign multiple logging tasks, independent logging rates and trigger conditions to their stimulus profiles. We use Stimulus Profile Editor to perform the automated calibration process, which is discussed and presented in Chapter 4.

3. Workspace

The Workspace is a kind of user interface, which allows users to carry out their real-time tasks. The system definition is deployed here, so that users can drag-and-drop different objects for different purposes in the run-time user interface, and then map the objects to their desired channels. The workspace or the user interface used in the Wind Tunnel Test is shown in Chapter 4.

4. NI Veristand Real-time Engine

This NI Veristand Real-time Engine is a "non-visible execution mechanism" (NationalInstruments, 2015c) that monitors the timing of the entire system and the communication issues between the Host PC and the Target. This Engine has multiple time loops using real time FIFOs (First In-First Out) mechanisms to transfer data packages between the them. It also decides which system definition file is allowed to run and carries out the execution of hardware I/O, models, test, procedures, etc. in this system definition file.

3.4   Controller Design and Actuation System

This section introduces the controller design and the actuation mechanism of the morphing wing-tip system. A portion of this work has already been published (D. H. Nguyen, Tchatchueng Kammegne, & Botez, 2015; D. H. Nguyen, Tchatchueng Kammegne, Botez, & Grigorie, 2016).

3.4.1   System Control Architecture

Figure 3.11 indicates the general architecture of the whole controlled morphing wing-tip system, showing the morphing wing-tip system with a rigid aileron. The architecture is similar to the case using a morphing aileron, except that the morphing aileron control is performed with a DSPACE system, as shown in Figure 3.12. The morphing aileron was controlled by the Italian team involved in the CRIAQ MDO 505 project.

The system introduced here has three main parts: the morphing wing-tip and aileron, an NI real-time controller (PXIe-8135) and its extended modules, and the Host PC. In the NI real-time controller, NI Veristand Custom Devices are created to acquire the pressure data from Kulite sensors and the position feedback from LVDT sensors. The actuation system inside the morphing wing-tip is monitored by a Host computer via an NI Veristand Workspace/GUI.

All of the current system's status is shown in the GUI so that the users know the current positions of the whole actuation system. After the deployment of the whole system on the Target, the desired positions are set by the users and sent to the wing and aileron controller, which sends instructions to the NI Custom Devices of their position sensors and their drives. The drives then convert the digital commands into analog and transfer these signals to the actuators. The position feedbacks of the actuators are transmitted to the custom devices before being sent back to the controllers for monitoring purposes. All of the data is recorded via data logger under a data logging command in the Host PC.
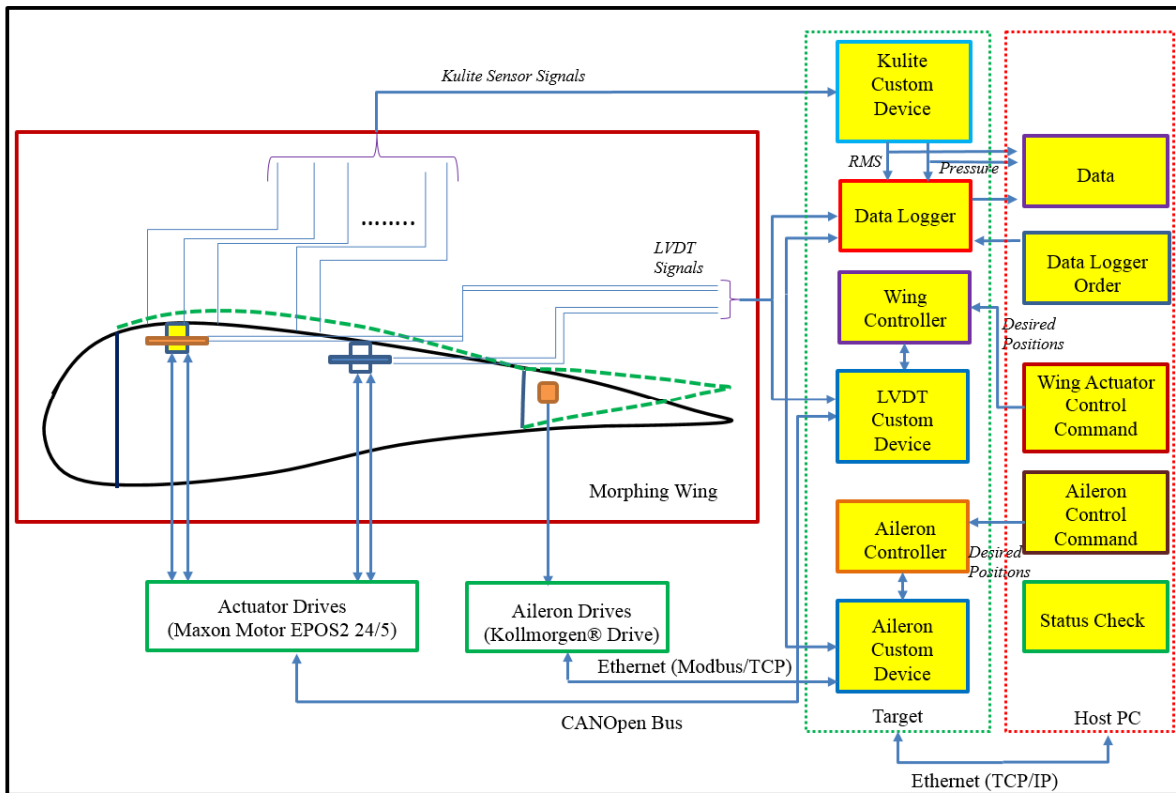
Figure 3.11 General architecture of the morphing wing and rigid aileron controllers

In the morphing aileron case, due to the differences in the actuation systems and digital signal processing hardware/software of the aileron motion controllers, we decided to control the actuation systems of the morphing wing and the morphing ailerons separately. This

means that the ailerons are settled into predefined fixed positions before we start moving the upper skin of the morphing wing.
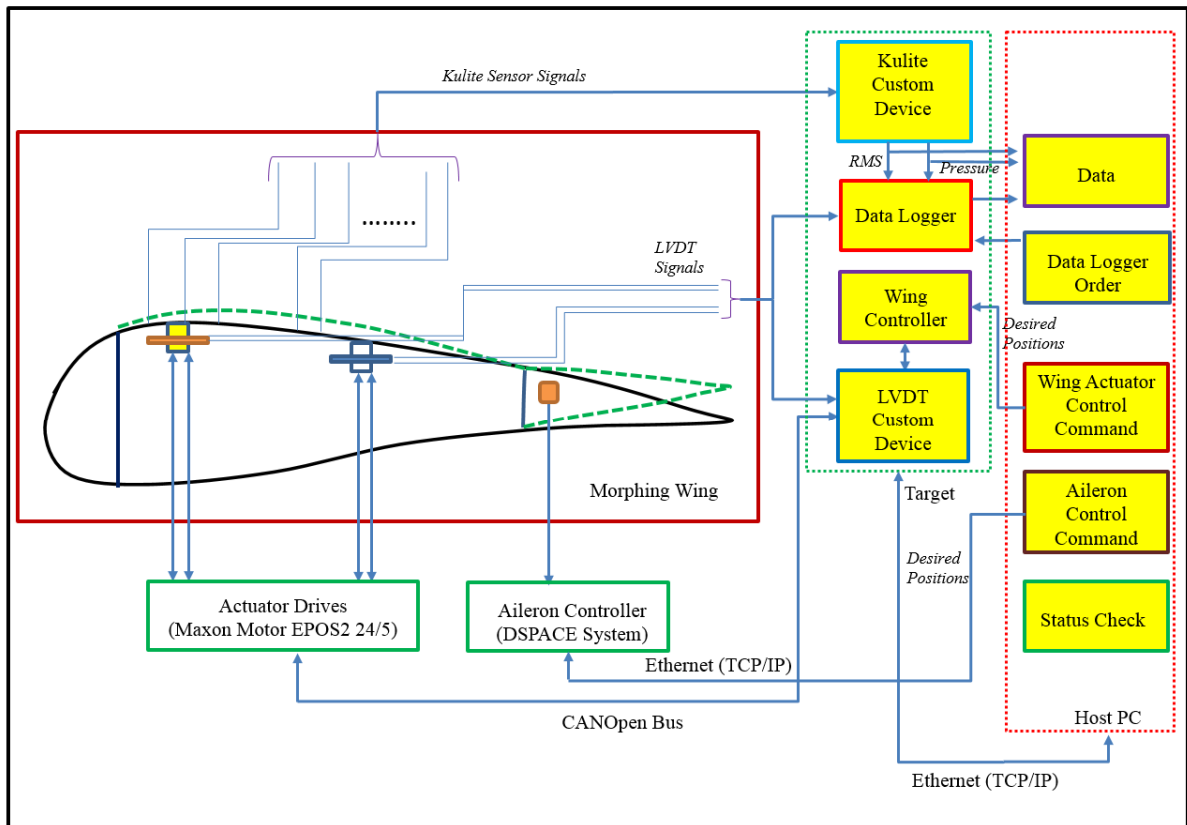
Figure 3.12 General architecture of the morphing wing and
morphing aileron controllers

Before going into the details of the controller design for each actuator, we first investigate the behaviors and performance of the system. In this investigation, we considered two cases: the case in which the actuation system was not controlled, in other words, only the position feedback was considered and the controller using ANFIS methodology was not implemented and trained; meanwhile in the second case, the actuation system was controlled by our trained ANFIS controller and the position feedback. The results presented in Figure 3-13 shows the differences between the desired and the real displacements resulting in these two cases (using and not using our trained ANFIS controller). It can be seen that the system performs much better when the controller is implemented. Figure 3.14 presents the behavior

of an actuator in real life when several displacements are applied. It is obvious from Figure 3.13 and Figure 3.14 that the system could not achieve the desired displacements and was unstable when the controller was not implemented.
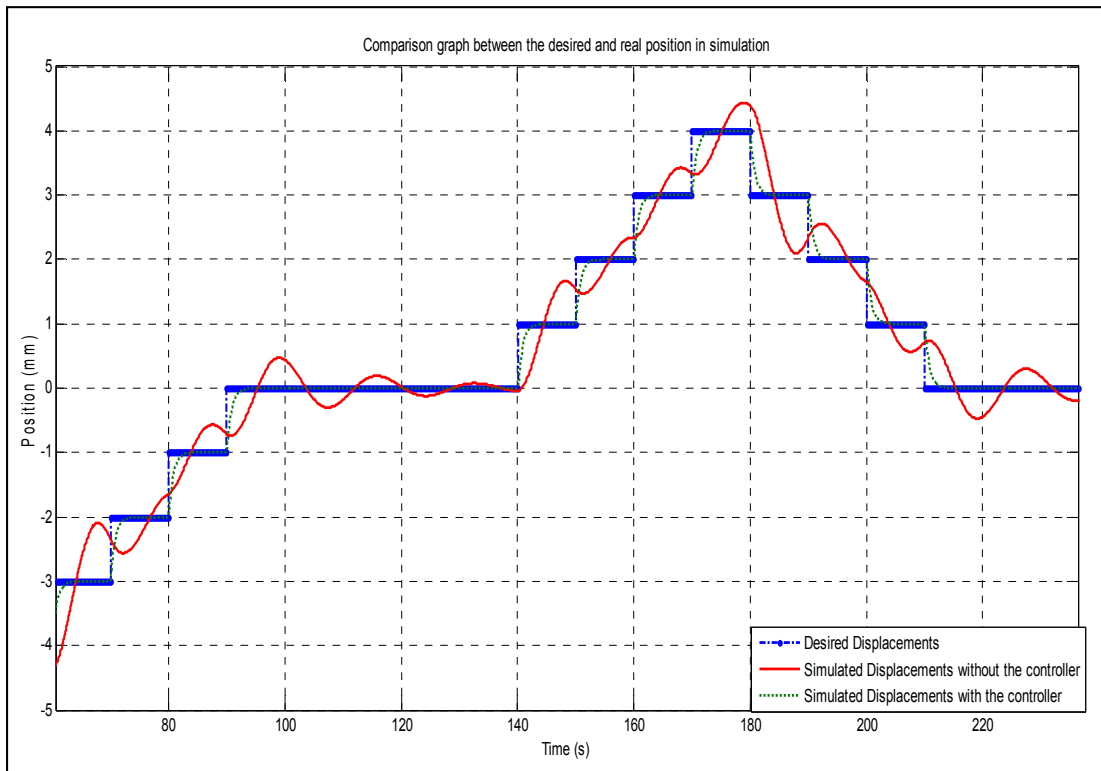
Figure 3.13 Simulation results of the desired versus simulated displacements
with and without a controller
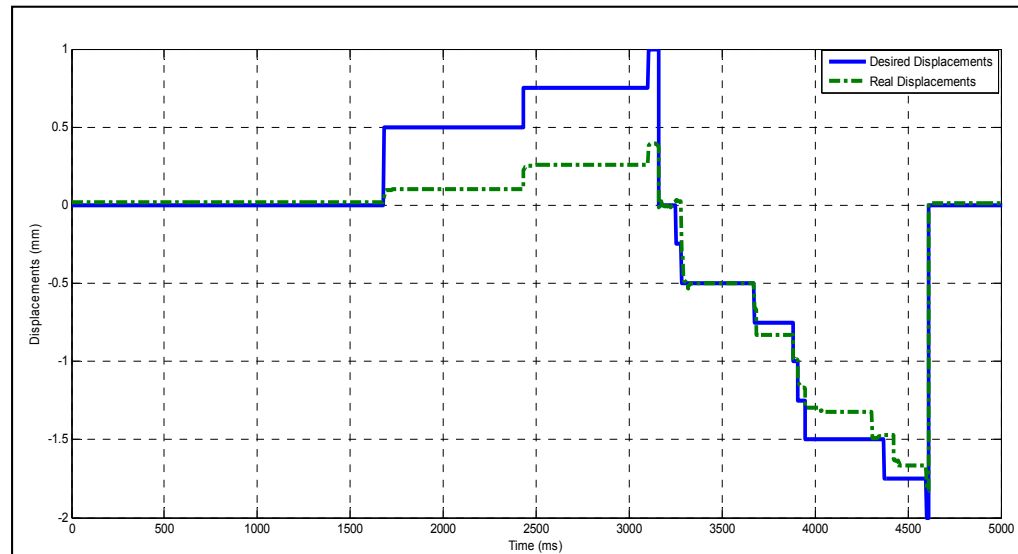
Figure 3.14 Bench test results without using a controller

3.4.2 Actuator Control Architecture

The control architecture design for each actuator is shown in Figure 3-15. The differences between the desired displacements and the LVDT feedback signal to control the actuator. As noted earlier in the Actuators sub-section and Hardware sub-section, Maxon drives are used to collect the data from the output of the controller; then pulses are created and send them to the BLDC motors. The motors receive the signals, rotate and then create the vertical motion corresponding to the rotary motion via a mechanical mechanism. This mechanism includes a piston and a gearbox as shown in Figure 3.8.

To compensate for the mechanical play inside the actuators, the exact position of the motor is sent back via the encoder (as introduced in the Actuators sub-section, the encoder is a part of the BLDC motor and is attached on its outside) and summed up with the controller output before being sent back to the drive. The communication between the EPOS2 drive and the real-time NI controller is done via the CANOpen telecommunication protocol. In this way, the motor updates the actuator's current position and keeping it moving until the actuation system reaches the required skin deflections position.
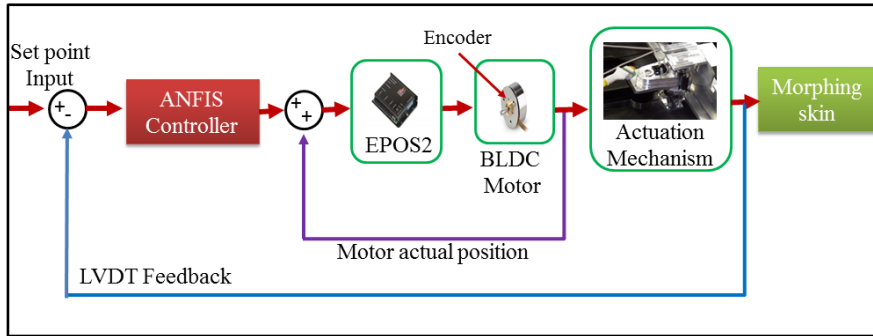
Figure 3.15 Control architecture of an actuator

In order to implement the control architecture in real time system, we build a Simulink model for each actuator, convert it into C/C++ language code and load it into the NI PXI-Express controller using the NI Versistand software. This model runs at the same frequency as the operating system's execution frequency (100 Hz), so that the system can run synchronously in real time, allowing the ANFIS controller to keep changing, and recomputing the input until the required position is obtained by the actuation system.

Figure 3-16 presents a schematic of the control architecture for an actuator in Matlab/Simulink, in which there are three inputs and one output. The architecture is similar when we apply it to all four actuators. The "Set point" input denotes the desired displacement input, and the "LVDT Feedback" input receives the position feedback from the actuation system via an LVDT sensor. The "Motor actual position" input obtains the exact angular position of the BLDC motor from the encoder. That angular position value is converted into a signal for the Maxon drive unit via the "Motor/Drive Conversion", which is determined by the Maxon manufacturer: One turn of the BLDC motor is equal to 24 signal states or units, which are also called quadrature counts or quad counts (qc) (MaxonMotor, 2014). For example, the motor must make 100 turns or 2400 qcs to move 1 mm on the flexible skin. The output of this controller is the "Drive Input", which is simultaneously the input of the BLDC motor drive EPOS2.
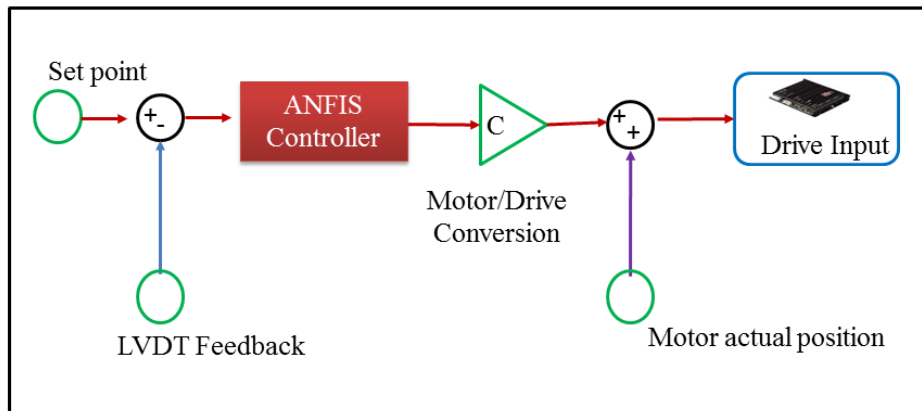
Figure 3.16 Control architecture in Matlab/Simulink

3.4.3 Adaptive Neuro-Fuzzy Infererence System (ANFIS) Control Methodology

As discussed in the previous section, it is important that the controller in the control architecture can adapt to changes in the actuation system. Therefore, we chose Adaptive Neuro-Fuzzy Inference System (ANFIS) as our control methodology. Before going deeper into the design of our ANFIS controller, we provide a brief introduction to fuzzy inference systems.

Fuzzy inference systems, known also as Fuzzy Controllers, normally include four important blocks as shown in Figure 3.17.
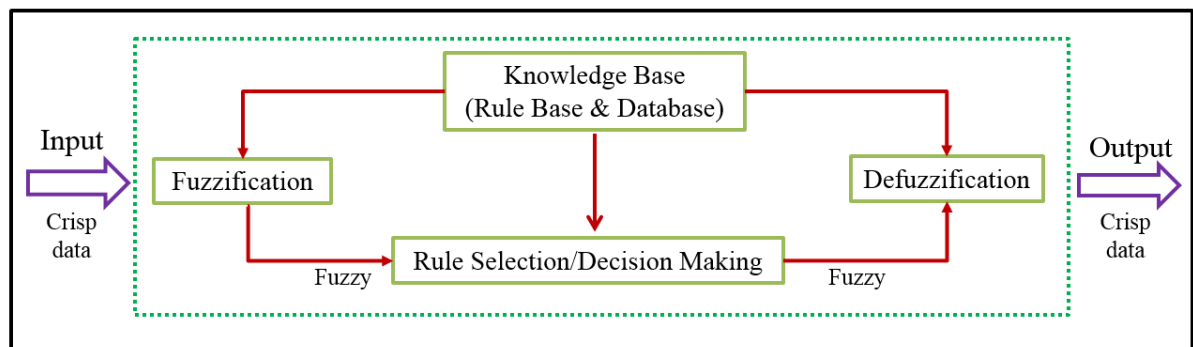
Figure 3.17 Fuzzy Inference System
Adapted from (Jang, 1993)

The details of the four blocks are described below:

- Fuzzification block: Converts the crisp input data into linguistic data or membership functions;

- Knowledge base block: Includes the "rule base" and the "database". A "rule base" contains the IF-THEN rules and the "database" consists of the membership functions of the fuzzy sets;

- Rule Selection/Decision Making block: Selects which rules are to be applied into the fuzzified inputs;

- Defuzzification block: Converts the fuzzy inference results into crisp output data.

Depending on the type of *fuzzy reasoning* (or *inference operations upon fuzzy if-then rules*) and IF-THEN rules implemented, fuzzy inference systems can be categorized into three types (Jang, 1993):

- Type 1: In this type, the output is calculated by calculating the weighted average values of each rule's crisp output;

- Type 2: The overall fuzzy output is found by choosing the "max" values in the fuzzy outputs. The overall crisp output is then determined based on the overall fuzzy output using maximum criterion, mean of maxima, etc..;

- Type 3: This type uses Takagi and Sugeno's fuzzy IF-THEN rules (Takagi & Sugeno, 1983), and is the type used in the ANFIS controller. Each rule's output is calculated by a linear combination of its input variables. The overall output for all rules is then calculated by the weighted average of the outputs of each rule.

ANFIS is a mixture between fuzzy logic inference systems and neural network theories, developed in the 1990s and built on first-order or zero Takagi–Sugeno (T–S) type systems. By combining neural network and fuzzy logic techniques, the method is able to take advantage of both approaches. Neural networks have the ability to learn from given data. However, the results obtained from Neural Networks are not easy to interpret and understand. Fuzzy logic techniques do not allow for self-learning, but it is possible to discover the meaning of their results by using IF-THEN rules and linguistic terms. ANFIS

has been developed and introduced in various control applications (Abraham, 2005; Mohdeb & Hacib, 2014; Prabu, Poongodi, & Premkumar, 2016; Premkumar & Manikandan, 2014).

The structure of the proposed ANFIS controller is similar to the structure of other fuzzy inference systems, as it contains four blocks that are shown in Figure 3.17 and Figure 3.18. "Crisp data" denotes the inputs that users put into the controller, and is supposed to be in the form of real numbers, such as the desired positions of the actuation system. The translation of the "crisp data" into linguistic variables is carried out using input membership functions via the fuzzification block. The rules, or the control logic of the system, is contained inside the rule base/knowledge base block. The choice of the rules is finalized in the "Rule selection" block using Neural Network methods. The "Defuzzification" block converts the linguistic output variables or the rules into crisp output values using output membership functions.
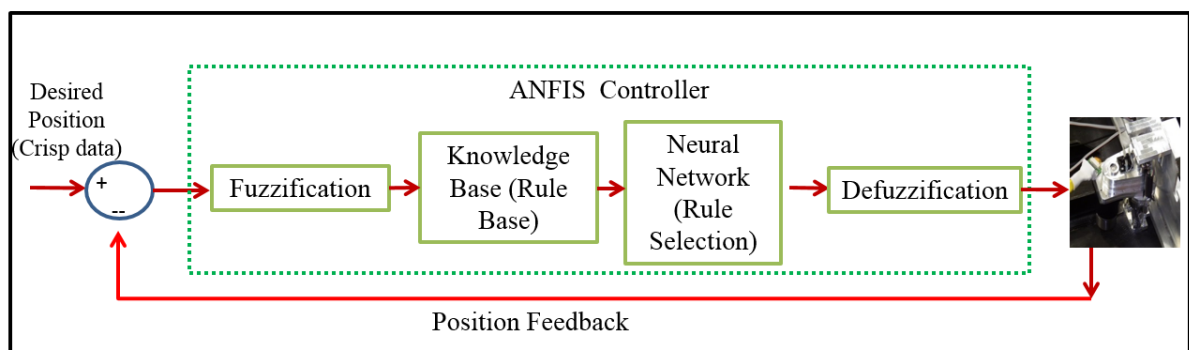
Figure 3.18 ANFIS block diagram
Adapted from (Jang, 1993)

In the proposed ANFIS controller, for the sake of simplicity, one input and one output are used, so that the IF-THEN rule of Takagi-Sugeno can be written as shown below:

$$\text{If } x \text{ is } A_j \text{ Then } y_j = \text{f}(x) = a_j x + b_j \tag{3.1}$$

where x is the crisp input variable, and A_j is the jth linguistic variable that corresponds to the crisp input variable, $j = 1:p$ where p the number of the linguistic variables; in this case, p is also the number of the rules. All of the A_j values are contained in A - a fuzzy

membership set of the input variable x; a_j, b_j are the "consequent parameters" of the crisp input variable x and the jth linguistic variable; y_j is the consequent linear polynomial function associated with the crisp input x and the jth linguistic variable A_j. These parameters will be investigated in more detail in the incoming sections.

The mathematical representation of the ANFIS structure can be divided into layers as shown in Figure 3.19. Signals from the output of a previous layer are introduced into the next layer as the input signals. The output of the ith fuzzy input node of the layer k is called $L_{i,k}$. The number of linguistic variables is equal to the number of fuzzy input nodes $i = j$; thus $L_{j,k} = L_{i,k}$. A detailed description of the layers is given below:

1. Layer 1: Input variables

This layer includes "adaptive nodes" or "changeable nodes". It determines the shape of membership functions such as triangular, trapezoidal, Gaussian and bell-shaped. All of the nodes in this layer are defined by a "node function", which classifies the membership function levels of the inputs:

$$L_{j,1} = \alpha_{A_j}(x) \tag{3.2}$$

where $L_{j,1}$ is the membership function or grade of A_j, and $\alpha_{A_j}(x)$ is defined by the shape of input membership functions such as trapezoidal, bell-shaped membership functions, etc.... The parameters used to calculate $\alpha_{A_j}(x)$ are called the "premise parameters" (Jang, 1993).

These initial values of the "premise parameters" are determined using "grid partition clustering method" and then they are updated using "training data" to obtain their optimized values. The training process will be described in the next sub-sections.

2. Layer 2: Membership

This layer includes the fixed nodes labeled *Pro* in Figure 3.19 that represent the weights of the associated rules. The weights are calculated as the product of the incoming signals from Layer 1. In this case we have one input, thus:

$$L_{j,2} = W_j = \alpha_{A_j}(x) \times 1 = \alpha_{A_j}(x) \tag{3.3}$$

The node function (the output function of the layer) can also be represented by a triangular norm (T-norm) in the form $T_{AB} = T_A \times T_B$ or *AND* operator as noted in Figure 3.20.

3. Layer 3: Normalization of weights

This layer contains fixed nodes labeled *Nor* (normalizing) in Figure 3.19. The node function computes the ratio of the jth rule's weight W_j to the sum of all the rules' weight $\sum_j^p W_j$ using the formula below :

$$L_{j,3} = \overline{W_j} = \frac{W_j}{\sum_j^p W_j} \tag{3.4}$$

This layer can also be called the "rule layer" because it calculates the activation level for every rule, and then matches the fuzzy rules corresponding to each activation level.

4. Layer 4: Defuzzification layer.

This layer determines the layer output values according to the rules' inference. This layer consists of adaptive nodes, with the "node function" provided by the following formula:

$$L_{j,4} = \overline{W_j} \times y_j = \frac{W_j}{\sum_j^r W_j} \times (a_j x + b_j) \tag{3.5}$$

The parameters a_j and b_j are referred to as "consequent parameters" (Jang, 1993). The initial values of these consequent parameters are set at 0, and then are updated using the "training data" in the same way as the "premise parameters".

5. Layer 5: Output layer

The output layer collects the inputs of the layer 4, and transfers them into the crisp format values called y in Figure 3.19. The overall output is calculated by the equation:

$$y = Output = L_{j,5} = \sum_{j=1}^{p} \overline{W_j} \times y_j = \sum_{j=1}^{p} \frac{W_j}{\Sigma_j^p W_j} \times (a_j x + b_j) \tag{3.6}$$
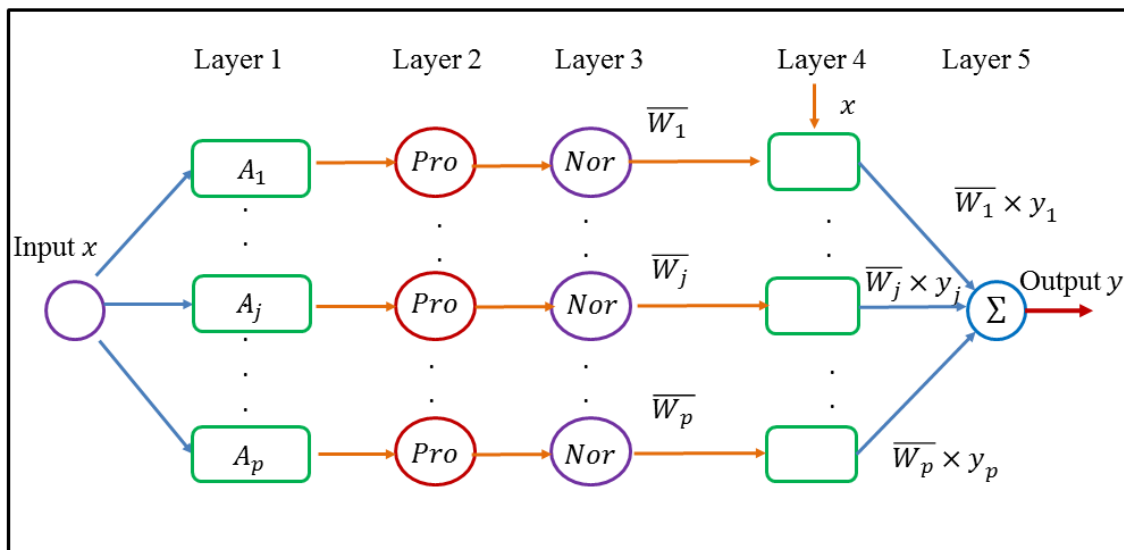
Figure 3.19 ANFIS Control Layers

The control layer structure in Figure 3.19 can be simplified by using a T-norm *AND* operator as shown in Figure 3.20. Because of the fact that only one input x is used, to simplify the layer structure, the two layers number 2 and 3 are combined into one layer AND/Nor as shown in Figure 3.20. In an ANFIS control layer structure, the variability range for each variable and membership function type must be determined. The type of the input membership functions depends on the user's choice of the membership function shape. We are able to exploit this ability to choose the shape of the membership function and thereby compare two types of the ANFIS control methodologies– those with trapezoidal and those with bell-shaped membership function. A ANFIS control system may have many inputs, however, it must have a single output to guarantee the action synchronization of the control system, and has "no rule sharing" to avoid the action confusion that may occur in the control

system. In other words, different output membership functions have different rules. The output membership functions must be homogeneous and should have *constant values* or have *linear dependencies*, which depend on varied range of the output.
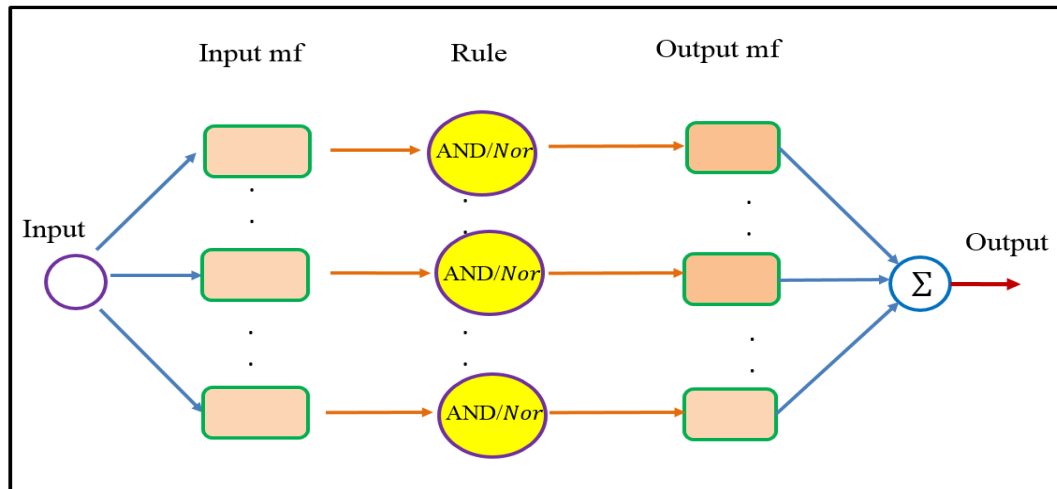
Figure 3.20 ANFIS control structure

The ANFIS method builds up the membership functions and rules of the training data. The actuation system provides the required input/output data pairs to create the training data. The control system uses the input/output data as the controlled displacement (or the commanded set points) and its desired displacement data, respectively. The parameters of the membership functions ("premise" and "consequent" parameters) are then updated (learning process) with this data, using algorithms such as the "back propagation algorithm" or the "hybrid algorithm".

The "back propagation algorithm" minimizes the loss function, in other words, it minimizes the errors between the desired outputs and the actual outputs of a system by means of a Gradient Descent (GD) approach to update the weights in the network. The "hybrid algorithm" is a combination of "back propagation" and Least Squares Estimation (LSE). The "back propagation" is applied first, with the "premise parameters" updated using the GD approach, and then the "consequent parameters" are recalculated by applying the LSE in layer 4.

For our study, the "crisp values" or the "desired displacements" of the actuation system range from -5 to 5 mm. This range is considered as the "interval of the desired displacements". For the fuzzy input and output variable membership functions, nine membership functions are used for the input and nine membership function are used for the output. The linguistic variables are: NBB- Negative Extra Big; NB-Negative Big; NLL- Negative Extra Large; NL-Negative Large; NM- Negative Medium; NS- Negative Small; Z- Zero; PS- Positve Small; PM- Positive Medium; PL- Positive Large; PLL- Positive Extra Large; PB-Positive Big; PBB-Positive Extra Big.

Two kinds of ANFIS controller were determined by using one of two popular input membership function shapes: trapezoidal and bell-shaped, with two different output membership function types: constant and linear. The rule description for both controllers is listed in Table 3-5. The two controllers have the same training data set, which has displacements ranging from -5 to 5 mm.

Table 3.5 Rules description

Rule	Description
1	*If the error is NLL then output is NBB*
2	*If the error is NL then output is NB*
3	*If the error is NM then output is NM*
4	*If the error is NS then output is NS*
5	*If the error is Z then output is Z*
6	*If the error is PS then output is PS*
7	*If the error is PM then output is PM*
8	*If the error is PL then output is PB*
9	*If the error is PLL then the output is PBB*

3.4.4   First Controller Description

This controller makes use of the trapezoidal-shaped input membership function. This membership function is used in Layer 1 in the form $\alpha_{A_j}(x)$, as shown in Equation 3.2. The calculation of $\alpha_{A_j}(x)$ is given by the following formula:

$$\alpha_{A_j}(x, l, m, n, o) = \begin{cases} 0, & \text{if } x \leq l_j \\ \dfrac{x - l_j}{m_j - l_j}, & \text{if } l_j \leq x \leq m_j \\ 1, & \text{if } m_j \leq x \leq n_j \\ \dfrac{o_j - x}{o_j - n_j}, & \text{if } n_j \leq x \leq o_j \\ 0, & \text{if } o_j \leq x \end{cases} = \max(\min(\dfrac{x - l_j}{m_j - l_j}, 1, \dfrac{o_j - x}{o_j - n_j}), 0) \qquad (3.6)$$

where $j = 1:p$ with p is the number of the linguistic variables, x is the crisp variable in the universe, the parameters l and o determine the bottom surface of the trapezoid, and the parameters m and n set the "shoulders" for the trapezoid.

Several methods could be used to generate the initial parameter values, one of these is the trial and error approach, in which the programmer assigns the values to every input experimentally and then adjusts it using a visualization process. This method is time consuming; therefore, the grid partition clustering method is used, as it is less time consuming, to create the values of these parameters and to generate the fuzzy rules. This method uses a "grid structure" to organize space of values around predetermined patterns (Schikuta, 1996). The method takes advantage of ANFIS Editor and the *genfis1* function in MATLAB. The initial values of the parameters (calculated before training) are shown in Table 3.6. The plots of the membership function $\alpha_{A_j}(x, l, m, n, o)$ using the initial values of these parameters used in Equation 3.7 are presented in Figure 3.21.
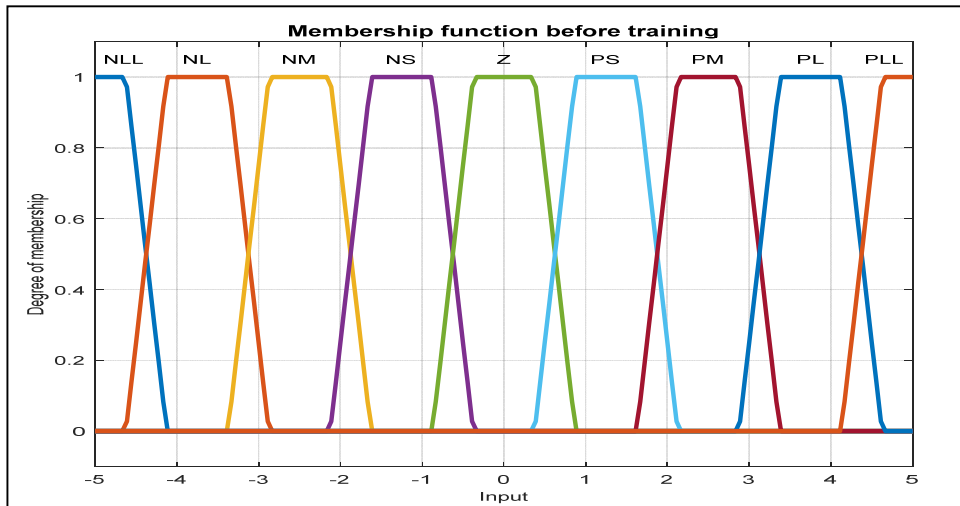
Figure 3.21 Initial input membership function plot

The training process was carried out for 600 epochs. Figure 3.22 shows the relationship of the training errors corresponding to epoch number. The training error is reduced to 0.0018 after 600 training epochs. As mentioned in the previous Section 3.4.3, in the training process, the hybrid learning algorithm – a combination of the LSE and the GD method -- is applied to identify the new values of the "premise" and the "consequent" parameters of the ANFIS controller. Each iteration or epoch is composed of a "backward pass" and a "forward pass" (Jang, 1993). The "backward pass" is where the error signals in each "node" in the 5 layers are derived. The derivative then propagates from the output towards the input. The gradient vector is saved for each training set, and the "premise parameters" are recomputed using the GD method (Jang, 1993). Table 3.6 shows all the updated "premise parameters" (after training); the plot of the membership function $\alpha_{A_j}(x, l, m, n, o)$ using the updated values of the parameters detailed in Table 3.6 is shown in Figure 3.23.
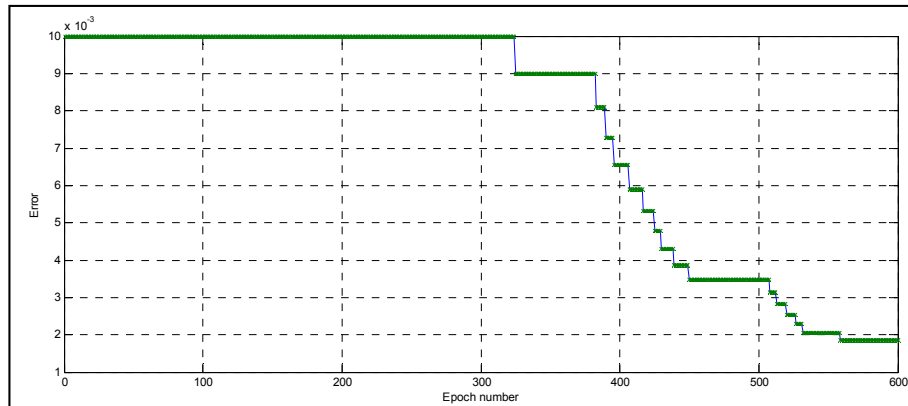
Figure 3.22 Training error versus number of epochs
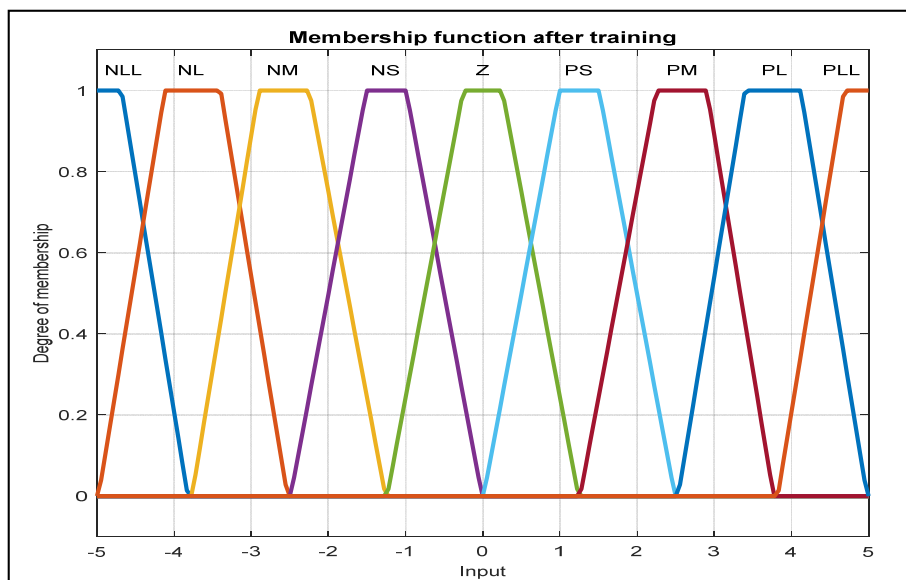
Figure 3.23 Input membership function after training

Table 3.6 Input membership function parameters before and after training

Membership function *(linguistic term)*	Before training	After training
	Parameter $[l, m, n, o]$	
NLL	[-5.875 -5.375 -4.625 -4.125]	[-5.875 -5.375 -4.68 -3.822]
NL	[-4.625 -4.125 -3.375 -2.875]	[-4.978 -4.12 -3.396 -2.531]
NM	[-3.375 -2.875 -2.125 -1.625]	[-3.768 -2.904 -2.247 -1.26]
NS	[-2.125 -1.625 -0.875 -0.375]	[-2.489 -1.507 -0.9926 -0.0104]
Z	[-0.875 -0.375 0.375 0.875]	[-1.24 -0.253 0.253 1.24]
PS	[0.375 0.875 1.625 2.125]	[0.0104 0.9926 1.507 2.489]
PM	[1.625 2.125 2.875 3.375]	[1.26 2.247 2.904 3.768]
PL	[2.875 3.375 4.125 4.625]	[2.531 3.396 4.12 4.978]
PLL	[4.125 4.625 5.375 5.875]	[3.822 4.68 5.375 5.875]

In the "forward pass", all the nodes outputs are recalculated layer by layer after including the input data into the controller. The process is reiterated for all the training datasets. The error for each pair of input/output is then computed and the LSE method is used to identify the "consequent parameters". The constant output membership function type is used, thus the values of a_j in Equation 3.1 and 3.5 are null, and only the values of b_j are taken into account. Table 3.7 shows all the values of the "consequent parameters" b_j before and after their training.

To recall and summarize the whole process, Figure 3.24 shows nine rules and nine membership functions. On the right hand side of Figure 3.24, the variation of the crisp output value (obtained displacement) with a crisp input value (desired displacement) is presented. The values are matched, as expected.

Table 3.7 Ouput membership functions

Membership function *(linguistic term)*	Before training b_j	After training b_j
NBB	0	-4.999
NB	0	-3.8
NM	0	-2.5
NS	0	-1.25
Z	0	-1.088e-14
PS	0	1.25
PM	0	2.5
PB	0	3.8
PBB	0	4.999
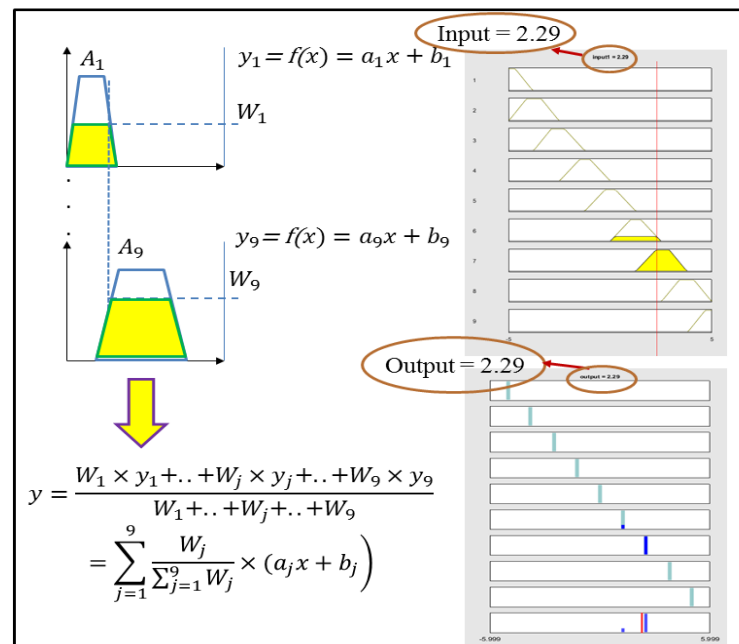
Figure 3.24 Input and output fuzzy logic reasoning

Figure 3.25 shows the bench test results of the controller when we applied it to our actuation system. The controller performed well, although there is a negligible processing time.
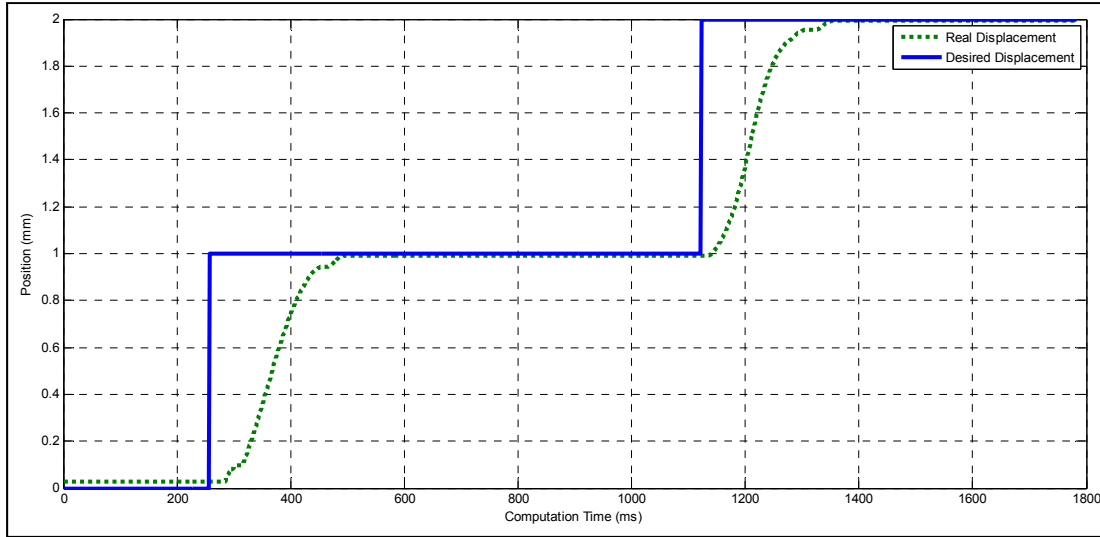
Figure 3.25 Bench test results using the 1st ANFIS controller

3.4.5 Second Controller Description

The bell-shaped input membership function is used in this controller instead of the trapezoidal one, in order to fully exploit the benefits of ANFIS methodology. The bell-shaped membership function is believed to have smoother changes and to be non-zero at all points, in contrast to the trapezoidal-shaped membership function. The formula representing the membership function is given below.

$$\alpha_{A_j}(x, t, u, v) = \frac{1}{1 + \left[\left[\left(\frac{x - v_j}{t_j}\right)^2\right]\right]^{u_j}} \tag{3.7}$$

where t, u and v are the premise parameters; t is the half width of the membership function, u determines the slopes at the points where the membership function value is 0.5, and parameter v defines the center of the curve. Figure 3.26 shows the physical meanings of the parameters:
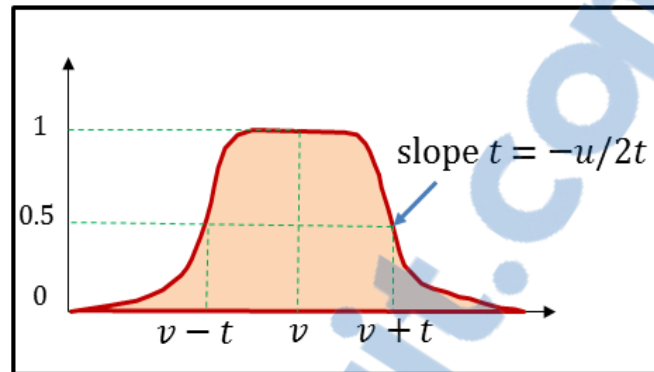
Figure 3.26 Physical meaning of bell-shaped
premise parameters.

The methods we used to determine and train the initial parameter values are similar to the methods used in the first Controller. The grid partition clustering method is used to assign the initial values, and then the hybrid algorithm is applied to find the final parameter values. Figure 3.27 presents the input membership function $\alpha_{A_j}(x, t, u, v)$ plot before and after the training process. The "premise parameters" values are shown in Table 3.8.
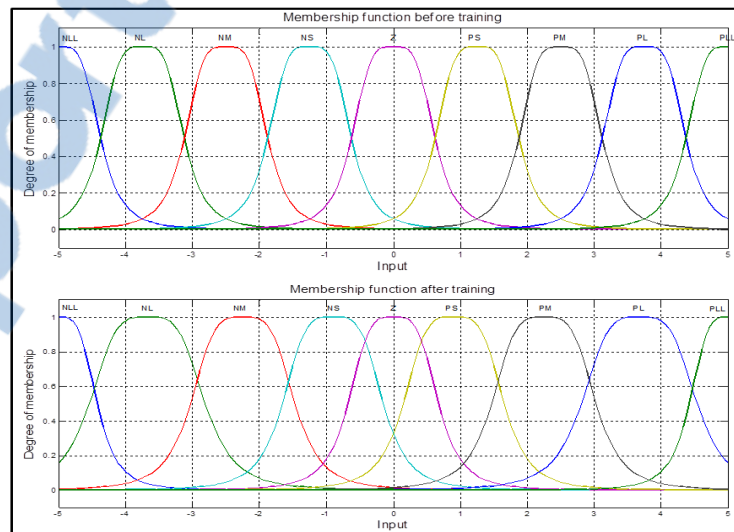
Figure 3.27 Input membership function
before and after training

Table 3.8 Membership function parameters before and after training (input)

Membership function *(linguistic term)*	Before training	After training
	Parameter $[t_j, u_j, v_j]$	
NLL	[0.625 2 -5]	[0.6019 1.999 -5.026]
NL	[0.625 2 -3.75]	[0.8662 1.969 -3.678]
NM	[0.625 2 -2.5]	[1.7816 1.987 -2.25]
NS	[0.625 2 -1.25]	[0.7547 2.009 -0.9029]
Z	[0.625 2 -1.776e-15]	[0.6781 1.958 -2.489e-10]
PS	[0.625 2 1.25]	[0.7547 2.009 0.9029]
PM	[0.625 2 2.5]	[0.7816 1.987 2.25]
PL	[0.625 2 3.75]	[0.8662 1.969 3.678]
PLL	[0.625 2 5]	[0.6019 1.999 -5.026]

Table 3.9 Membership function parameters before and after training (output)

Membership function *(linguistic term)*	Before training	After training
	Parameter $[a_j, b_j]$	
NBB	[0 0]	[0.9591 -0.2101]
NB	[0 0]	[0.9393 -0.2348]
NM	[0 0]	[0.8691 -0.3319]
NS	[0 0]	[0.6424 -0.4835]
Z	[0 0]	[0.3321 -8.347e-11]
PS	[0 0]	[0.6424 0.4835]
PM	[0 0]	[0.8691 0.3319]
PB	[0 0]	[0.9393 0.2348]
PBB	[0 0]	[0.9591 0.2101]

In this controller's design, the output membership function type is linear, which means that the output function is $y_j = \mathrm{f}(x) = a_j x + b_j$, as indicated in Equation 3.1. The values of a_j, b_j are updated using the "forward pass" of the hybrid algorithm, as described in Subsections 3.4.3 and 3.4.4.

The values of the "consequent parameters" before and after training are shown in Table 3.9. A bench test was carried out using a real time system to test the controller. Similar to the bench test applied to controller no. 1, a real-time system using a National Instrument (NI) system with the NI Veristand software was implemented with LVDT signal conditioning and other data acquisition modules (see Section 3.3 for further details). The four actuators were controlled independently. Figure 3.28 shows the outcomes of the experimental bench test for an actuator (actuator no. 1), and prove that the controller helps this actuation system to accomplish its required position securely and properly. It can be observed that controller no. 2 has a shorter response time than controller no.1.
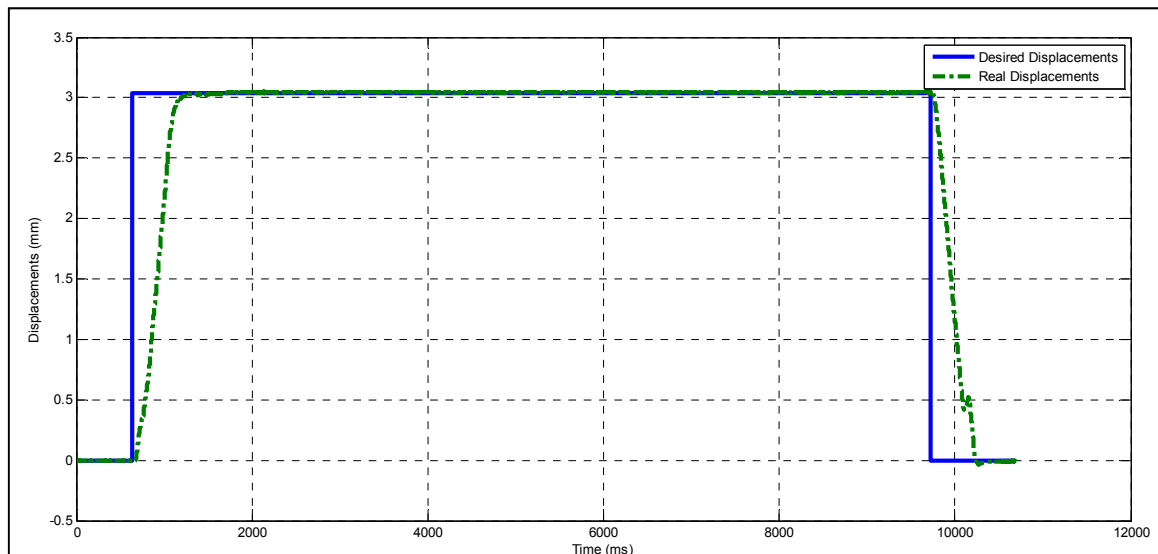
Figure 3.28 Bench test results using the 2nd ANFIS controller

CHAPTER 4

WIND TUNNEL TESTS

4.1   Description of the Wind Tunnels

A wind tunnel is an infrastructure in which scale models can be tested in a test chamber while air is passing over them in a controlled manner. Wind tunnels are mainly used for the validation of numerical calculated aerodynamic coefficients. Wind Tunnels can be open or closed. Open circuit wind tunnels get fresh air into the machine, and release the air that goes through the test section. In closed circuit wind tunnels, the air that travels through the test section is regained back into the fan, and thus passes through the test section over and over again.

Several types of wind tunnels are described in the literature, and can be grouped according to their airspeeds as follows:

- Hypersonic;
- Supersonic;
- Transonic;
- Subsonic (Low speed).

4.1.1   Price-Païdoussis Subsonic Blow Down Wind Tunnel

The Price Païdoussis Wind Tunnel located at the LARCASE is a type of open subsonic tunnel. It consists of two test chambers, illustrated in Figures 4.1, 4.2 and 4.3.

The LARCASE Wind Tunnel has 2 test sections. The maximum Mach number of 0.12 is reached in the largest test section. This test section has the dimensions of 0.6 by 0.9 meters and is made of wood with plexiglass removable doors. The volume of the second test section is half of the volume of the first test section. In this second test section, a maximum Mach

number of 0.18 can be achieved, this second test section is also made of wood and plexiglass removable doors as the first section.
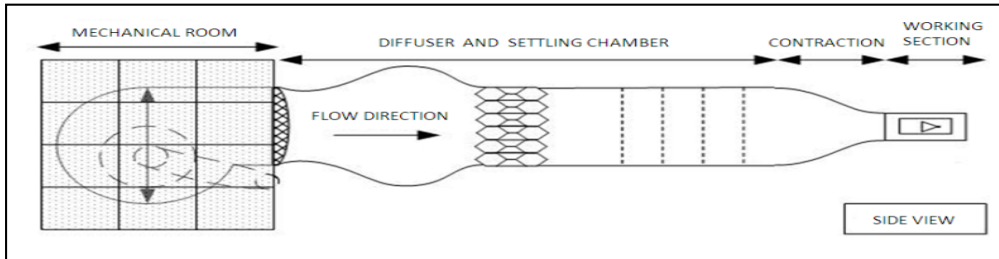
Figure 4.1 Price Païdoussis Subsonic Wind Tunnel

Figure 4.2 Working Section of Test Chamber 1

Figure 4.3 Working Section of Test Chamber 2

Table 4.1 Price Païdoussis Subsonic Wind Tunnel dimensions

Number of Test Chamber	Dimensions	Maximum speed
1	Length: 183cm; Width: 91cm; Height: 62cm	40 m/s
2	Length: 122cm; Width: 61cm; Height: 32cm	70 m/s

Tests were carried out and a calibration schedule was set up for the pressure sensor system in this Wind Tunnel. The sensor system contains 32 Kulite XCQ-0162 series sensors for pressures in the 0 to 5 psi range. The positions of the Kulite sensors and the actuators on the morphing wing are shown in Figure 4.4; the positions of the Kulite sensors on the wing are indicated in millimeters on this figure. Their exact positions are shown in Table-A II-1 in APPENDIX II.
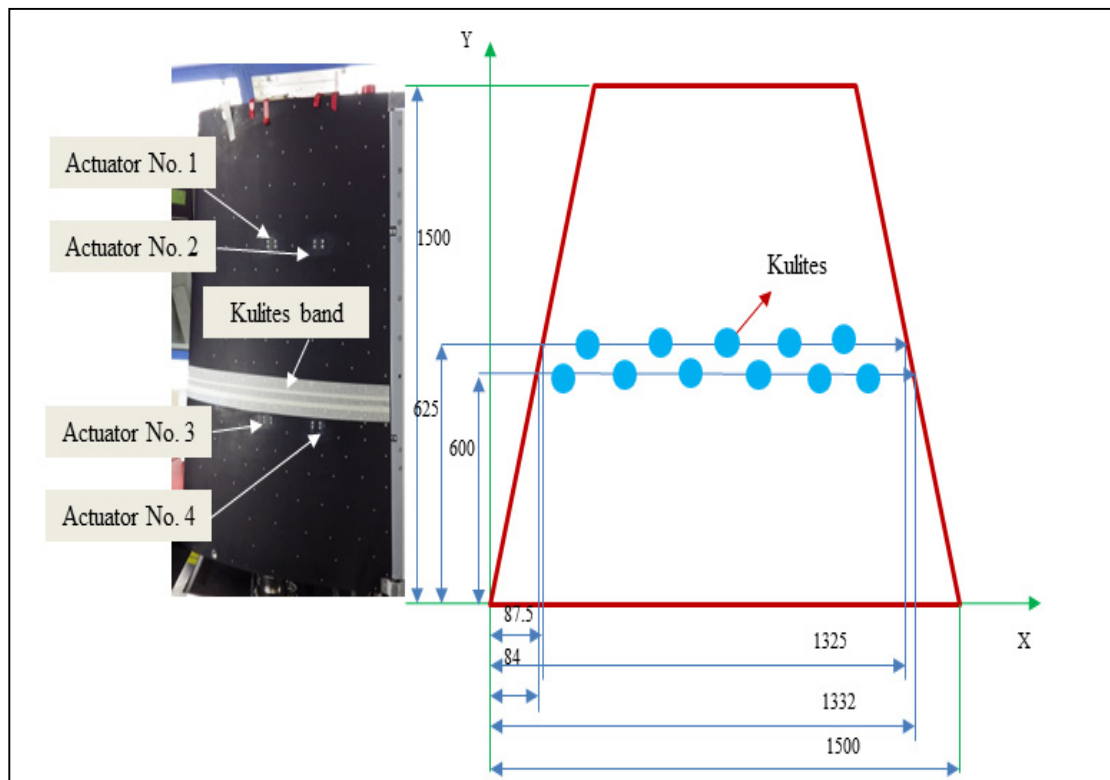
Figure 4.4 Positions of Kulite sensors on the Wing

4.1.2　Institute of Aerospace Research (IAR) - National Research Council (NRC) Wind Tunnel

The IAR-NRC Wind Tunnel in Ottawa is a closed subsonic wind tunnel. Its testing chamber is 3 meters high and 2 meters wide as shown on Figure 4.5. The standard test section area is 5.07 square meters, which is suitable to carry out aerodynamics tests for the 1.5 meters (wing span) x 1.5 meters (chord) morphing wing system. This wind tunnel's fan power is 1.5 MW, that is sufficient to reach the maximum airspeed of 140 meters/second (equal to Mach speed 0.4). A cooling system is provided to prevent its overheating. An auxiliary mechanical system is used to fix the wing in the test chamber, and moves it to the desired angles of attack.
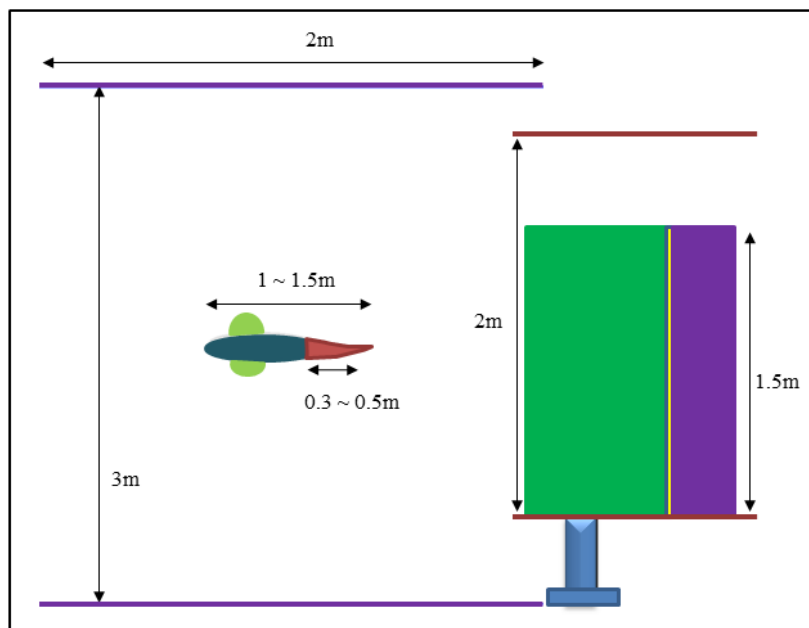
Figure 4.5 IAR-NRC wind tunnel

4.2　Test Calibration

In this section, the preparation process prior to the wind tunnel tests and the wing shape change validation are presented. This process involves the wing shape scanning techniques after these tests, and the LVDT position sensor calibration. The calibration techniques are carried out in bench tests at the LARCASE in the absence of the aerodynamic loads.

4.2.1   Wing Shape Scanning Techniques

The skin of the morphing wing is designed and manufactured of composite materials. The skin needs to be strong enough in order to sustain the aerodynamic load, as well as flexible enough so that the actuation system can change its shapes. It is also important that the shape of the skin can be recovered back to the original shape after being morphed, thus the verification of the wing skin's shape by its scanning is needed. In addition, the aerodynamic optimization process to design optimized airfoils also requires precise real skin's shape model, which should be close to its real shape as much as possible. In order to solve these problems, three 3D-tracking cameras are used to reconstruct the geometries of the morphing skin surfaces (Gabor, 2015). These cameras use circular markers, which are sticked on the skin's upper surfaces as shown in Figure 4.6, to detect the changes on the skin. The left hand side of the figure presents the setting of the scanning system is set up, while the right hand side shows the geometrical positions of the markers attached to the skin.

In order to improve the resolution of the scanned images, the aerodynamic team performs a bi-harmonic spline interpolation procedure. This procedure is carried out using the markers and interpolating between the markers; they are arranged in a 100 x 100 point grid. The scanning and interpolation procedure is repeated and applied to all flight test cases to obtain the skin displacement differences for these cases. The scanning procedure gives an estimated maximum error of 0.07 mm, which is acceptable for the aerodynamics team to carry out its numerical and simulation analysis (Gabor, 2015).
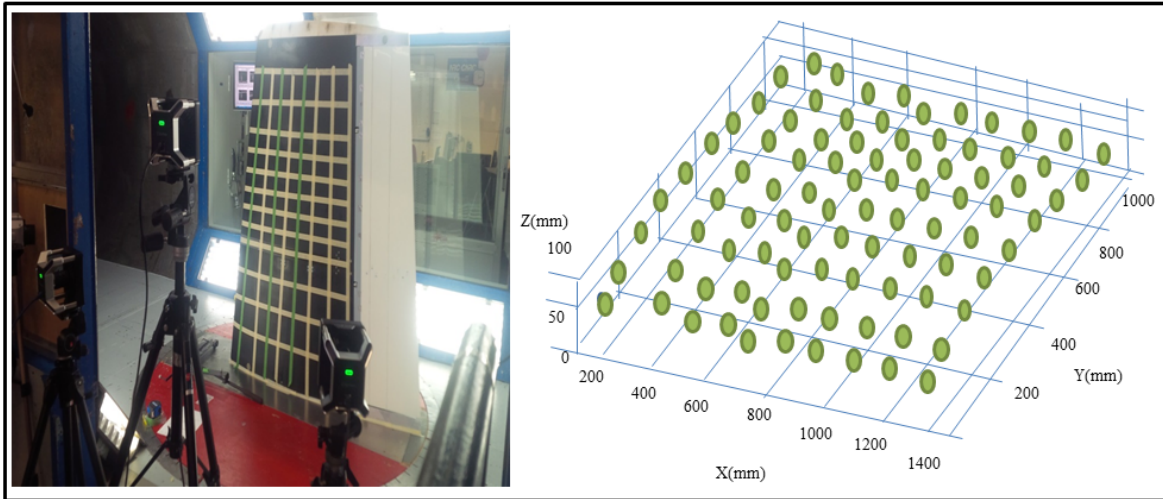
Figure 4.6 3-D wing skin scanning

4.2.2 "Play Zone" Calibration

Another problem in the morphing wing tip system that we have to cope with is the nonlinear property of the composite skin. Due to the nonlinear characteristics, the displacements of the real skin are not identical to the displacements given by the LVDT sensors (to recall, the LVDT is a kind of electrical transformers, which is used to measure linear positions). The nonlinear behavior of the composite skin is also due to its structural interaction with the actuators, thereby making the relationship between the real displacements of the skin and the LVDT signal values become nonlinear. Bench tests were taken place at the LARCASE in the absence of winds to define this nonlinear relationship. Digital Indicators (DIs) were used to record the real skin displacements, as shown in Figure 4.7.

The first problem that we need to solve is related to the "play zone" or "dead zone" - a phenomenon caused by the mechanical play generated inside the actuators and the nonlinear structural interaction between the actuation system and the morphing skin. The phenomenon creates a zone where the movement of the actuators does not lead necessarily to a movement of the wing's skin. In order to solve this "play zone" problem, the reference point (or the "zero point") of the system - the middle point of the "play zone"- was calibrated to return the system of DIs and LVDTs back to the same reference point. The DIs recorded all the

displacements between 0 and ±1 mm with reference to the zero point. Then, these displacements were compared to the displacements given by LVDTs. In this way, it was possible to obtain the offset of displacements with two measurement devices (LVDTs and DIs) and adjust the values of the LVDTs with these offsets, so that the actuation system can move the "play zone" from the random positions of LVDTs (as shown in Figure 4.8 – 4.11) back to the origin point of LVDTs; in other words, the zero millimeter position of LVDTs corresponds to the zero millimeters displacement of the wing's skin.
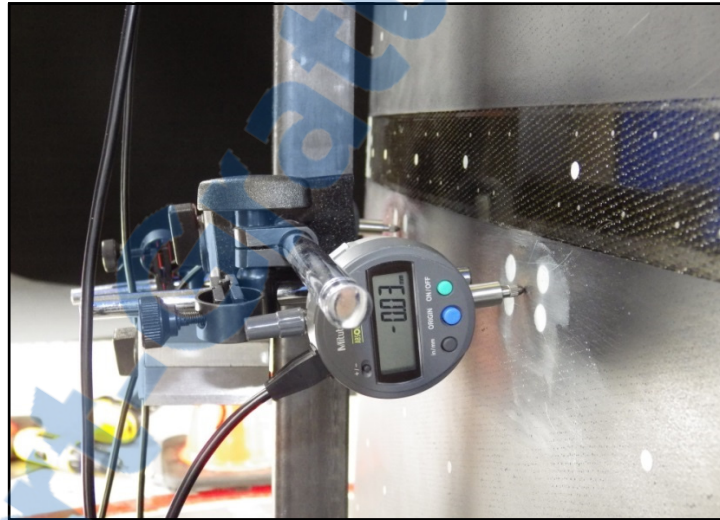
Figure 4.7 A DI attached to the wing

Figure 4.8 to Figure 4.11 shows the relationship between the real skin deplacements (DI values) and the desired skin (LVDT values) positions around the reference point in four actuators, respectively. A number of 17-21 points ranged from -1mm to +1mm to find the reference point. The list of points is shown in Table-A III-1 in APPENDIX III. The "play zone" is, as previously mentioned, the region where any movement of actuators does not lead to a movement of the wing's skin, is the highlighted values shown in Table-A III-1 (APPENDIX III). The calibrated reference point is marked by the green round shape located at the middle of the "play zone". Then, the offset values are found by calculating the horizontal distance between the original reference point (marked by red rectangular shapes) and the calibrated reference point, which is also the average value of the "play zone". The

offset values are added to all the LVDT Calculated Channels in NI Veristand Engine to update the calibrated values of LVDTs in this real time system.

Using the calculation previously mentioned with data found in Table-A III-1 and repeat the process mentioned above several times, the offsets of the four actuators are determined:

- Actuator 1 0.05 millimeter;
- Actuator 2 0.6 millimeter;
- Actuator 3 0.05 millimeter;
- Actuator 4 0.15 millimeter.
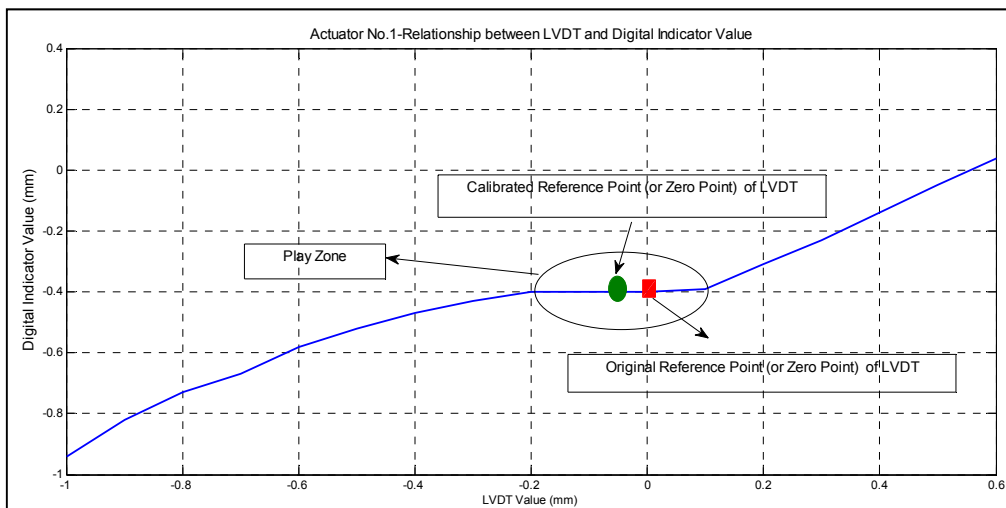
Figure 4.8 Real skin displacement versus desired displacement relationship around the reference point- Actuator No.1
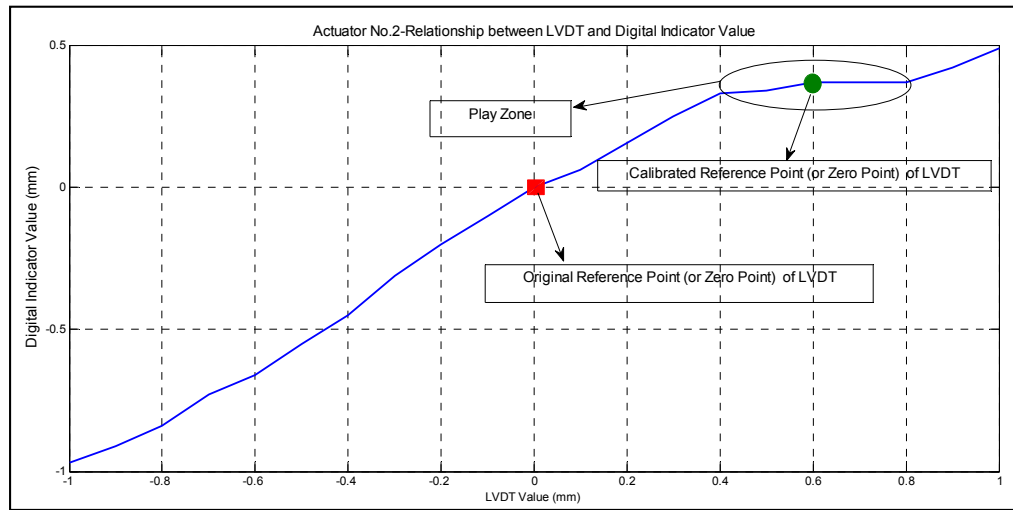
Figure 4.9 Real skin displacement versus desired displacement relationship
around the reference point- Actuator No.2
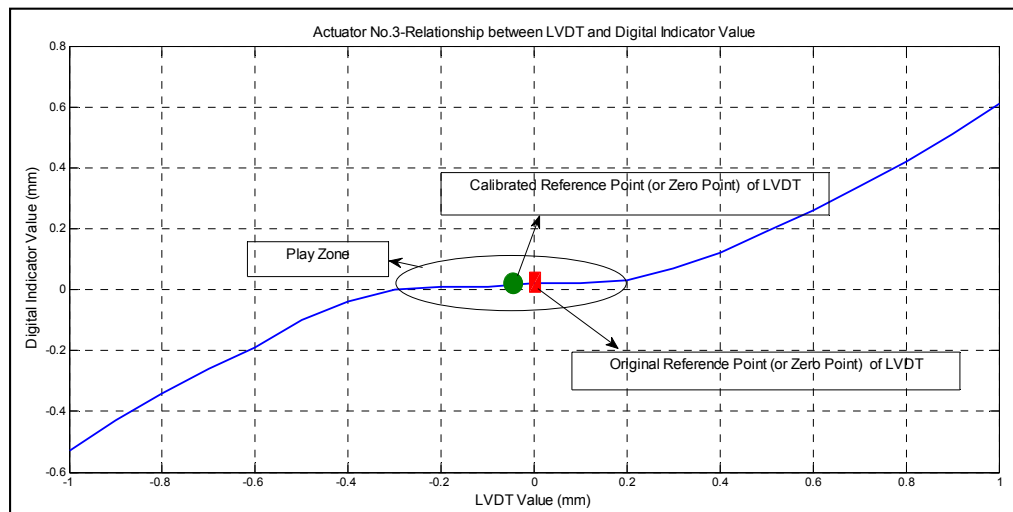
Figure 4.10 Real skin displacement versus desired displacement relationship
around the reference point- Actuator No. 3
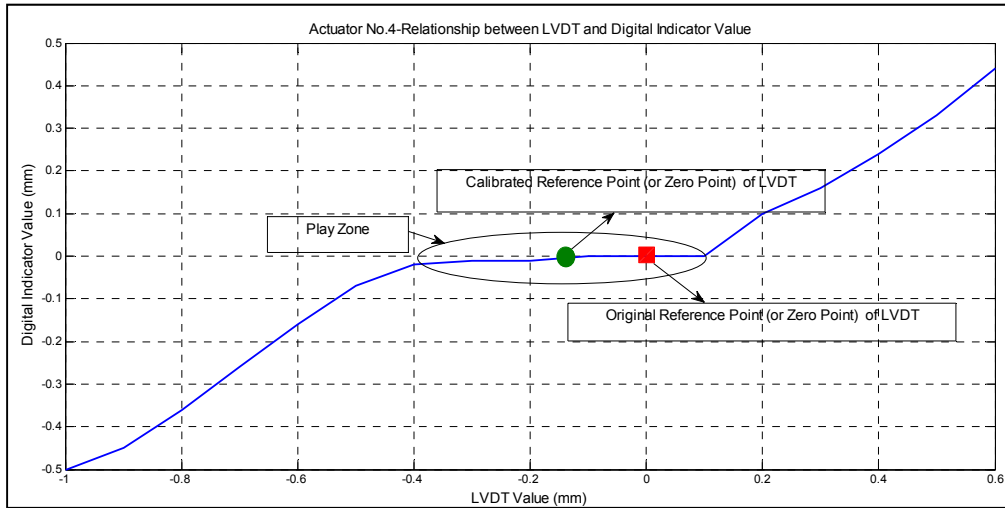
Figure 4.11 Real skin displacement versus desired displacement relationship
around the reference point- Actuator No. 4

4.2.3   LVDT/DI Calibration

The second problem is the nonlinear correspondence between the desired (or commanded) positions and the real skin displacement. In order to solve this problem, tests were run on a controller with feedback from DIs to build a Calibration Table of the relationship between the desired and the real skin displacements. At the end of the building process, the Calibration Table is supposed to include LVDT values, which should be accurate enough to achieve desired displacements on the wing-tip skin as known as "calibration"). The tests were carried out with the support of an NI custom add-on device using the NI Veristand software and a Maxon device. The feedback signal of this controller system was real skin displacements, which were acquired via DIs. The controller system is shown in Figure 4.12.
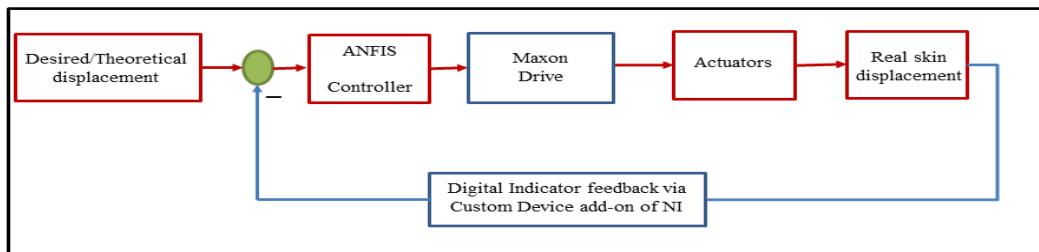
Figure 4.12 Control system with DI feedback

In order to build the Calibration Table quicker for all the flight cases, an automated calibration procedure using the NI Stimulus profile was built. The details of this procedure are described in Figure 4.13 below.
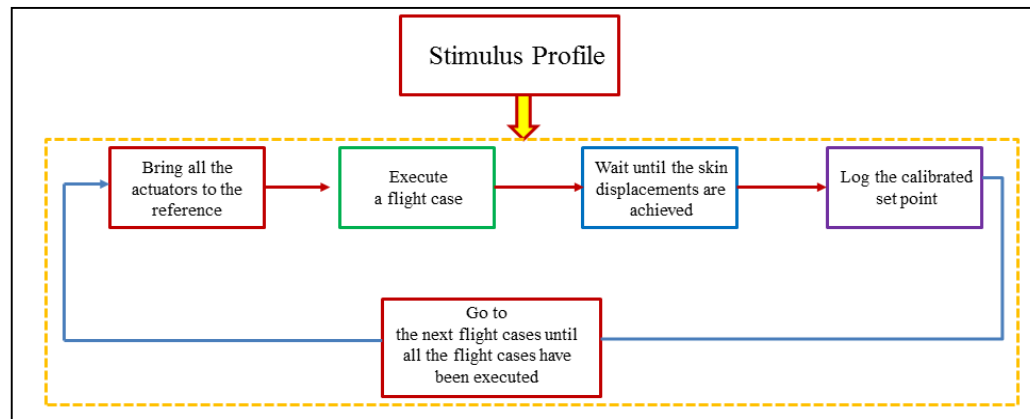
Figure 4.13 Automatic Calibration Process

The automatic calibration process can be explained as follows: For each flight case, all the actuators are brought to the calibrated reference point -- the point which was found previously. Then, the actuation system runs until the desired skin displacements are achieved. The LVDT values are logged at that moment, saved in a separate file and create the Calibration Table. The process is repeated for the next flight cases, which give various skin displacements. The definition of the flight cases is given in the next section 4.3. The calibration process ends when all the flight cases have been executed, that is equivalent to the "time" when all the airfoil shapes have been obtained by using the controller. The "log" file (or Calibration Table) with the LVDT values is used in the subsequent wind tunnel tests. In order to program the process in real time, the Stimulus Profile Editor is used; this Editor is a tool built by NI to execute desired tasks in an automated way as introduced in Chapter 3.

Four figures (Figure 4.14 to Figure 4.17) show the relationship between theoretical LVDT values and DI values or the desired skin displacements for a number of 49 cases tested in the IAR-NRC wind tunnel. "Theoretical LVDT Values" denote the displacements recorded in the Calibration Table that the actuation system needs to reach, so that the desired

displacements on the wing-tip's skin (or "Theoretical Digital Indicator Values") are achieved, and eventually, the required airfoil shapes of the flight cases are obtained. From these figures, it is observed that the difference between their values is higher with actuators no. 1, 3 and 4 than with actuator no. 2. To be more precise, any motion of the actuator no. 2 leads to the approximate same displacement of the wing-tip's skin, which is not achievable by other actuators. The explanation is most likely due to the behavior of the wing's skin around the position of actuator no. 2 and to the installation of the actuator on the skin, which linearizes the skin's behavior with respect to the motion of the actuator than to other parts of the wing.
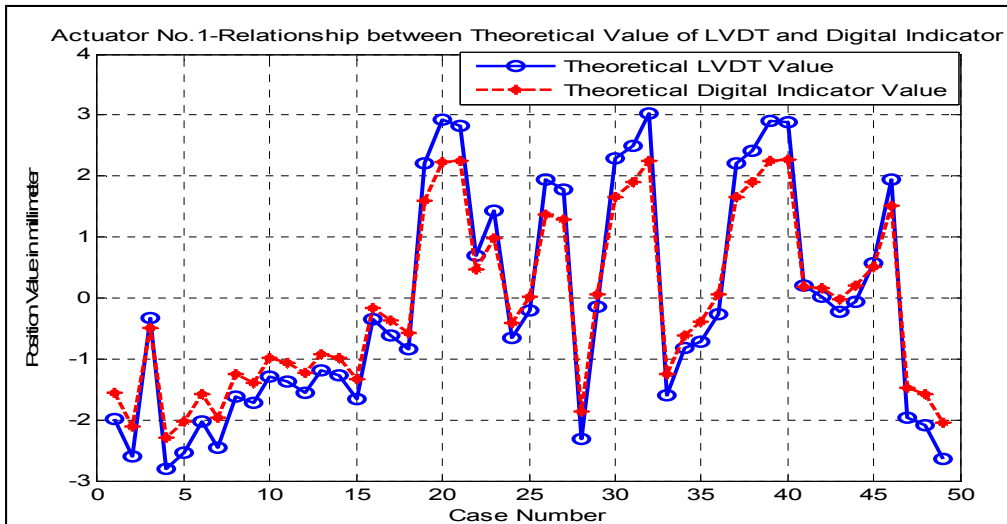
Figure 4.14 Actuator No. 1- Relationship between LVDT values
and desired skin displacements
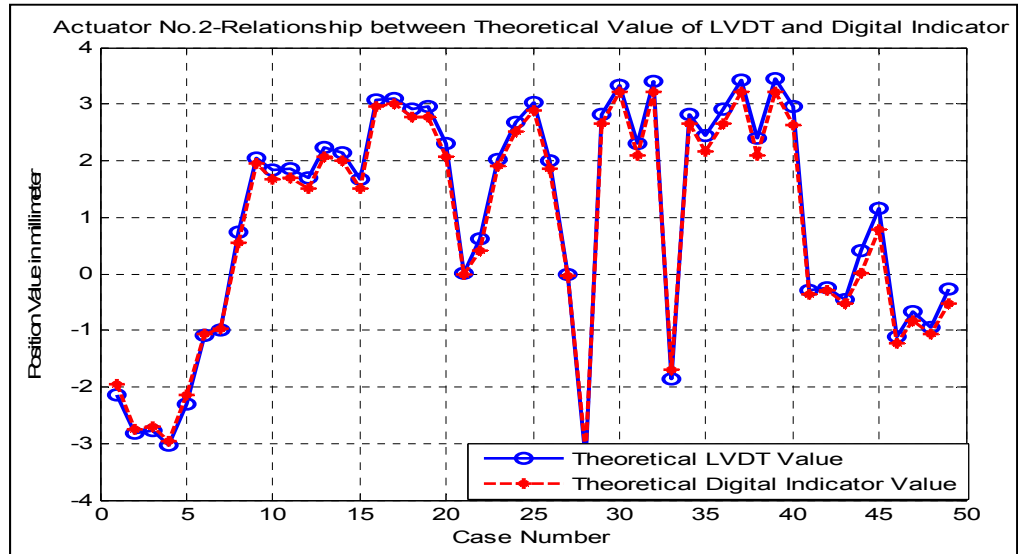
Figure 4.15 Actuator No. 2- Relationship between LVDT values
and desired skin displacements
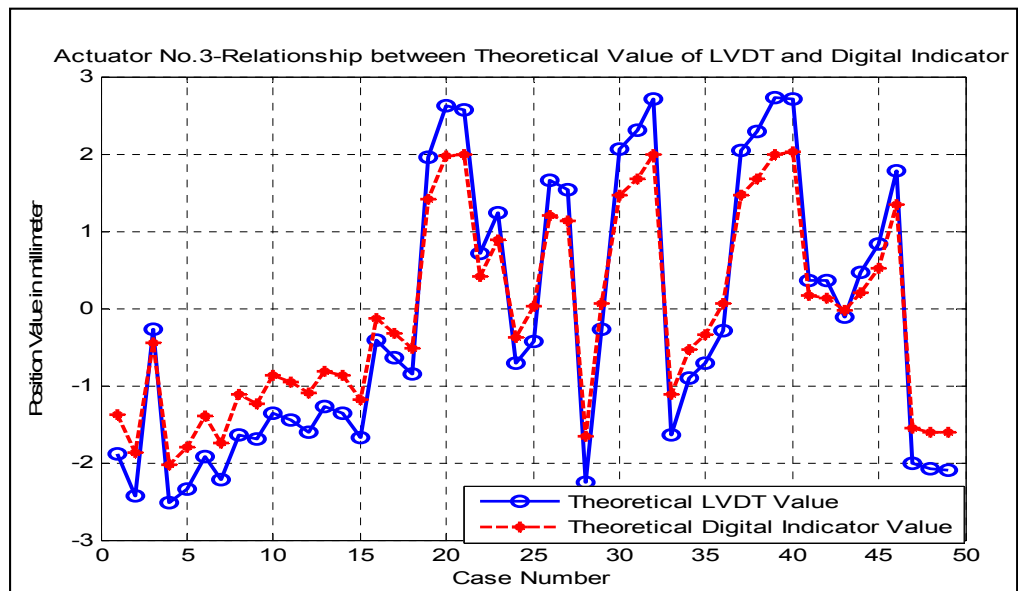
Figure 4.16 Actuator No. 3- Relationship between LVDT values
and desired skin displacements
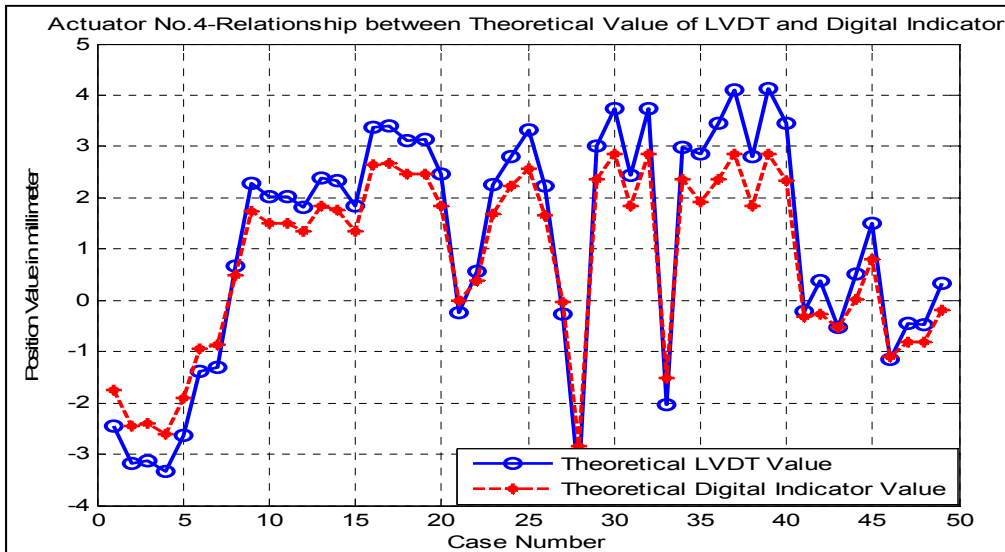
Figure 4.17 Actuator No. 4- Relationship between LVDT values
and desired skin displacements

Before the start of Wind Tunnel Test, the automated LVDT calibration process has been redone at the IAR-NRC to test its repeatability and to make sure that the Calibration Table was correct and the calibrated LVDT values used as the input of the control system were acceptable (prior to the wind tunnel tests).

Figure 4.18 shows the error distribution of four DIs attached on the upper surface of the wing-tip in a repeated automated calibration process. At this time, LVDT values created and saved in the Calibration Table were used as inputs of the closed loop control system, with position feedback from LVDT sensors, as shown in Figure 3.12 in Chapter 3. The values measured by these four DIs were recorded and compared with their theoretical values (desired displacements of the wing's skin calculated by the aerodynamics team). The error tolerance for the morphing wing-tip system is 0.1mm, and for any errors above this value, it is difficult to obtain the wing skin shapes. We can see that in Figure 4.18, the maximum error was around 0.08mm caused by Actuator No. 1, that occurred in 2 cases among 49 tested cases. In other words, the calibrated LVDT values in the Calibration Table were correct. The Calibration Table is shown in Table-A III-2 in APPENDIX III (and is presented with two decimal numbers).
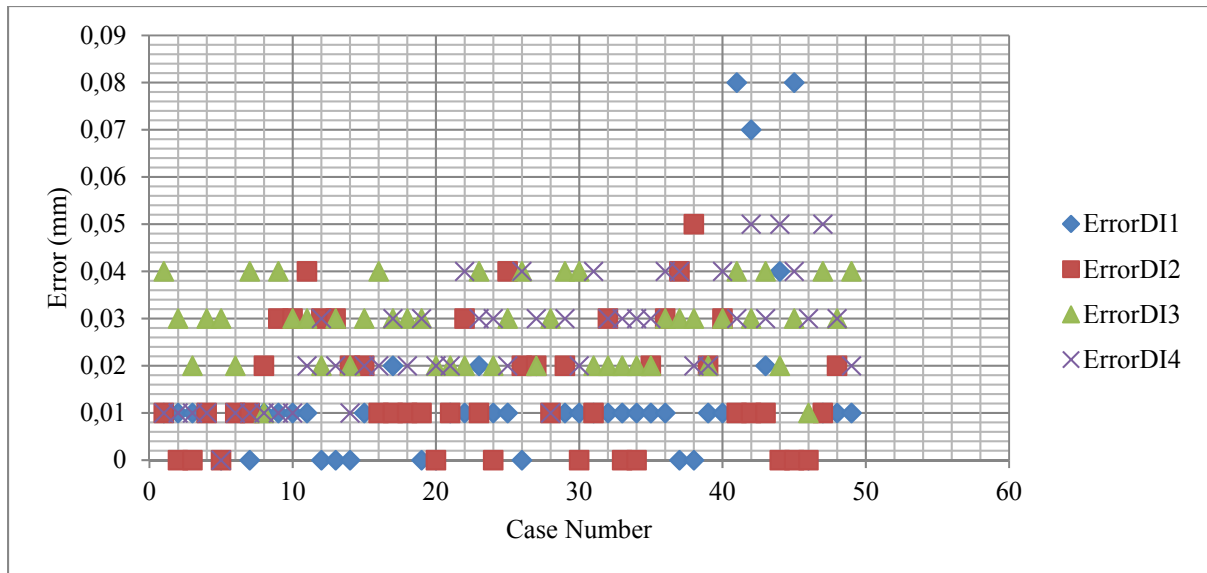
Figure 4.18 Error distribution of four DIs

4.3 Wind Tunnel Test Description

The optimized skin airfoils for different flight cases were determined theoretically by the aerodynamics team in collaboration with the structural team. The optimized airfoils were obtained experimentally in real time by the actuators motions with the aim to delay the flow transition towards their trailing edges. A flight case was defined as a combination of wind speed or Mach number (M), angle of attack (α) and aileron deflection angle (δ_{ail}). The Mach number is usually limited by the capacity (dimensions) of the wind tunnel test chamber in which the manufactured wing-tip is tested. All 49 flight cases tested in the NRC wind tunnel are shown in Table-A IV-1 in APPENDIX IV.

The Wind Tunnel Tests require the cooperation between IAR-NRC engineers and LARCASE students. IAR-NRC team implemented and installed the wing-tip on a turnable base (named TurnTable) inside the Test Section, and made sure that the wing chord line was aligned with the airflow direction in the test section. The position of the wing-tip prototype was located at the zero rotation angle of the "Turn Table", so that the desired angles of attack

were adjusted by turning the base. Figure 4.19 shows the morphing wing-tip system after its installation in the IAR-NRC Wind Tunnel.
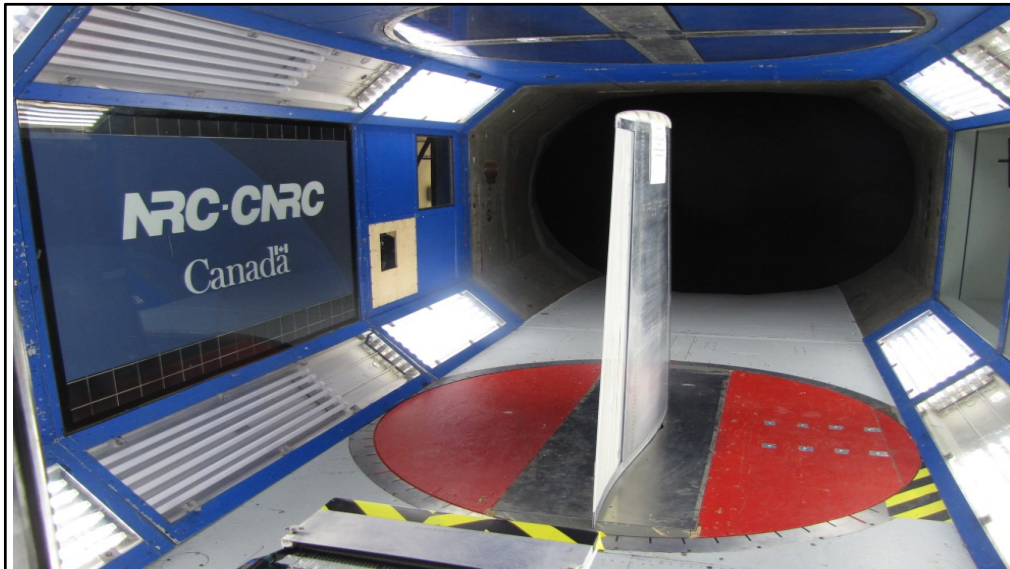
Figure 4.19 The morphing wing tip system in the IAR-NRC's Wind Tunnel

Meanwhile, the LARCASE team made the setup and reconnected all the control and data acquisition devices such as NI devices, Maxon drive, cable. and installed them in Balance Room, that is a room located under the Test Section of the Wind Tunnel with the aim to ensure the isolation from the Wind Tunnel when carrying out the Wind Tunnel Tests. The Ethernet connection was built between our PC in the Control Room and the real time NI devices and Kulite DAQ in the Balance Room, so that the motion of the actuation system on the wing-tip was controlled, and the data acquired by Kulite and LVDT sensors was collected into our PC. During the Wind Tunnel Test, for the safety requirements, several accelerometers were installed on the wing and on the aileron, and were managed by one of our LARCASE team members. These safety requirements concerned mainly the undesirable vibrations of the wing-tip. If the vibration of the wing-tip prototype recorded by the accelerometers reached an unacceptable rate, the whole Wind Tunnel Tests should be stopped (which was not the case).

A test plan was also built by the IAR-NRC, LARCASE and Italian teams (with morphing aileron). This plan included every flight case run that we wanted to carry out. Thus, the number of run cases was listed along with their aerodynamic conditions such as Mach numbers, angles of attack, deflection angles of the ailerons, and the state of morphing wing control ("morphed" or "unmorphed"). The "morphed" state was achieved with a controller, while "unmorphed" state is the original skin shape and no controller was needed. In order to synchronize the actions of all different teams in the Wind Tunnel Tests, an IAR-NRC engineer was assigned as commander-in-chief, who instructed the actions of all teams. Afterward, when the installation of all equipments and all team members were ready, the Wind Tunnel Tests were carried out in the steps listed below:

1. Shakedown: The run was carried out by the IAR-NRC team and used to check the current functional status of the Wind Tunnel system. The speed was increased gradually from 0 m/s to 51.74 m/s (Mach 0.15) and 69.98 m/s (Mach 0.20). In this run, angle of attack and aileron deflection angle is set at 0. The wing-tip skin was unmorphed.

2. Aileron Safety Runs: This step was used to check the aileron functional stability under the aerodynamic loads. The aileron was controlled to change its deflection angle from -2.5° to 6°.

3. Polar Runs: These runs aimed to check the behaviors of the wing-tip system under the airflow conditions. In these Polar Runs, the angles of attack were changed from -5° to +5° while the deflection angles of the aileron remained fixed at zero, 3° and 6°, respectively. The wing-tip skin was still unmorphed.

4. Tests using controllers: This run was the main part of the Wind Tunnel Tests. The controllers were implemented into the actuation system. The angles of attack and the aileron's deflection angles were changed, while the wing-tip skin was "morphed", then it was "unmorphed" following the specifications of the predetermined flight

cases. Mach numbers varied between 0.15 and 0.2. The aileron was controlled to move to the required deflection angle. After the ailerons had been fixed in its required position, the actuation system inside the wing-tip was set active.

Figure 4.20 shows the GUI used during the wind tunnel test, that was built with the support of NI Veristand software. The first step was to set the flight case number using the button "Flight Case Selection"; in Figure 4.20, the GUI is set for case number 19. All the information about the Mach number, angle of attack, aileron deflection angle, and the desired positions are shown according to the specific flight case. The desired positions are the positions that the actuation system needs to attain with the LVDT sensors, so that the skin can obtain the desired optimized shape. The positions were obtained in a log file, as described in the second calibration step in Section 4.2. The buttons "Activated act 1 & 3" and "Activated act 2 & 4" show that the actuators are active when they show « 1 », and that the actuators are not activated (they are "inactive") when they show « 0 ». The buttons "LVDT1", "LVDT2", "LVDT3" and "LVDT4" show predetermined or expected displacements of all four actuators from CFD calculations. In addition to the predetermined positions of the test cases, the customized cases can be built by using the buttons: "set point cust act 1", "set point cust act 2", "set point cust act 3" and "set point cust act 4" buttons. The customized cases are mostly used to double-check the actuation system to find out if all the actuators are active and well-functioning in the beginning of the Wind Tunnel Test. . The buttons "Activate act 1", "Activate act 2", "Activate act 3", "Activate act 4" and "Act_all_manual" are used to activate each actuator or all actuators simultaneously, respectively. All of the test data are saved in the control section "Log_file_motor_data" when the button "Logging Enabled" is activated.

Figure 4.20 GUI used in the Wind Tunnel Tests

Figures 4.21 and Figure 4.22 show the behavior visualization of Kulite sensors on an unmorphed and a morphed wing, respectively, in case 19. These figures demonstrate the movement of the transition region by observing the changes to the Kulite sensors. The transition region is thus delayed toward the wing's trailing edge. The peaks and the transition delay detected and measured by the Kulite sensors are explained in the next sub-section 4.4.4 by using STD/FFT method.
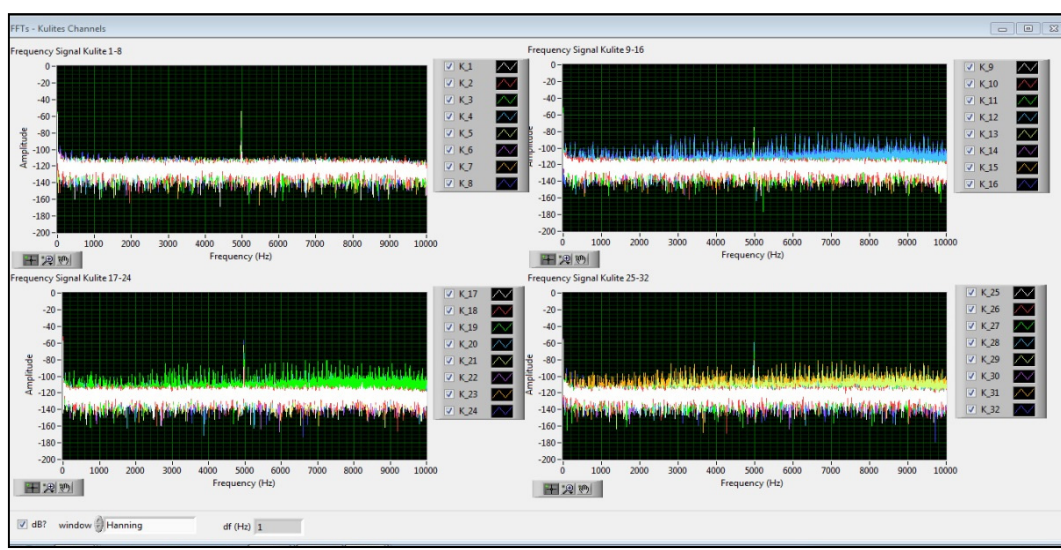
Figure 4.21 Kulite sensors' behavior on the unmorphed (original) wing
for case number 19
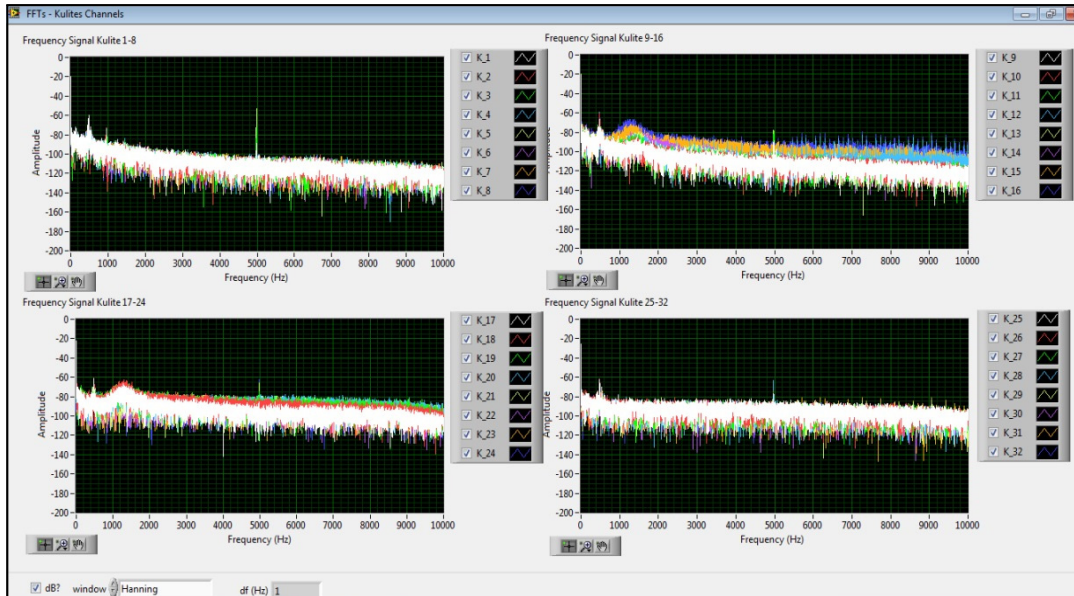
Figure 4.22 Kulite sensors' behavior on the morphed wing
for case number 19

4.4 Results obtained in the IAR-NRC Wind Tunnel Tests

In this section, the test results of two controllers under aerodynamic loads in IAR-NRC Wind Tunnel is described. As shown in Chapter 3, both controllers use ANFIS methodology. The first controller is built using the trapezoidal input membership function and the constant output membership function, while the second controller uses the bell shaped input membership function and the linear output membership function. In these tests, the theoretical LVDT values in the Calibration Table were used as the inputs of the control system. In this section, the aerodynamic results obtained and analyzed using STD/FFT and Infrared methods are presented and discussed.

4.4.1 First controller Wind Tunnel Test

The controller was used in the wind tunnel to morph the upper side of the wing in 36 flight cases, from case No. 1 to case No. 36. The test results of all four actuators in case No. 31 are shown in Figure 4.23 as an example of test results for all 36 cases. These results were obtained for the optimized shape of the flight case characterized by M= 0.2, α = -0.5, $\delta_{ail} =$

3. In Figure 4.23, "Theoretical LVDT Value" denotes the LVDT values recorded in the LVDT/DI Calibration process, while "Experimental LVDT Value" denotes the LVDT values recorded in the Wind Tunnel Test. It was observed that although there were small vibrations due to the effect of aerodynamic loads, the controller helped the actuation system to reach the desired position under aerodynamic load conditions. The performance of the Controller No. 1 in all 36 cases is shown in Figure-A V-1 in APPENDIX V. Computation time was measured by milliseconds.
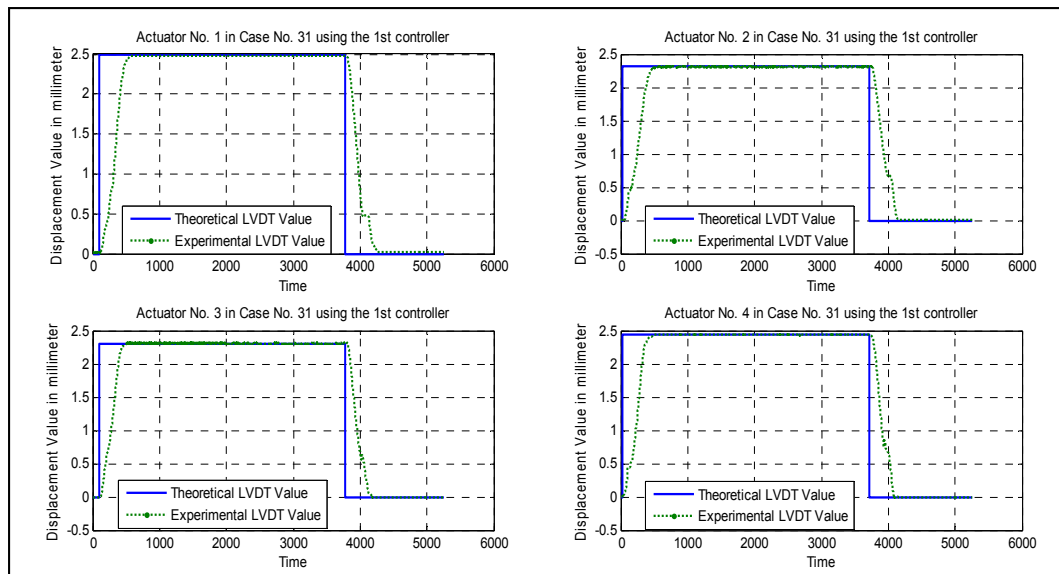
Figure 4.23 Controller No.1-Test results for case No. 31

Figure 4.24 shows the error distribution between the "Theoretical LVDT Value" and "Experimental LVDT Value" in these 36 cases. The maximum error was about 0.041 mm and was obtained for actuator no.4 in the flight case no. 2. However, most of the errors were lower than 0.02, which demonstrated that the controller achieved the desired skin displacements in all cases.
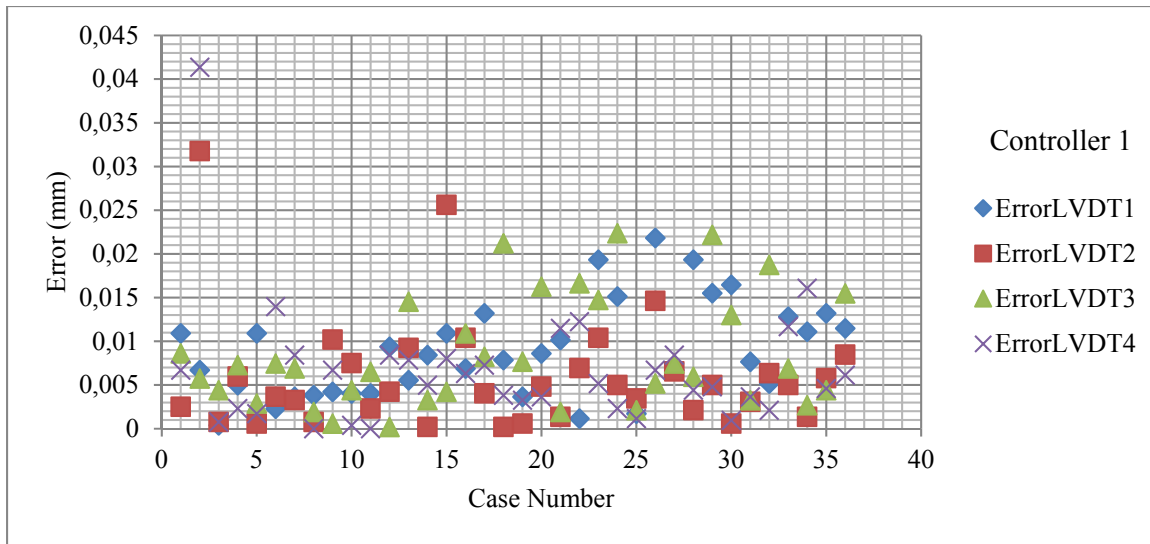
Figure 4.24 Errors distribution between the theoretical and
experimental LVDT values using Controller No. 1.

4.4.2   Second controller Wind Tunnel Test

The second controller was tested for 25 cases from case number 25 to case number 49. In order to guarantee the objectivity of the research, the number of the cases tested with each controller were chosen randomly. Figure 4.25 shows the performance of the controller in the actuation system. Similar to Figure 4.23, in Figure 4.25, "Theoretical LVDT Value" represents the LVDT values recorded in the LVDT/DI Calibration process, while "Experimental LVDT Value" represents the LVDT values recorded in the Wind Tunnel Tests. It is easily observed that the second controller helped the actuation system to reach the required positions, as the first controller did. The performance of the controller in all 25 test cases was shown in Figure-A V-2 in APPENDIX V.
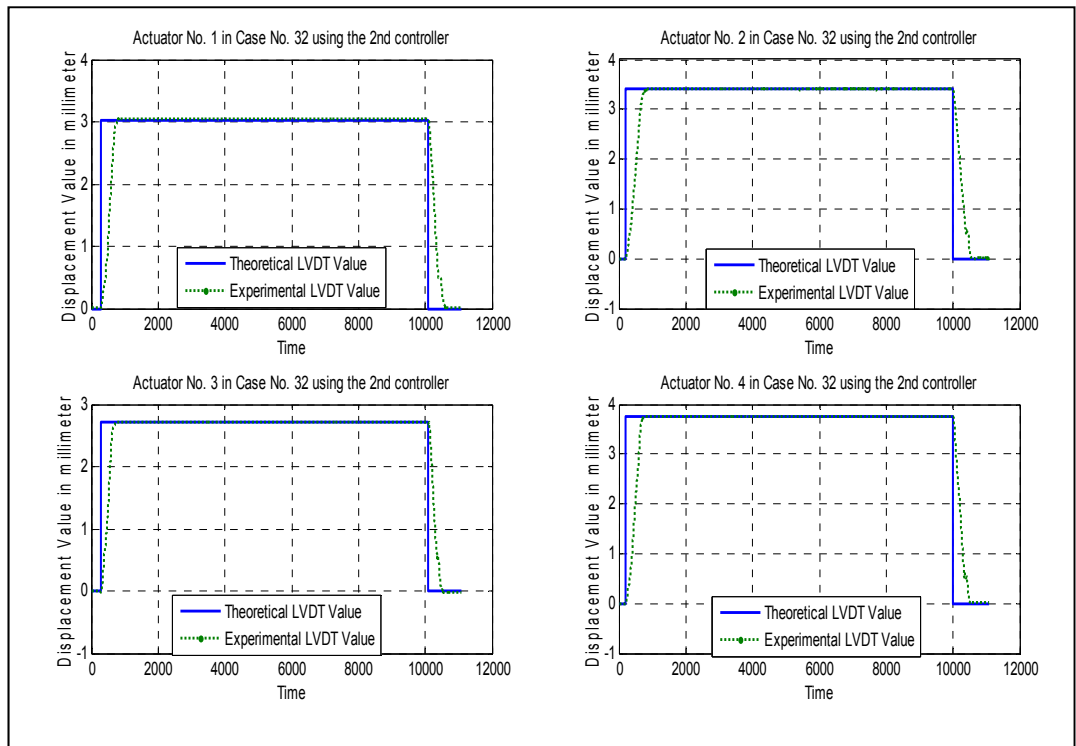
Figure 4.25 Controller No.2-Test results for case No. 32

The error distribution of the actuation system when using the Controller No. 2 is shown in Figure 4.26.
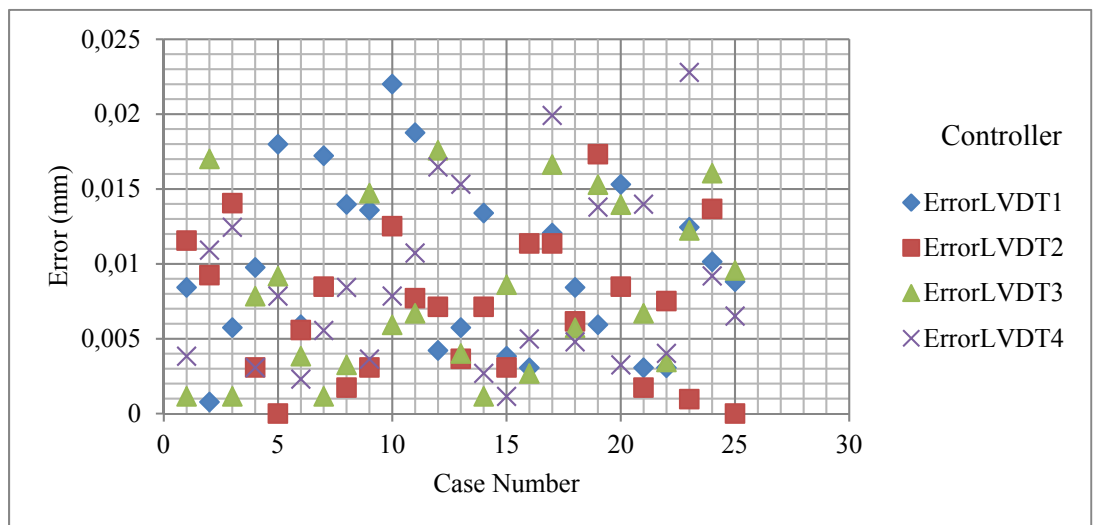
Figure 4.26 Errors distribution between the theoretical and
experimental LVDT values using Controller No. 2

In Figure 4.26, the maximum error was around 0.023 mm, and was found using the actuator no. 4, while most of errors occurred with all four actuators were lower than 0.02. The results indicate that the controller also performs well under various aerodynamic load conditions.

4.4.3 Comparison of two controllers' performance in the Wind Tunnel test and Discussion

In order to compare the results obtained by these two controllers during the Wind Tunnel Tests, one specific flight case is considered. Case no. 28 is chosen. This case is obtained for M = 0.2, α = 1, δ_{ail} = 4 . Both controllers were tested and their results are shown in Figure 4.27. These results show that both controllers can achieve the desired goals with respect to the theoretical values and that they are relatively stable. In Figure 4.27, it is easy to visualize that Controller No.2 has a faster response time than Controller No. 1. The main reason might come from the difference in membership function shapes. The Controller No.2 uses the bell-shaped membership functions, which are smoother and non-zero in all points than the trapezoidal membership functions used in the Controller No.1. Therefore, the difference in membership functions can improve the control performances of the nonlinear actuation system.

The visualization comparison between the two controllers and the theoretical values for 12 cases - cases for which both controllers were tested with all 4 actuators- is shown from Figures-A V-3 to Figure-A V-6 in APPENDIX V for these 4 actuators, respectively. These 12 common cases are the flight cases ranged from Case no. 25 to Case no. 36.
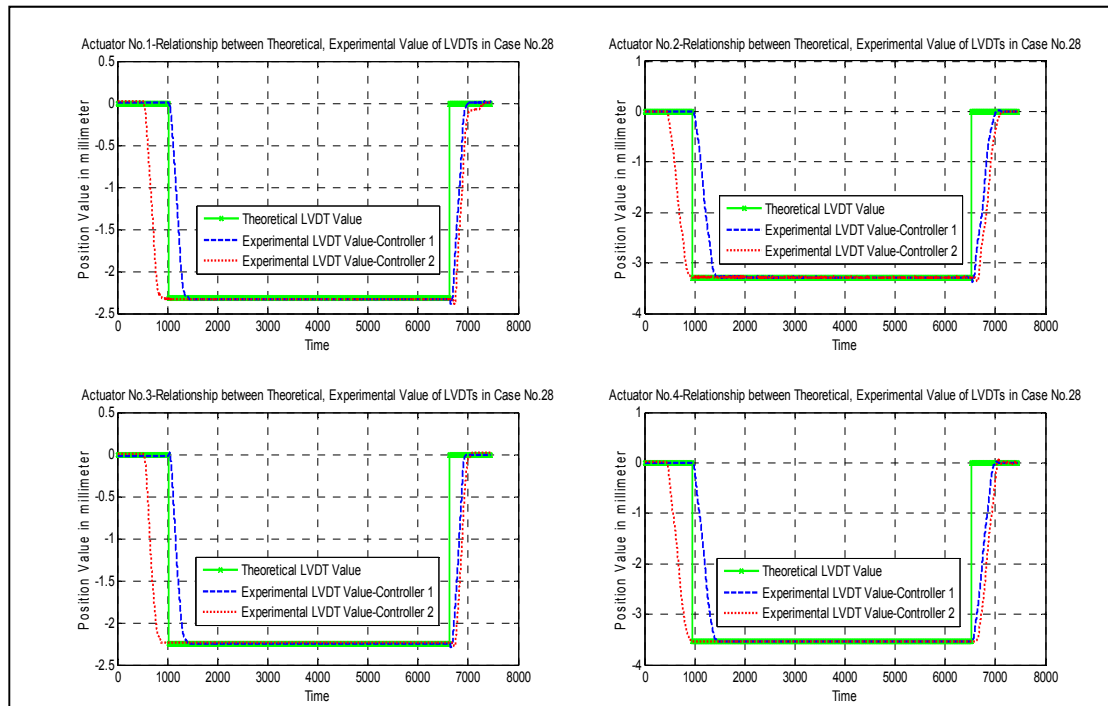
Figure 4.27 Comparison of the performance of two controllers with
theoretical values - Case No. 28, all four actuators

Figure 4.28 shows the error percentages of these two controllers for 12 flight cases. The 12 cases are cases that were tested with both two controllers. The error percentages were calculated for all four actuators in all 12 flight cases. As seen on Figure 4.28, Controller No. 2 gave a slightly lower error percentage than the Controller No. 1 (2% of the cases had the error greater than 0.02 mm in comparison with 4% of the cases for Controller No.1).

Another concern is the accumulated errors of LVDT and DI measurement values. In order to ensure ourselves that the actuation system works very well, the errors were calculated. The values can be calculated by the absolute sum of LVDT and DI errors. Figure 4.29 shows the results obtained with two controllers: Controller No. 1 was used in the first 36 cases (From Case No. 1 to Case No. 36), while Controller No. 2 was used in the last 25 cases (from Flight Case No. 25 to No. 49).

In Figure 4.29, « AccumulatedError1 » to « AccumulatedError4 » represent the accumulated errors obtained with Actuator No. 1 to Actuator No. 4, respectively. The maximum accumulated error occurred with Actuator No. 3 using Controller No. 1 was 0.06 mm, while

for Controller No. 2, the maximum accumulated error was around 0.09 mm with Actuator No. 1. The reason of obtaining this difference that contradict the best performance of the Controller No. 2 comes from the DI errors. The cases no. 41, 42 and 45 (they are numbered as case number « 41 », « 42 » and « 45 » in Figure 4.18, and are numbered « 17 », « 18 » and « 21 » in the Controller 2 graph in Figure 4.29, respectively) gave these highest accumulated errors (0.091 mm, 0.079 mm and 0.082 mm) and were also the cases that gave the highest DI errors (0.08 mm, 0.07 mm and 0.08 mm as shown in Figure 4.18 – Error distribution of four DIs).
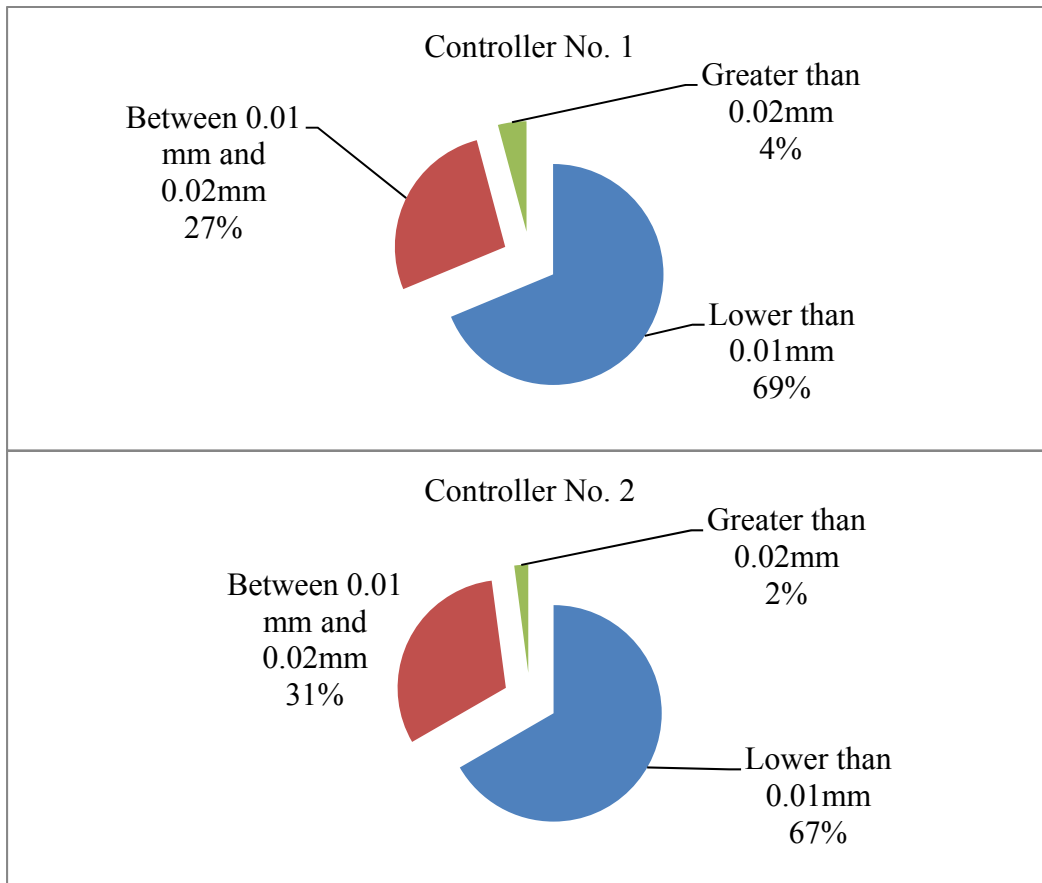
Figure 4.28 Error percentage comparison between two controllers
in 12 common cases
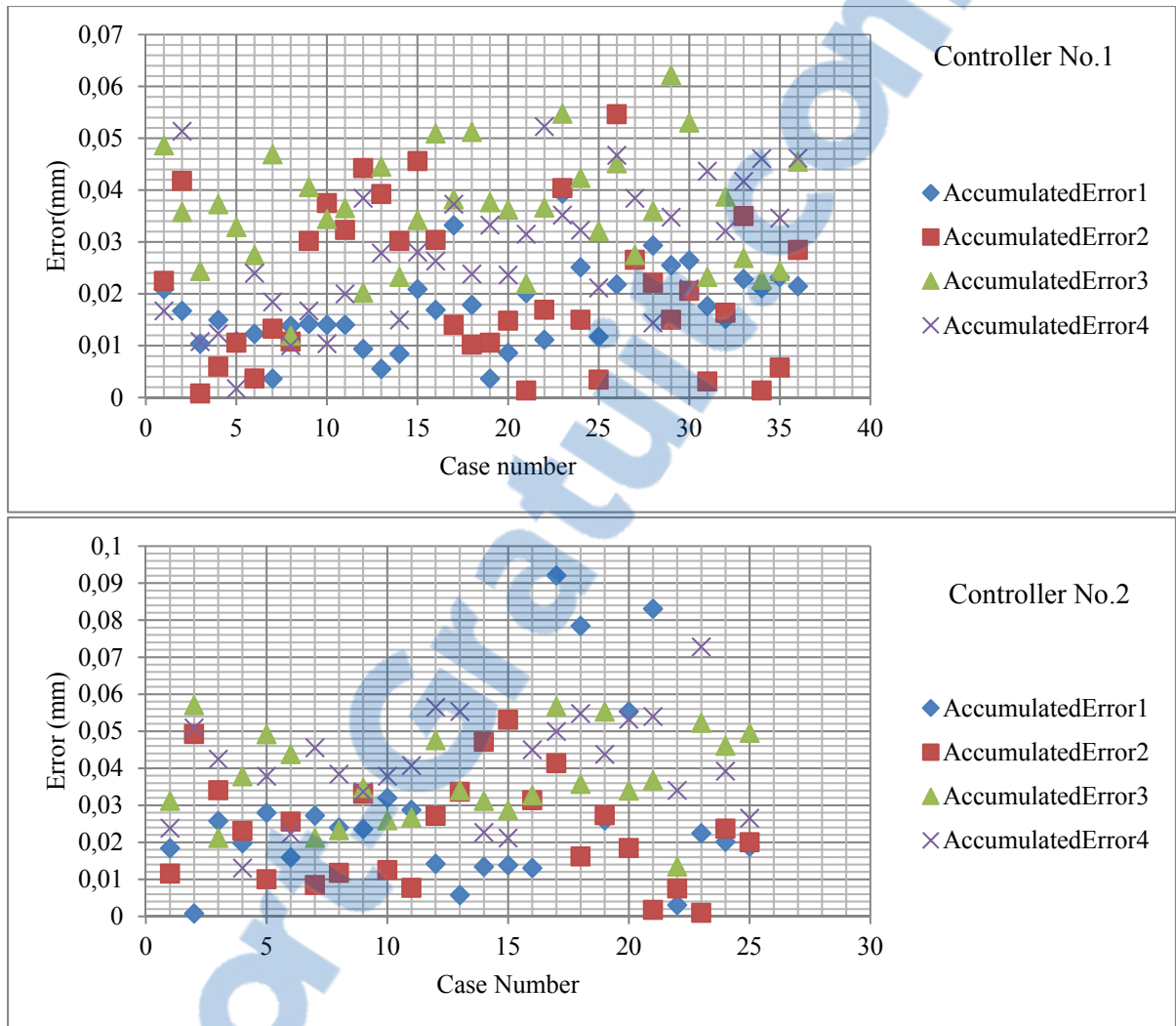
Figure 4.29 Accumulated Errors Distribution

As shown in Figure 4.29, the high accumulated errors occurred in only 3 cases, and they are still under 0.1 mm – the error threshold allowing to obtain the desired skin shapes. Most of the cases gave the accumulated errors lower than 0.06 mm for the cases using the Controller No.2, and lower than 0.05 mm for the cases using the Controller No.1. The Actuator No.1 seems to be the most efficient actuator among these 4 actuators when its error zone lies under 0.03 mm for almost all of the time (except in the three cases no. 41, 42 and 45 due to the DI errors).

Generally speaking, despite of the slight difference in aerodynamic performance, we observe that the performance of both controllers in these cases is quite good; in other words, under the wind tunnel aerodynamic loads, these two controllers proved to be effective and useful in reaching the desired skin position without any difficulties.

4.4.4   Data Postprocessing uses the STD/FFT and Infrared methods

The purpose of the project is to optimize the airfoil and to move the transition point on the surface of the wing close to its trailing edge as a means to improve its aerodynamic performance. For different flight cases, in order to observe the transition region motion process, the Kulite sensors were used as pressure measurement sensors. The wind tunnel tests provided the Kulite sensors' data, and the STD/FFT method, as well as the Infrared method was used to verify the transition points values.

4.4.4.1   STD/FFT method

During the wind tunnel tests, we recorded waveforms from 32 Kulite sensors. The recording rate was 20 KHz for 49 flight cases with an unmorphed wing, and 20 KHz for 49 flight cases with a morphed wing. In order to visualize the Power Spectrum of every Kulite sensor, we calculated the Fast Fourier Transform (FFT) for every set of 1024 data points. The acquisition rate was set to 20kHz. Both methods have used a data package (1024 data points/package) to correlate the Standard Deviation (STD) with the Power Spectrum. To ensure that the 1024 data points package, the one selected to interpret, is representative of all the recorded points, the STD values of all the recorded data points were calculated and compared with the values saved earlier by a Mean Square Error algorithm. The STD that was closest to the average one was further chosen to be interpreted along with the Power Spectrum.

Before carrying out the STD calculations, the raw signal was filtered to erase the noises. The noises can appear because of the wind tunnel noises itself, or they could be attributed to the

aileron actuation system at the beginning of every run (as described in the section 4.3, the aileron was moved to fixed positions before the actuation system inside the wing-tip was set active, while the Kulite data acquisition system was active all the time). These noises were detected in the graphs by identifying peaks that appeared on every Kulite sensor in every case, regardless the morphing status of the wing, the angle of attack and the aileron deflection. Using this noise-detection method, the peaks were eliminated during the STD calculation and the data were high-pass filtered at 1 KHz, as shown in Figures 4.30 and 4.31. The STD calculation was carried out by applying the following equation on the filtered signals (Wikipedia, 2016):

$$\Delta P_{std} = \sqrt{\frac{1}{N}\sum_{i=1}^{N}(\Delta P_i - \Delta P)^2} \tag{4.1}$$

Adapted from (Wikipedia, 2016)

Here, ΔP_{std} is the standard deviation of the pressure on a Kulite; ΔP is the mean value of the pressures of all the recorded data points of a Kulite, determined by using a Mean Square Error algorithm. ΔP_i is the pressure of the ith data point.

Figures 4.30 and 4.31 show the STD and the power spectrum visualization in Case No. 18 for a morphed and an unmorphed wing, respectively. This Case No. 18 was characterized by M = 0.15, α = 1.25, δ_{ail} = 0. The transition region was considered to be limited by two specific Kulite sensors. The starting sensor was the one from which there were changes in power spectrum amplitude, in other words, the position where the amplitude of the Power Spectrum was greater than the amplitude of the previous Power Spectrums. In Figure 4.30, that is Kulite sensor no. 15, and in Figure 4.31, it is Kulite sensor no.11. The second Kulite sensor marks the transition point, determined by the maximum of the STD plot. In Figure 4.30, that is Kulite sensor no. 20, and in Figure 4.31, it is Kulite sensor no. 16. In summary, the transition region was moved from the region between Kulite sensor no. 11 and sensor no. 16 (around 50% of the chord) to the region between Kulite sensor no. 16 and sensor no. 20

(around 54% of the chord). By referring to the positions of Kulite sensors in Table-A II-1 in APPENDIX II, it is clear that the transition region was successfully moved from the leading edge to the trailing edge.
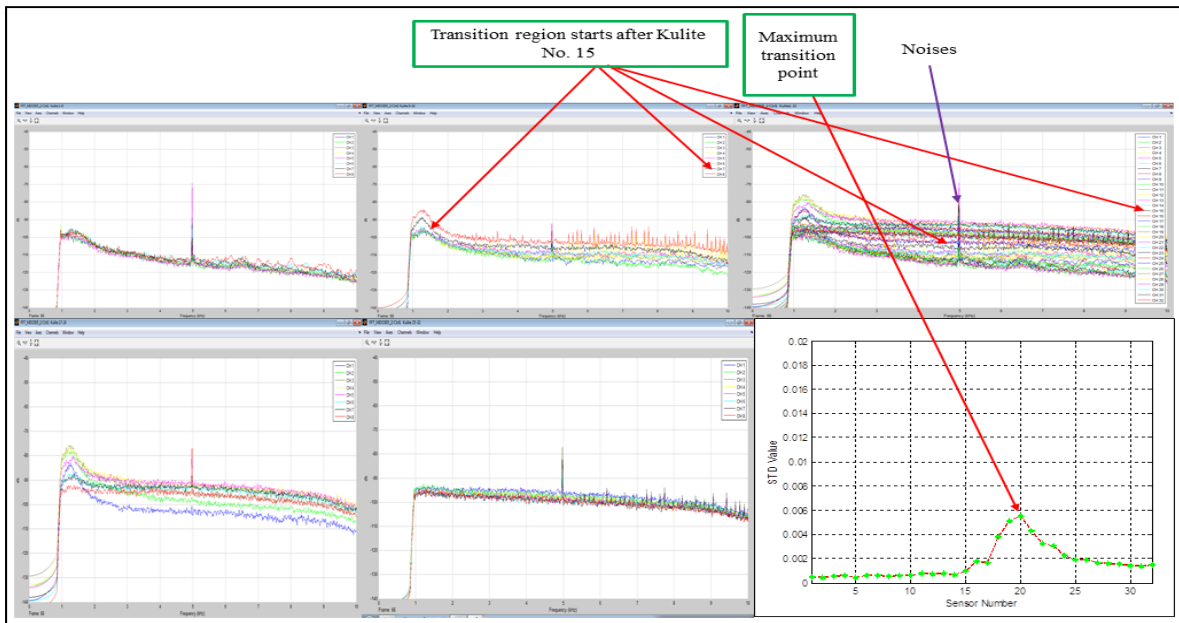
Figure 4.30 STD and Power Spectrum visualization Case No. 18- Morphed Wing.
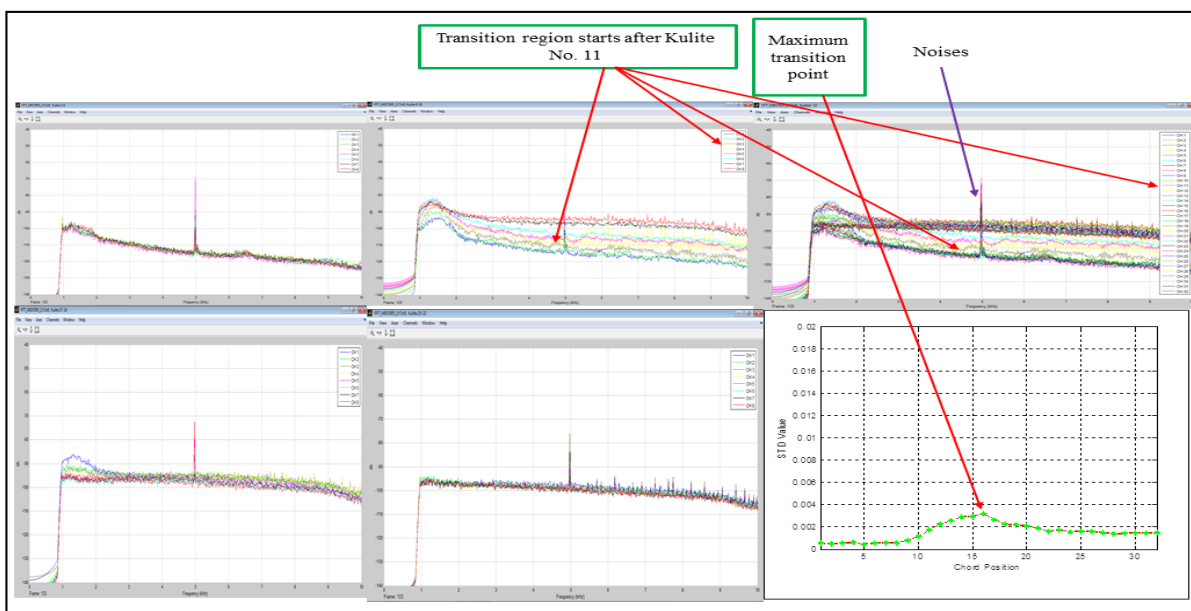
Figure 4.31 STD and Power Spectrum visualization Case No. 18- Unmorphed Wing.

4.4.4.2   Infrared Tests Method

Along with the Kulite sensors measurement method needed to capture the flow transition region, Infrared Test method was also used to validate, and to compare its results with the results obtained by the Kulite sensors. The Infrared thermography method uses the temperature changes on the surface of materials to identify the laminar-to-turbulent transition zone. For example, when the surface of the materials is heated up to a specific temperature due to the Wind Tunnel heat exchange system, there exists a difference in temperature between two flow regimes: laminar and turbulent, that is due to heat transfer coefficients, and to heat flux dissipation. By observing the changes on the images captured by a thermography camera, the flow transition zone is detected.

In this Wind Tunnel Test, a Jenoptik Variocam thermography camera was implemented. This camera has a resolution of 640 x 480 pixels and was assisted with a 60 degrees lens angle (Gabor, 2015). The camera was attached inside the test section in the subsonic Wind Tunnel and was connected to some monitors in the Control Room, which allowed the observation in real time of the transition region on the wing-tip prototype's surface. In order to increase the resolution and quality of the Infrared images, the wing-tip surface, except the Kulite sensor lines, was coated with high emissivity black paint.

Figure 4.32 shows the infrared test results for the Case No. 18. The image on the left hand side of Figure 4.31 shows the results for the unmorphed wing, and the image on the right hand side of Figure 4.32 shows the results for the morphed wing. The average flow transition line is represented by the black hard lines on the surface, while the flow transition region is determined by the two white dashed lines. The red dot located at $y/c = 0.4$ represented the transition in the span-wise direction. It can be observed that the dot was moved from $x/c = 0.5$ to $x/c = 0.52$ with the variation ± 0.01 limited by two white dashed lines. In other words, the transition region was moved from 50% $\pm$ 1% to 52% $\pm$ 1% of the chord, towards the trailing edge of the wing.
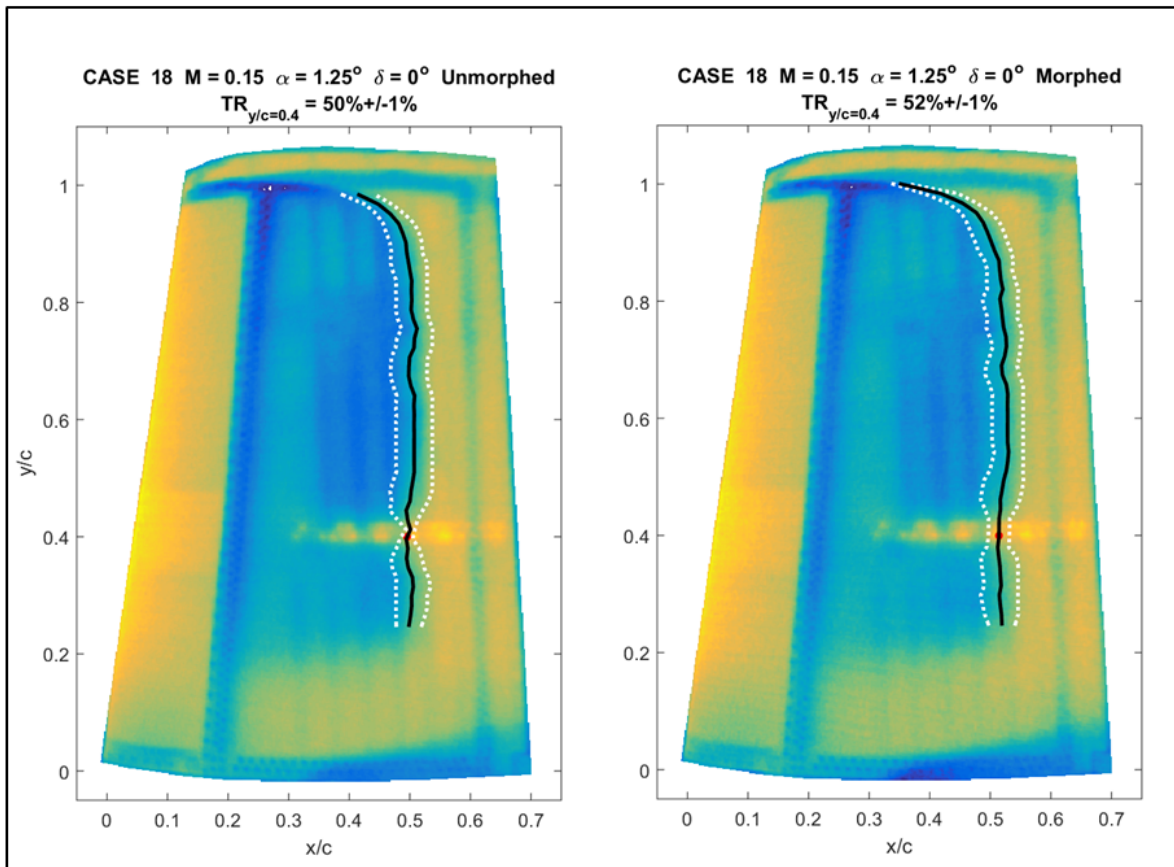
Figure 4.32 Infrared results for Case No. 18 (unmorphed and morphed)

The results in Figure 4.32 have shown that the transition of 2 % on the wing-tip was delayed from the leading edge to the trailing edge, thereby improving its aerodynamic performance.

CONCLUSION

This research presents a prototype of a morphing wing-tip model, along with its controlling methods and control system. The detailed changes of a morphing wing's upper surface that are required to morph the wing-tip of a real Bombardier aircraft is elaborated, as well as the types of the ailerons (morphing and rigid) used to reach the desired aerodynamics performance. Two ANFIS control approaches were conceived to control an actuation system using in-house developed electromechanical actuators.

These methods were validated both via simulation and experimental testing, and the results were here presented. The bench test results have shown that the controllers were able to perform well and that they remain stable.

The Price Païdoussis Wind Tunnel and IAR-NRC Wind Tunnel facilities were presented. The testing process of the morphing wing-tip system in IAR-NRC Wind Tunnel was also described in details. "Play Zone" or "Dead Zone" - the zone in which any motion of the actuation system did not lead to any change of the upper surface of the wing's skin- was identified and adjusted. A Calibration Table was also built to tackle the nonlinearity problems, which are detected between the real displacements on the skin recorded by the DIs and the desired displacements using LVDT sensors that the actuation system produced.

The Wind Tunnel test results are promising. The measured errors of DIs and LVDT sensors in 49 flight cases were identified. The small LVDT errors (below 0.02mm) show that the control system achieved the required displacements with high accuracy under the aerodynamic loads. The accumulated errors of these two error sources (DIs and LVDTs) in the experimental Wind Tunnel Tests were less than 0.1mm, which is less than the standard error predicted by the aerodynamics team. In other words, the actuation system performed very well and achieved the desired airfoil shapes.

Analyses of the STD/FFT and Infrared Test methods were also conducted. These analyses have shown that the actuation system helped to implement the movement of the transition region from the leading edge to the trailing edge of the wing prototype, thereby improving the aerodynamic performance.

As future work, the control system could be replaced by using digital signal processing systems. The use of a modern system such as the National Instrument system that was used in this work can bring stability and reliability; but it is heavy and cumbersome. The application of smaller digital signal processing systems can help to reduce the size and weight of the entire morphing control system. In addition, due to the time constraint of the project, we did not present here the modeling and simulation of the whole actuation system and the morphing wing-tip. Therefore, in the future work, a nonlinear modeling and simulation of the whole systems will be built, with the aim of developing a full automatic algorithm to control the actuation system and cope easily with the nonlinear behavior of the morphing wing's skin.

ANNEX I

MORPHING WING AND AILERON (WING-TIP) SYSTEM
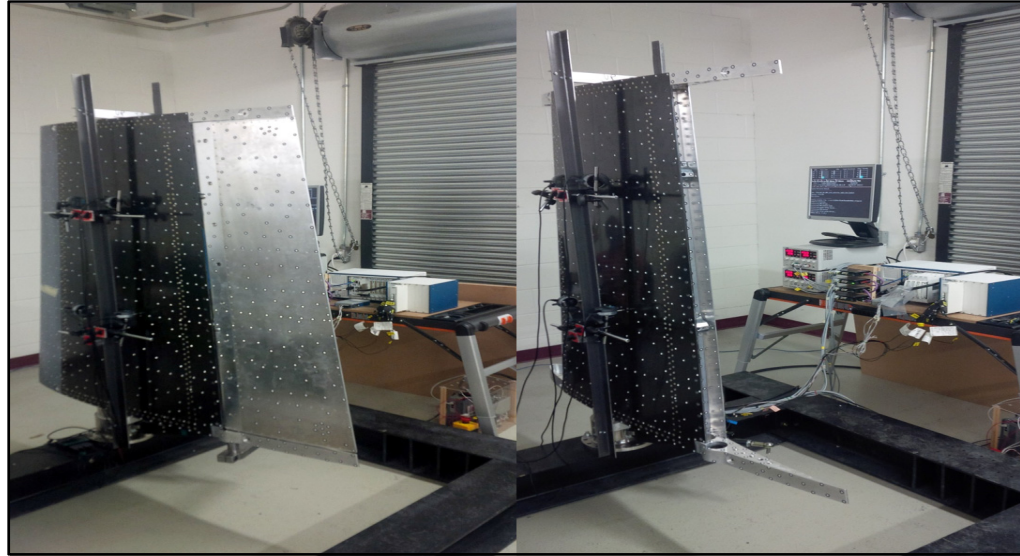
Figure A I.1. Morphing wing-tip system with and without rigid aileron

Figure A I.2. Morphing wing-tip system with morphing aileron

APPENDIX I

FLOW PHASES ON A AIRFOIL
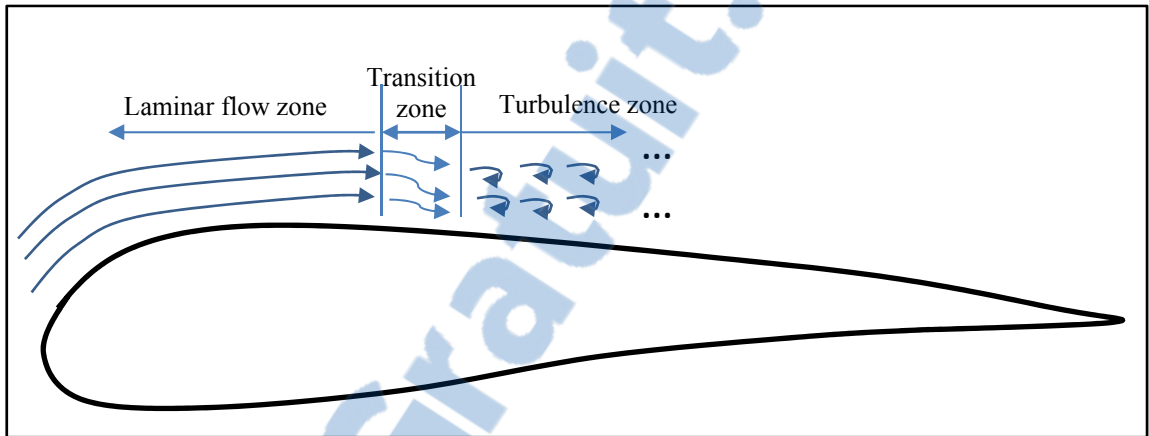
Figure-A I-1 Definition of the three phases of the flow along an airfoil

APPENDIX II

KULITE SENSORS POSITIONS

Table-A II-1 Exact positions of Kulite sensors

Kulite Number	Percentage of the chord (×100%)
1	0.285291
2	0.295467
3	0.334088
4	0.352852
5	0.363404
6	0.375373
7	0.382459
8	0.391143
9	0.413664
10	0.424537
11	0.436184
12	0.443592
13	0.451573
14	0.462824
15	0.500371
16	0.507926
17	0.512003
18	0.52698
19	0.534542

Table-A II-1 Exact positions of Kulite sensors (continued)

Kulite Number	Percentage of the chord (×100%)
20	0.546035
21	0.557063
22	0.568675
23	0.57207
24	0.587538
25	0.602104
26	0.615468
27	0.628381
28	0.638108
29	0.654659
30	0.660747
31	0.677179
32	0.683387

APPENDIX III

CALIBRATION

Table-A III-1 "Play-Zone" Calibration around the reference point

Actuator 1		Actuator 2		Actuator 3		Actuator 4	
LVDT Values	DI Values	LVDT Values	DI Values	LVDT Values	DI Values	LVDT Values	DI Values
-1	-0.94	-1	-0.97	-1	-0.53	-1	-0.5
-0.9	-0.82	-0.9	-0.91	-0.9	-0.43	-0.9	-0.45
-0.8	-0.73	-0.8	-0.84	-0.8	-0.34	-0.8	-0.36
-0.7	-0.67	-0.7	-0.73	-0.7	-0.26	-0.7	-0.26
-0.6	-0.58	-0.6	-0.66	-0.6	-0.19	-0.6	-0.16
-0.5	-0.52	-0.5	-0.55	-0.5	-0.1	-0.5	-0.07
-0.4	-0.47	-0.4	-0.45	-0.4	-0.04	-0.4	-0.02
-0.3	-0.43	-0.3	-0.31	-0.3	0	-0.3	-0.01
-0.2	-0.4	-0.2	-0.2	-0.2	0.01	-0.2	-0.01
-0.1	-0.4	-0.1	-0.1	-0.1	0.01	-0.1	0
0	-0.4	0	0	0	0.02	0	0
0.1	-0.39	0.1	0.06	0.1	0.02	0.1	0
0.2	-0.31	0.3	0.25	0.2	0.03	0.2	0.1
0.3	-0.23	0.4	0.33	0.3	0.07	0.3	0.16
0.4	-0.14	0.5	0.34	0.4	0.12	0.4	0.24
0.5	-0.05	0.6	0.37	0.5	0.19	0.5	0.33
0.6	0.04	0.7	0.37	0.6	0.26	0.6	0.44
-	-	0.8	0.37	0.7	0.34	-	-
-	-	0.9	0.42	0.8	0.42	-	-

Table-A III-1 "Play-Zone" Calibration around the reference point (continued)

Actuator 1		Actuator 2		Actuator 3		Actuator 4	
LVDT Values	DI Values	LVDT Values	DI Values	LVDT Values	DI Values	LVDT Values	DI Values
-	-	1	0.49	0.9	0.51	-	-
-	-	1.1	0.57	1	0.61	-	-

Table-A III-2 Calibration Table
(*Note*: TLVDT Values = Theoretical LVDT Values; TDI Values = Theoretical DI Values)

Flight Case No.	Actuator 1		Actuator 2		Actuator 3		Actuator 4	
	TLVDT Values	TDI Values	TLVDT Values	TDI Values	TLVDT Values	TDI Values	TLVDT Values	TDI Values
1	-1.99	-1.55	-2.13	-1.96	-1.89	-1.38	-2.44	-1.74
2	-2.60	-2.1	-2.82	-2.76	-2.42	-1.87	-3.18	-2.45
3	-0.34	-0.49	-2.77	-2.71	-0.28	-0.44	-3.12	-2.4
4	-2.81	-2.29	-3.04	-2.95	-2.52	-2.03	-3.33	-2.62
5	-2.55	-2.03	-2.31	-2.14	-2.33	-1.8	-2.64	-1.9
6	-2.02	-1.57	-1.10	-1.07	-1.93	-1.39	-1.38	-0.95
7	-2.45	-1.96	-1.00	-0.98	-2.21	-1.74	-1.30	-0.87
8	-1.63	-1.26	0.74	0.55	-1.64	-1.12	0.66	0.49
9	-1.73	-1.4	2.06	1.95	-1.70	-1.24	2.27	1.73
10	-1.28	-0.98	1.83	1.67	-1.35	-0.87	2.02	1.49
11	-1.38	-1.07	1.86	1.7	-1.44	-0.95	2.02	1.51
12	-1.56	-1.23	1.69	1.52	-1.61	-1.1	1.81	1.35
13	-1.20	-0.92	2.23	2.08	-1.27	-0.81	2.38	1.84
14	-1.27	-0.98	2.14	1.99	-1.37	-0.87	2.33	1.77
15	-1.66	-1.33	1.67	1.52	-1.68	-1.18	1.83	1.35
16	-0.36	-0.16	3.07	2.97	-0.41	-0.14	3.38	2.64
17	-0.62	-0.37	3.10	3	-0.64	-0.33	3.40	2.66
18	-0.83	-0.58	2.92	2.78	-0.85	-0.51	3.12	2.46
19	2.20	1.6	2.95	2.77	1.96	1.42	3.15	2.46
20	2.92	2.23	2.32	2.08	2.61	1.98	2.46	1.85
21	2.83	2.25	0.01	-0.01	2.57	2	-0.24	-0.01
22	0.69	0.47	0.63	0.42	0.72	0.41	0.56	0.38

Table-A III-2 Calibration Table (Continued)
(*Note*: TLVDT Values = Theoretical LVDT Values; TDI Values = Theoretical DI Values)

Flight Case No.	Actuator 1		Actuator 2		Actuator 3		Actuator 4	
	TLVDT Values	TDI Values	TLVDT Values	TDI Values	TLVDT Values	TDI Values	TLVDT Values	TDI Values
23	1.44	0.99	2.02	1.9	1.24	0.88	2.26	1.68
24	-0.65	-0.42	2.67	2.51	-0.71	-0.37	2.80	2.23
25	-0.20	0.02	3.04	2.9	-0.43	0.02	3.31	2.58
26	1.94	1.36	2.01	1.86	1.65	1.21	2.22	1.65
27	1.78	1.28	-0.01	-0.03	1.53	1.13	-0.27	-0.03
28	-2.32	-1.87	-3.28	-3.18	-2.25	-1.66	-3.53	-2.83
29	-0.15	0.07	2.83	2.66	-0.27	0.06	3.00	2.37
30	2.30	1.66	3.34	3.21	2.06	1.47	3.74	2.85
31	2.49	1.9	2.31	2.09	2.31	1.68	2.44	1.85
32	3.02	2.26	3.40	3.21	2.72	2	3.74	2.85
33	-1.60	-1.25	-1.85	-1.7	-1.64	-1.11	-2.05	-1.51
34	-0.83	-0.61	2.81	2.65	-0.90	-0.54	2.98	2.36
35	-0.71	-0.4	2.43	2.17	-0.70	-0.35	2.84	1.92
36	-0.28	0.07	2.91	2.66	-0.29	0.06	3.44	2.37
37	2.21	1.66	3.43	3.21	2.04	1.47	4.09	2.85
38	2.41	1.9	2.39	2.09	2.29	1.68	2.80	1.85
39	2.90	2.26	3.44	3.21	2.72	2	4.12	2.85
40	2.89	2.28	2.95	2.62	2.71	2.03	3.44	2.33
41	0.19	0.18	-0.29	-0.37	0.37	0.16	-0.21	-0.33
42	0.01	0.16	-0.24	-0.3	0.36	0.14	0.38	-0.26
43	-0.24	-0.03	-0.45	-0.53	-0.11	-0.03	-0.53	-0.53
44	-0.05	0.21	0.41	0.01	0.46	0.21	0.51	0.01

Table-A III-2 Calibration Table (Continued)
(*Note*: TLVDT Values = Theoretical LVDT Values; TDI Values = Theoretical DI Values)

Flight Case No	Actuator 1		Actuator 2		Actuator 3		Actuator 4	
	TLVDT Values	TDI Values	TLVDT Values	TDI Values	TLVDT Values	TDI Values	TLVDT Values	TDI Values
45	0.58	0.51	1.15	0.79	0.83	0.51	1.50	0.79
46	1.93	1.52	-1.11	-1.23	1.78	1.35	-1.16	-1.1
47	-1.97	-1.47	-0.68	-0.84	-2.01	-1.55	-0.46	-0.81
48	-2.09	-1.57	-0.95	-1.07	-2.08	-1.6	-0.47	-0.81
49	-2.63	-2.05	-0.26	-0.53	-2.09	-1.61	0.34	-0.19

APPENDIX IV

FLIGHT CASES

Table-A IV-1 Flight case specifications

Flight Case number	Angle of attack α(deg)	Mach number	Aileron angle δ_{ail} (deg)
1	-3	0.15	-2
2	-2.5	0.15	-2
3	-2	0.15	-2
4	-1.5	0.15	-2
5	-1	0.15	-2
6	-0.5	0.15	-2
7	0	0.15	-2
8	0.5	0.15	-2
9	1	0.15	-2
10	1.5	0.15	-2
11	-0.5	0.15	0
12	-0.25	0.15	0
13	0	0.15	0
14	0.25	0.15	0
15	0.5	0.15	0
16	0.75	0.15	0
17	1	0.15	0
18	1.25	0.15	0
19	1.5	0.15	0

Table-A IV-1 Flight case specifications (continued)

Flight Case number	Angle of attack α(deg)	Mach number	Aileron angle δ_{ail} (deg)
20	2	0.15	0
21	2.5	0.15	0
22	3	0.15	0
23	0	0.20	4
24	0.5	0.20	4
25	1	0.20	4
26	1.5	0.2	4
27	2	0.20	4
28	2.5	0.20	4
29	-1.4	0.20	3
30	-0.9	0.20	3
31	-0.5	0.20	3
32	0.6	0.20	2.5
33	1	0.20	2.5
34	1.6	0.20	2.5
35	-2.5	0.15	2
36	0	0.20	4
37	0.5	0.20	4
38	1	0.20	4
39	1.5	0.20	4
40	2	0.20	4
41	0	0.15	6
42	0	0.15	5
43	0	0.15	4
44	0	0.15	3

Table-A IV-1 Flight case specifications (continued)

Flight Case number	Angle of attack α(deg)	Mach number	Aileron angle δ_{ail} (deg)
45	0	0.15	2
46	0	0.15	1
47	0	0.15	0
48	0	0.15	-1
49	0	0.15	-2

APPENDIX V

CONTROLLERS' PERFORMANCE IN THE WIND TUNNEL TEST
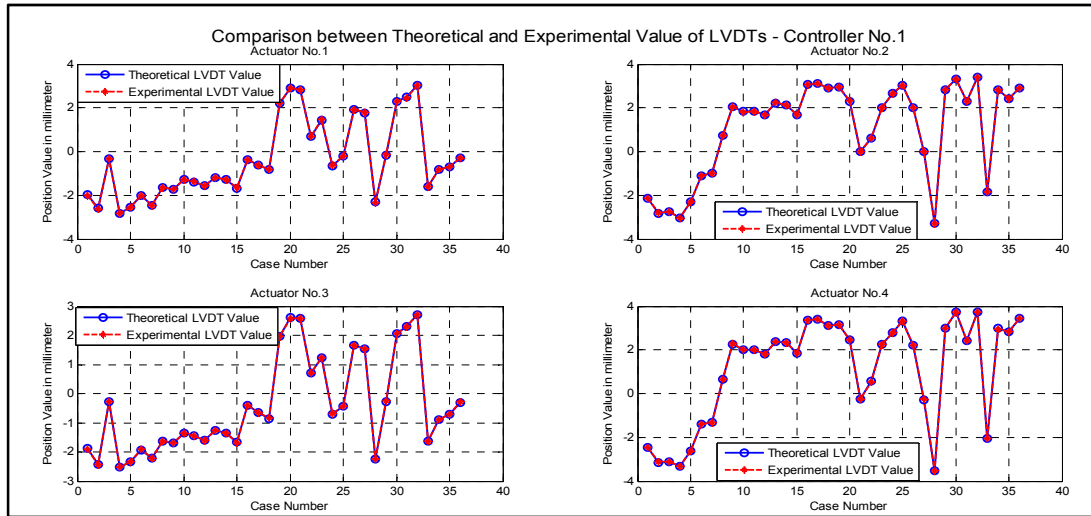
Figure-A V-1 Tests performances in 36 cases using Controller No.1
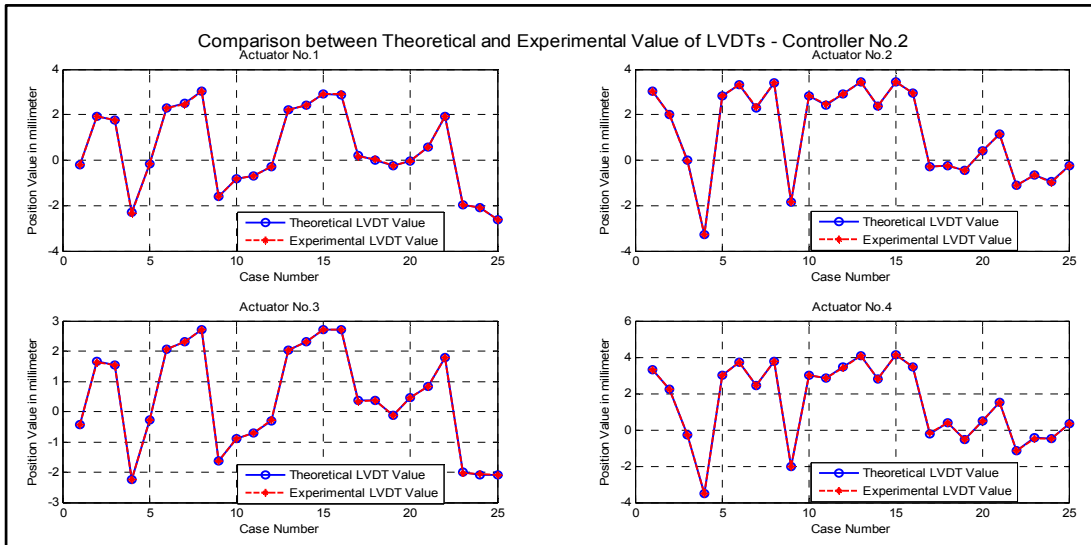
Figure-A V-2 Tests performances in 25 cases using Controller No.2
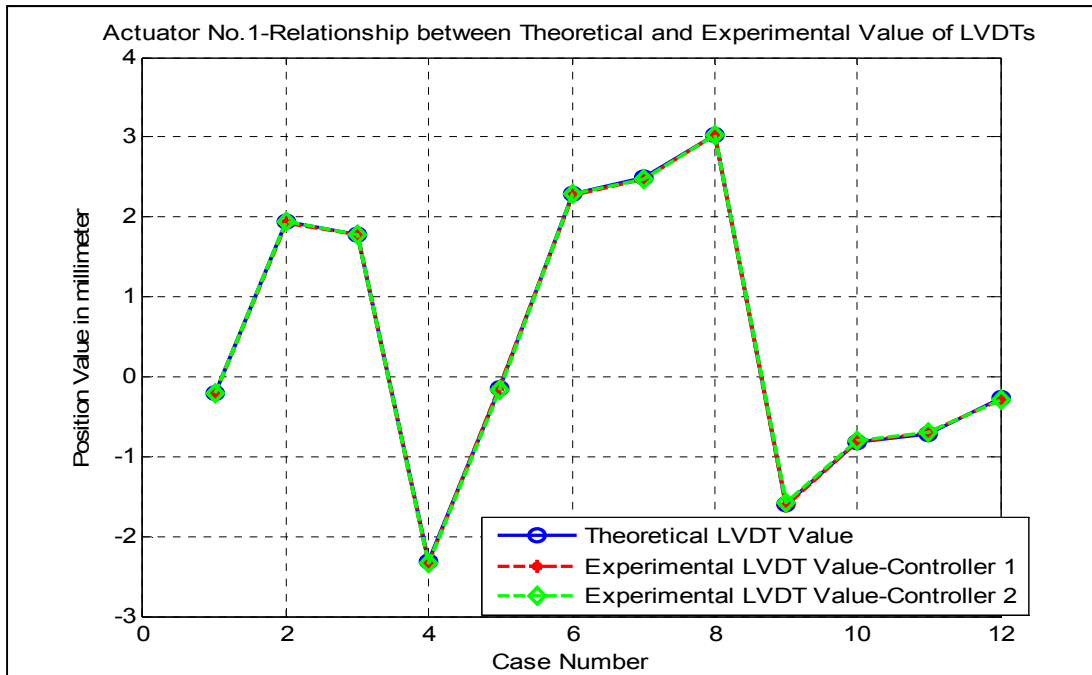
Figure-A V-3 Performance comparison of two controllers in 12 common cases
(from Case no. 25 to Case no. 36), actuator no. 1
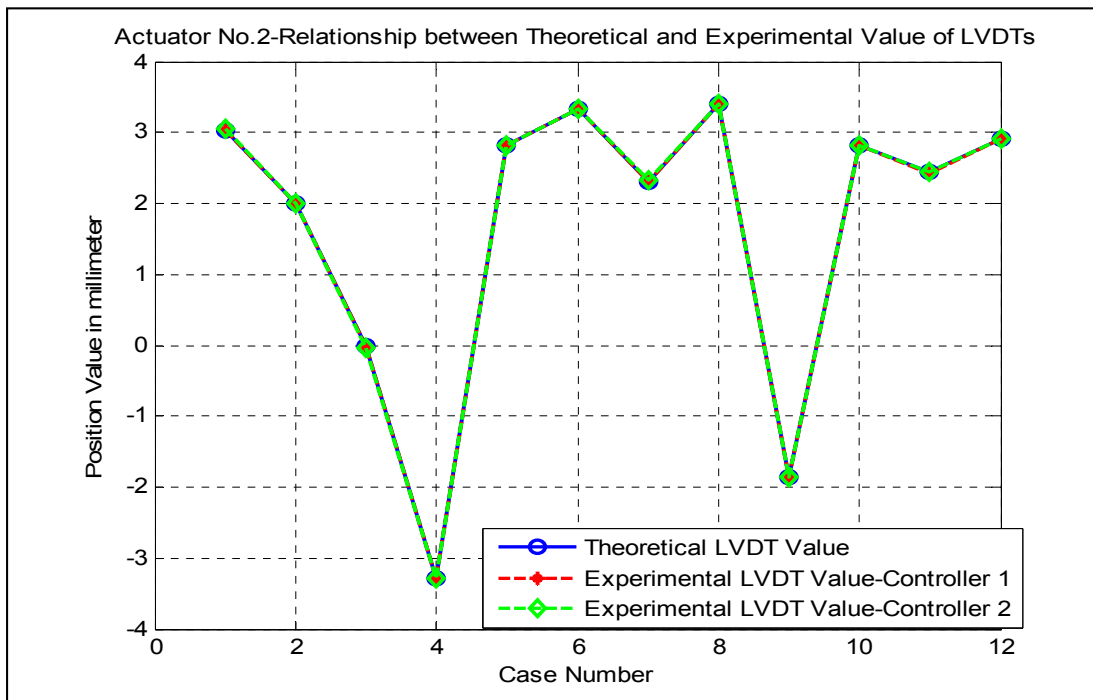
Figure-A V-4 Performance comparison of two controllers in 12 common cases
(from Case no. 25 to Case no. 36), actuator no. 2
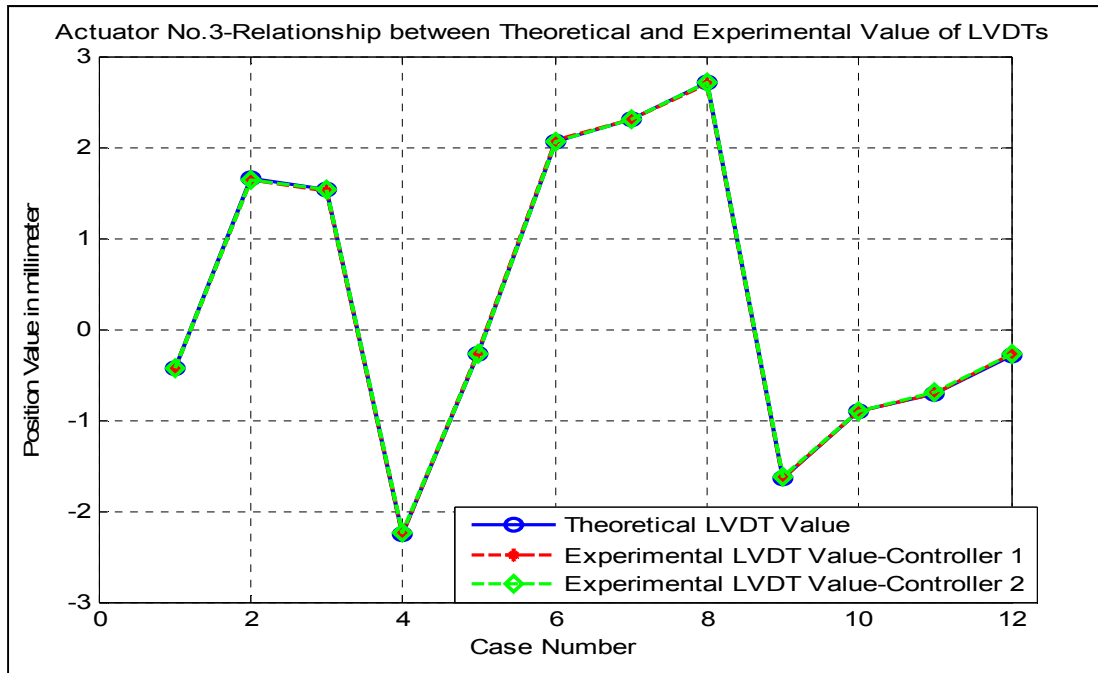
Figure-A V-5 Performance comparison of two controllers in 12 common cases
(from Case no. 25 to Case no. 36), actuator no. 3
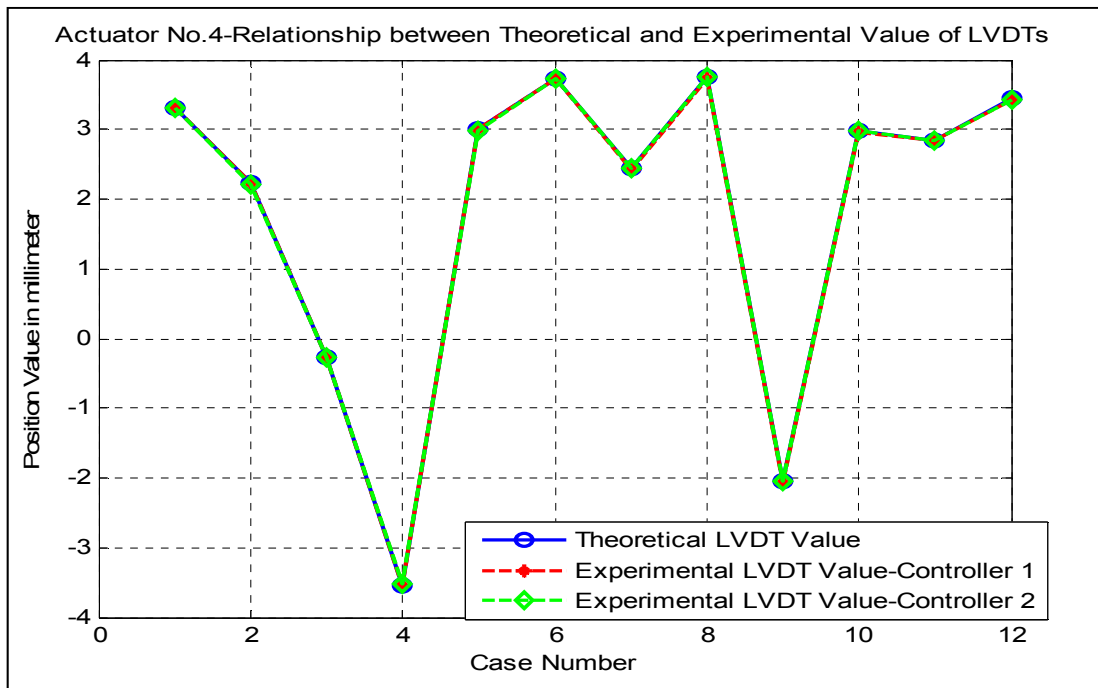
Figure-A V-6 Performance comparison of two controllers in 12 common cases
(from Case no. 25 to Case no. 36), actuator no. 4

LIST OF BIBLIOGRAPHICAL REFERENCES

Abraham, A. (2005). Adaptation of fuzzy inference system using neural learning *Fuzzy Systems Engineering* (pp. 53-83): Springer.

Anderson, S. B. (1987). A look at handling qualities of canard configurations. *Journal of Guidance, Control, and Dynamics, 10*(2), 129-138.

Barbarino, S., Bilgen, O., Ajaj, R. M., Friswell, M. I., & Inman, D. J. (2011). A review of morphing aircraft. *Journal of Intelligent Material Systems and Structures, 22*(9), 823-877.

Bilgen, O., Friswell, M., Kochersberger, K., & Inman, D. (2011). *Surface actuated variable-camber and variable-twist morphing wings using piezocomposites.* Paper presented at the 52nd AIAA/ASME/ASCE/AHS/ASC Structures, Structural Dynamics and Materials Conference

Brailovski, V., Terriault, P., Georges, T., & Coutu, D. (2010). SMA actuators for morphing wings. *Physics Procedia, 10*, 197-203.

Catalano, F., Greco Jr, P., & Martins, A. (2002). *Viscous and wave drag optimization for a transport aircraft mission adaptive wing.* Paper presented at the Aircraft Laboratory: University of São Paulo-Brazil and EMBRAER, Congress.

Cosin, R., Angelo, M., Catalano, F., & Bonemer De Salvi, F. (2010). *Mission adaptive wing optimization with Wind Tunnel hardware in the loop.* Paper presented at the 13th AIAA/ISSMO Multidisciplinary Analysis Optimization Conference.

Debiasi, M. T., Bouremel, Y., Lu, Z., & Ravichandran, V. (2013). *Deformation of the upper and lower surfaces of an airfoil by macro fiber composite actuators.* Paper presented at the 31st AIAA Applied Aerodynamics Conference.

Gabor, O. Ş. (2015). *Validation of morphing wing methodologies on an unmanned aerial system and a wind tunnel technology demostrator.* (Doctoral Degree), Ecole de Technologie Superieure.

Galantai, V. P. (2012). *Design and analysis of morphing wing for unmanned aerial vehicles.* (Doctoral Degree), University of Toronto.

Gamboa, P., Vale, J., P. Lau, F., & Suleman, A. (2009). Optimization of a morphing wing based on coupled aerodynamic and structural constraints. *AIAA Journal, 47*(9), 2087-2104.

Grigorie, T., Botez, R., & Popov, A. (2013). How the airfoil shape of a morphing wing is actuated and controlled in a smart way. *Journal of Aerospace Engineering, 28*(1), 04014043.

Grigorie, T., Popov, A., & Botez, R. (2012). *Design and experimental validation of a control system for a morphing wing.* Paper presented at the AIAA Atmospheric Flight Mechanics Conference.

Grigorie, T., Popov, A., Botez, R., Mamou, M., & Mébarki, Y. (2012a). On–off and proportional–integral controller for a morphing wing. Part 1: Actuation mechanism and control design. *Proceedings of the Institution of Mechanical Engineers, Part G: Journal of Aerospace Engineering, 226*(2), 131-145.

Grigorie, T., Popov, A., Botez, R., Mamou, M., & Mébarki, Y. (2012b). On–off and proportional–integral controller for a morphing wing. Part 2: Control validation–

numerical simulations and experimental tests. *Proceedings of the Institution of Mechanical Engineers, Part G: Journal of Aerospace Engineering, 226*(2), 146-162.

Grigorie, T. L., & Botez, R. (2009). Adaptive neuro-fuzzy inference system-based controllers for smart material actuator modelling. *Proceedings of the Institution of Mechanical Engineers, Part G: Journal of Aerospace Engineering, 223*(6), 655-668.

Grigorie, T. L., & Botez, R. M. (2010). New adaptive controller method for SMA hysteresis modelling of a morphing wing. *The Aeronautical Journal, 114*(1151), 1-13.

Grigorie, T. L., Botez, R. M., & Popov, A. V. (2009). Adaptive neuro-fuzzy controllers for an open-loop morphing wing system. *Proceedings of the Institution of Mechanical Engineers, Part G: Journal of Aerospace Engineering, 223*(7), 965-975.

Grigorie, T. L., Botez, R. M., Popov, A. V., Mamou, M., & Mébarki, Y. (2012a). A hybrid fuzzy logic proportional-integral-derivative and conventional on-off controller for morphing wing actuation using shape memory alloy Part 1: Morphing system mechanisms and controller architecture design. *The Aeronautical Journal, 116*(1179), 433-449.

Grigorie, T. L., Botez, R. M., Popov, A. V., Mamou, M., & Mébarki, Y. (2012b). A hybrid fuzzy logic proportional-integral-derivative and conventional on-off controller for morphing wing actuation using shape memory alloy part 2: Controller implementation and validation. *The Aeronautical Journal, 116*(1179), 451-465.

Guezguez, M. S. (2016). *Morphing wing system integration with wind tunnel testing.* (Master's Degree), École de technologie supérieure.

Heryawan, Y., Park, H. C., Goo, N. S., Yoon, K. J., & Byun, Y. H. (2005). *Design and demonstration of a small expandable morphing wing.*

Hetrick, J., Osborn, R., Kota, S., Flick, P., & Paul, D. (2007). *Flight testing of mission adaptive compliant wing.* Paper presented at the 48th AIAA/ASME/ASCE/AHS/ASC Structures, Structural Dynamics, and Materials Conference.

Jang, J.-S. (1993). ANFIS: adaptive-network-based fuzzy inference system. *IEEE transactions on systems, man, and cybernetics, 23*(3), 665-685.

Joo, J. J., Reich, G. W., & Westfall, J. T. (2009). Flexible skin development for morphing aircraft applications via topology optimization. *Journal of Intelligent Material Systems and Structures, 20*(16), 1969-1985.

Kang, W.-R., Kim, E.-H., Jeong, M.-S., Lee, I., & Ahn, S.-M. (2012). Morphing wing mechanism using an SMA wire actuator. *International Journal Aeronautical and Space Sciences, 13*(1), 58-63.

Kota, S., Osborn, R., Ervin, G., Maric, D., Flick, P., & Paul, D. (2009). *Mission adaptive compliant wing–design, fabrication and flight test.* Paper presented at the RTO Applied Vehicle Technology Panel (AVT) Symposium.

Kulite. (2015). Ultraminimature pressure transducer. Retrieved 2nd February, 2017, from http://www.kulite.com/technology.asp?p=2-6#technical_papers

LeBeau, R., Karam, A., Pern, N., & Jacob, J. (2010). *Analysis of low speed flow over an adaptive airfoil with oscillating camber.* Paper presented at the 48th AIAA Aerospace Sciences Meeting Including the New Horizons Forum and Aerospace Exposition.

Mashud, M., Rahman, K. M., Kaiser Ahmed, M., & Mujahidul Islam, S. (2010). *Active flow separation control using oscillating camber.* Paper presented at the 13th Asian Congress of Fluid Mechanics.

MaxonMotor. (2014). Motion control for newbies. Retrieved 10th January, 2017, from http://www.maxonmotor.com/medias/sys_master/root/8819755712542/Motion-Control-for-Newbies.pdf.

MaxonMotor. (2016). Positioning controller-Getting started. Retrieved 10th January, 2017, from http://www.maxonmotor.com/medias/sys_master/root/8821326118942/367676-Getting-Started-En.pdf

Mohdeb, N., & Hacib, T. (2014). A new application of an ANFIS for the shape optimal design of electromagnetic devices. *International Journal of Intelligent Systems and Applications, 6*(10), 11.

Munday, D., & Jacob, J. (2002). Active control of separation on a wing with oscillating camber. *Journal of Aircraft, 39*(1), 187-189.

Munday, D., Jacob, J., Hauser, T., & Huang, G. (2002). *Experimental and numerical investigation of aerodynamic flow control using oscillating adaptive surfaces.* Paper presented at the 1st Flow Control Conference.

Murray, G., Gandhi, F., & Bakis, C. (2010). Flexible matrix composite skins for one-dimensional wing morphing. *Journal of Intelligent Material Systems and Structures, 21*(17), 1771-1781.

NationalInstruments. (2015a). Components of a project. Retrieved 12th January, 2017, from http://zone.ni.com/reference/en-XX/help/372846J-01/veristand/comp_of_project/

NationalInstruments. (2015b). Getting started with NI Veristand. Retrieved 12th January, 2017, from http://www.ni.com/tutorial/14126/en/

NationalInstruments. (2015c). Understanding the Veristand engine. Retrieved 16th January, 2017, from http://zone.ni.com/reference/en-XX/help/372846J01/veristand/understanding_vs_engine/

NationalInstruments. (2016). Configure real-time testing applications. Retrieved 12th January, 2017, from http://www.ni.com/white-paper/13068/en/

Nguyen, D. H., Tchatchueng Kammegne, M. J., & Botez, R. (2015). *A predictive PID controller design for an actuator attached inside a morphing wing.* Paper presented at the 62nd CASI Aeronautics Conference and AGM 3rd GARDN Conference, Montreal, QC, Canada.

Nguyen, D. H., Tchatchueng Kammegne, M. J., Botez, R. M., & Grigorie, L. (2016). *Open loop morphing wing architecture based ANFIS controller.* Paper presented at the 16th AIAA Aviation Technology, Integration, and Operations Conference.

Nguyen, N., & Urnes, J. (2012). *Aeroelastic modeling of elastically shaped aircraft concept via wing shaping control for drag reduction.* Paper presented at the AIAA Atmospheric Flight Mechanics Conference.

Nguyen, N. T., Ting, E. B., Nguyen, D., Dao, T., & Trinh, K. (2013). *Coupled vortex-lattice flight dynamic model with aeroelastic finite-element model of flexible wing transport aircraft with variable camber continuous trailing edge flap for drag reduction.* Paper presented at the AIAA Atmospheric Flight Mechanics (AFM) Conference.

Ohanian III, O. J., Karni, E. D., Olien, C. C., Gustafson, E. A., Kochersberger, K. B., Gelhausen, P. A., & Brown, B. L. (2011). *Piezoelectric composite morphing control surfaces for unmanned aerial vehicles.*

Olympio, K. R., & Gandhi, F. (2010). Flexible skins for morphing aircraft using cellular honeycomb cores. *Journal of Intelligent Material Systems and Structures, 21*(17), 1719-1735.

Omega. (2014). Miniature LVDT displacement transducer with guided core. Retrieved 2nd February, 2017, from http://www.omega.ca/pptst_eng/LD340.html

Pern, N., & Jacob, J. (1999). *Aerodynamic flow control using shape adaptive surfaces.* Paper presented at the Proc. 1999 ASME Design Engineering Technical Conferences (Las Vegas, NV).

Popov, A. V., Botez, R. M., & Labib, M. (2008). Transition point detection from the surface pressure distribution for controller design. *Journal of Aircraft, 45*(1), 23-28.

Popov, A. V., Grigorie, L. T., Botez, R. M., Mamou, M., & Mébarki, Y. (2010). Real time morphing wing optimization validation using wind-tunnel tests. *Journal of Aircraft, 47*(4), 1346-1355.

Popov, A. V., Grigorie, T. L., Botez, R. M., Mébarki, Y., & Mamou, M. (2010). Modeling and testing of a morphing wing in open-loop architecture. *Journal of Aircraft, 47*(3), 917-923.

Popov, A. V., Labib, M., Fays, J., & Botez, R. M. (2008). Closed-loop control simulations on a morphing wing. *Journal of Aircraft, 45*(5), 1794-1803.

Prabu, M. J., Poongodi, P., & Premkumar, K. (2016). Fuzzy supervised online coactive neuro-fuzzy inference system-based rotor position control of brushless DC motor. *IET Power Electronics, 9*(11), 2229-2239.

Premkumar, K., & Manikandan, B. (2014). Adaptive Neuro-Fuzzy Inference System based speed controller for brushless DC motor. *Neurocomputing, 138*, 260-270.

Prock, B., Weisshaar, T., & Crossley, W. (2002). *Morphing airfoil shape change optimization with minimum actuator energy as an objective.* Paper presented at the 9th AIAA/ISSMO Symposium on Multidisciplinary Analysis and Optimization.

Raither, W., Heymanns, M., Bergamini, A., & Ermanni, P. (2012). *Morphing Airfoil with Adaptive Bending-Twist Coupling*: Deutsche Gesellschaft für Luft-und Raumfahrt-Lilienthal-Oberth eV (German Aerospace Congress).

Reich, G., Sanders, B., & Joo, J. (2007). *Development of skins for morphing aircraft applications via topology optimization.* Paper presented at the 48th AIAA/ASME/ASCE/AHS/ASC Structures, Structural Dynamics, and Materials Conference.

Santhanakrishnan, A., Pern, N., Ramakumar, K., & Jacob, J. (2005). Enabling flow control technology for low speed UAVs *Infotech@ Aerospace* (pp. 6960).

Schikuta, E. (1996). *Grid-clustering: An efficient hierarchical clustering method for very large data sets.* Paper presented at the Pattern Recognition, 1996., Proceedings of the 13th International Conference On.

Takagi, T., & Sugeno, M. (1983). *Derivation of fuzzy control rules from human operator's control actions.* Paper presented at the Proceedings of the IFAC symposium on fuzzy information, knowledge representation and decision analysis.

Thill, C., Etches, J., Bond, I., Potter, K., & Weaver, P. (2008). Morphing skins. *The Aeronautical Journal, 112*(1129), 117-139.

Thill, C., Etches, J., Bond, I., Potter, K., & Weaver, P. (2010). Composite corrugated structures for morphing wing skin applications. *Smart Materials and Structures, 19*(12), 124009.

Usher, T. D., Ulibarri, K. R., & Camargo, G. S. (2013). Piezoelectric microfiber composite actuators for morphing wings. *ISRN Materials Science, 2013.*

Vos, R., Barrett, R., de Breuker, R., & Tiso, P. (2007). Post-buckled precompressed elements: a new class of control actuators for morphing wing UAVs. *Smart Materials and Structures, 16*(3), 919.

Wikipedia. (2016). Standard deviation. Retrieved 5th February, 2017, from https://en.wikipedia.org/wiki/Standard_deviation

Wikipedia. (2017a). Counter-electromotive force. Retrieved 16th February 2017, from https://en.wikipedia.org/wiki/Counter-electromotive_force

Wikipedia. (2017b). Linear Variable Differential Transformer. Retrieved 10th January 2017, from https://en.wikipedia.org/wiki/Linear_variable_differential_transformer

Zupan, M., Ashby, M. F., & Fleck, N. A. (2002). Actuator classification and selection—the development of a database. *Advanced Engineering Materials, 4*(12), 933-940.